Studies on the Fabrication and Contact Stiffness of Mechanical Interfaces with Tailored Rough and Structured Surfaces

By

Jack Alan Nathaniel Perris

Submitted in fulfilment of the requirements for the degree of Doctor of Philosophy in Mechanical Engineering.

Nov 2022

James Watt School of Engineering

College of Science and Engineering

University of Glasgow, UK

College of Science and Engineering

Statement of Originality to Accompany Thesis Submission

Name: Jack Alan Nathaniel Perris

Registration number: XXXXXXXX

I certify that the thesis presented here for examination for a PhD degree of the University of Glasgow is solely my own work other than where I have clearly indicated that it is the work of others (in which case the extent of any work carried out jointly by me and any other person is clearly identified in it) and that the thesis has not been edited by a third party beyond what is permitted by the University's PGR Code of Practice. The copyright of this thesis rests with the author. No quotation from it is permitted without full acknowledgement.

I declare that the thesis does not include work forming part of a thesis presented successfully for another degree.

I declare that this thesis has been produced in accordance with the University of Glasgow's Code of Good Practice in Research.

I acknowledge that if any issues are raised regarding good research practice based on review of the thesis, the examination may be postponed pending the outcome of any investigation of the issues.

“You live and learn. At any rate, you live.”

Douglas Adams

Acknowledgements

Firstly, I'd like to thank my supervisors Daniel and Nikolaj for their continued advice and friendly discussion. Both of you have always had an open door for me and provided me with unwavering support throughout my studies.

Thank you to Yang and Charchit for their useful knowledge and friendship throughout all my work. Without you both I'm sure there would be some glaring errors or missing pieces strewn across this thesis. I would like to thank all the members from the MMRG and BIG research groups. Particularly Alex, Neil, Saad, Chris, Ross, Johnny, Andy, and everyone else that offered me their knowledge, expertise, and good laughs along the way. A huge thanks to all the amazing lab staff in the JWNC, Thompson materials lab, and the Rankine synthesis lab. I would be lost without all these hard working and committed people.

Many thanks to all my friends from office 618, Alex, Graham, Louie, Cees, Ahmed, and Tata. You made a young engineer feel at home, welcome, and part of a community in those scary early days. Another huge thank you to all my friends from office 535. You guys were wonderful company and a source of endless laughter.

Another monumental thank you to my friends outside of the university, Callum, Daphne, Stefan, Jamie, Harry, and Ryan. All of you have provided laughter, support, encouragement, and most importantly lent an ear to complain to when necessary.

A massive thank you is due to my wonderful partner Katie. Your endless love and support have been a priceless gift. Without you this experience would have been something else entirely. You provide me with the strength to pick myself up, to keep going, and to produce my best work.

Finally, I'd like to thank my parents. Alan and Jan. You make me believe I'm capable of anything, while that may be only partly true it's still an encouraging thought. You give me the confidence to push myself and strive to create great things.

Jack

Abstract

Contact stiffness is a measure of how interface separation displacement will respond to an applied load. Contact stiffness is most directly affected by interface geometry, material properties, and external factors such as loading, lubrication etc. Surface geometry is often considered in terms of roughness, the asperities that make up a surface and the compliance they introduce to an interface. The compliance or contact stiffness of an interface has an inherent contribution to how mechanical systems operate. This becomes critically important to engineering design where performance is directly linked to interfacial properties, through individual components or a systemic effect – vibrational response machines, biomedical joints, frictional contacts in turbine and engines. If an engineer can control the contact stiffness of an interface, then there is an opportunity to manipulate the performance of a design to suit the needs of the user.

The work in this thesis explores the viability of creating both controlled, tailored, and repeatable pre-defined microstructured and rough surface topographies. The first half of the work involved the development of a novel fabrication technique that combines microfabrication techniques and manufacturing technologies to generate microstructured topographies in functional polymers with the aim of controlling contact stiffness. The designs were initially modelled in finite element software before manufacture and mechanical testing. The microstructured interfaces yielded promising results that indicate high repeatability and tailoring of contact stiffness to the users' defined characteristics. The second half introduces the concept of manipulating numerically generated rough surface topographies to be produced in various polymers, again aiming to control contact stiffness. The numerically generated topographies were 3D printed before being replicated in various polymer materials through injection moulding and polymer casting, and finally mechanically tested. The results display a high level of control of surface characteristics which can be translated into the rough surface interfaces. The designs can then be manipulated to achieve the desired contact stiffness properties in a repeatable and tailored fashion. All areas of the work presented in this thesis have the potential to further tribological knowledge and future applications in a wide range of engineering fields.

Publications arising from the thesis

Perris J, Xu Y, Kartal ME, Gadegaard N, Mulvihill DM. Tailorable and Repeatable Normal Contact Stiffness via Micropatterned Interfaces. *Tribology Letters*. 2021 Sep;69(3):1-2.

Hamilton A, **Perris J**, Convery N, Mulvihill DM, Gadegaard N. Flexible Inserts for Injection Molding of Complex Micro-Structured Polymer Components. *Macromolecular Materials and Engineering*. 2021 Sep;306(9):2100223.

Olender J, **Perris J**, Xu Y, Young C, Mulvihill DM, Gadegaard N. Gecko-inspired dry adhesives for heritage conservation–tackling the surface roughness with empirical testing and finite element modelling. *Journal of Adhesion Science and Technology*. 2022 May 19:1-26.

Perris J, Kumar C, Xu Y, Tassieri M, Kartal ME, Gadegaard N, Mulvihill DM. 3D Printing and Rapid Replication of Advanced Numerically Generated Rough Surface Topographies in Numerous Polymers. *Advanced Engineering Materials*. 2022 Aug 3.

Kumar C, **Perris J**, Bairagi S, Min G, Xu Y, Gadegaard N, Mulvihill DM. Multiscale in-situ quantification of the role of surface roughness and contact area using a novel Mica-PVS triboelectric nanogenerator. Nano Energy. 2022 Dec 21:108122.

+ one more in preparation from the work described in Chapter 6 of this thesis.

Contents

List of figures

Figure 5.4 – Simplified process diagram detailing polymer fabrication routes used to produce the rough surface topographies. Injection moulding process flow (a) and polymer casting process flow (b) [197].

Figure 5.5 – Topography dataset point-to-point comparison. (a) Initially the topography datasets are aligned to ensure correct data point comparison. Two-dimensional representation of the difference measurement direction vector generation between two data points, allowing for heigh displacement calculation. (c) Heat map visualisation of the height difference calculation between the topography datasets, this gives a visual indication of the similarity of the scanned areas [197].

Figure 5.6 – Plot indicating the difference between the target surface roughness, Sq, of the designed topographies) and the measured roughness of the 3D printed samples. The photographs illustrate the 3D printed topographies, (a) 25µm, (b) 50µm, (c) 100µm. The measured values are taken from the average of five printed samples for each topography design [197].

Figure 5.7 – Cross-correlation ratio analysis of the polymer replica surfaces produced from the 3D printed masters. All three distinct rough surface topographies are indicated. The results illustrated show the injection moulded (polystyrene) and the polymer casting methods (ultra-low viscosity epoxy, PDMS, ultra-low viscosity PVS). Each result is the average from 12 sample scans [197].

Figure 5.8 – Mean surface difference analysis of the polymer replica surfaces produced from the 3D printed masters. All three distinct rough surface topographies are indicated. The results illustrated show the injection moulded (polystyrene) and the polymer casting methods (ultra-low viscosity epoxy, PDMS, ultra-low viscosity PVS). Each result is the average from 12 sample scans [197].

Figure 5.9 – Injection moulding inlay durability results. (a) Cross-correlation (CCR) for injection moulded PS replica surfaces from 3D printed master. (b) Mean difference measurement for injection moulded PS surfaces from 3D printed master. Results shown for shots 50, 100, 150, and 200. Consistency across the results illustrates the 3D printed inlays

durability and repeatability for the process. Durability results shown for the three distinct rough surface designs.

Figure 5.10 - Surface tailoring results indicating the ability to fabricate surfaces with varying frequency characteristics. Figure shows the generated topographies (top) and the as-produced 3D printed surfaces (bottom). The frequency cut-off bands are varied from left to right with upper and lower frequency cut-offs (and frequency range) increasing from left to right according to [fl, fs] (Units of 1/mm). Full numerical details in table 14 [197].

Figure 5.11 – Results of the effect of viscosity on surface replication quality. PVS resins used for the polymer casting. Left y-axis details cross-correlation ratio results, right y-axis details surface mean difference. Both analysis methods are plotted against the complex viscosity of the resins. Results measured from 3 samples for each case [197].

Figure 6.1 – Rough surface fabrication process used to produce the rough surface polymer designs.

Figure 6.2 – Experiment schematic of the normal contact stiffness tests. (a) Basic representation of the experimental rig. (b) Application of normal load, P, and relative displacement of interface, d, being measured. Red dashed box indicates a snapshot of how the DIC system tracks the relative approach of the samples. (c) Detailed view of the experimental fixtures for the modified Deben microtester.

Figure 6.3 – Schematic for the test rig that allows for the optical measurements of the real contact area of the rough surface interfaces.

Figure 6.4 – Optical principles that are used in the optical contact measurements. (a) White light is projected from the telecentric lens attached to the pixelink camera through the transparent PMMA and then reflected for capture with destructive and constructive interference depending on the contact area. (b) Sample contact image that demonstrates real contact areas (dark spots) and out of contact regions (bright spots). (c) Binary image after post-processing used to calculate real contact area.

Figure 6.5 – Basic schematic for the ABAQUS model design. (a) 2D schematic of model used in ABAQUS, view is taken from top of model. All dimensions are in mm. (b) FE model with the rough surface data mapped onto the component interface, node and element positions after they have been shifted according to the surface data scans.

Figure 6.6 – Normal contact stiffness evolution with the applied normal load. All surface designs are shown. The ribbon plots indicate the average trend for of the normal contact stiffness and the upper and lower bounds of the results that were observed for each surface design.

Figure 6.7 –Real contact area measurements for the low load tests. (a) Binary images show example images for the 25 and 150 μm design cases at 100 N, 500 N, and 1500 N applied normal load. (b) Data in the graph illustrates the evolution of real contact area for the low load events. (c) Surface scan data of 25 μm design. (d) Surface scan data of 150 μm design.

Figure 6.8 – FE model results and corresponding mechanical test results.

Figure 6.9 - Normal contact stiffness results for all rough surface designs. All samples are loaded to 1500 N.

List of tables

Table 5.3 – Injection moulding inlay durability data indicating numerical results. (a) Cross-correlation (CCR) for injection moulded PS replica surfaces from 3D printed master. (b) Mean difference measurement for injection moulded PS surfaces from 3D printed master. Results shown for shots 50, 100, 150, and 200. Consistency across the results illustrates the 3D printed inlays durability and repeatability for the process. Durability results shown for the three distinct rough surface designs.

Table 5.4 – Numerical parameters used to design the generated surfaces and results of scanned 3D printed topographies. The surface data here corresponds to the surface designs and 3D print scans shown in fig. 52. Hurst exponent = 0.7 for all cases.

Table 5.5 – Numerical results from viscosity investigation. PVS replication from 3D printed master data. Both cross-corelation ratio (CCR) and mean difference measurement are shown.

Table 6.1 – Numerical parameters used to design the generated surfaces. Followed by results of the scanned 3D printed masters, and injection moulded polystyrene replica surfaces.

Nomenclature

Roman symbols

A_n (mm)	Nominal contact area
A_{nf} (mm)	Nominal feature area
A_r (mm)	Real contact area
A (mm)	Contact area of structured feature tops
c (m/s)	Wave speed
d (mm)	Relative displacement of surface reference planes in normal direction
d* (mm)	Relative mean interfacial separation in the normal direction
E (GPa)	Young's modulus
E^* (GPa)	Effective Young's modulus of two dissimilar materials in contact
F_s (μm)	Feature spacing
F_t (μm)	Maximum frictional force
F_w (μm)	Feature width
F (Hz)	Frequency
f_l (1/m)	Lower cut-off wavenumber
f_s (1/m)	Upper cut-off wavenumber
f_k (N)	Kinetic frictional force
f_s (N)	Static frictional force
H	Hurst exponent
h (μm)	Feature height
H_{km}	Complex spectral density

L (m)	Characteristic length (this is used for various applications)
K_n (kN/mm)	Normal contact stiffness
K_t (kN/mm)	Tangential contact stiffness
K_{bn}(kN/mm)	Bulk stiffness in normal direction
K_{bt}(kN/mm)	Bulk stiffness in tangential direction
$K_{roughness}$(kN/mm)	Stiffness due to surface roughness
$K_{saturation}$ (kN/mm)	Saturation stiffness
K_{tn}(kN/mm)	Total stiffness in normal direction
K_{tt}(kN/mm)	Total stiffness in tangential direction
P (N)	Applied normal load
Q (N)	Applied tangential load
R	Reflection coefficient
R_a (µm)	Centre line average roughness
R_q (µm)	Root mean square roughness
S (mm^2/Hz)	Power spectrum density
S_a (µm)	Areal centre line average roughness
S_{al}	Auto-correlation length
S_{dq} (µm)	Areal root mean square gradient
S_q (µm)	Areal root mean square roughness
R_x (µm)	Radii of object 'x'
r_o (µm)	Contact region for Hertzian contact
T_g (°C)	Glass transition temperature of a material

S_y (GPa)	Yield strength of a material
Z (kg/m^{2}s)	Acoustic impedance
Z_x (μm)	Amplitude of surface profile 'x'

Greek symbols

δ (mm)	Relative displacement of surface reference planes in tangential direction
δ* (mm)	Distance that the Hertzian spheres have penetrated each other
κ_s (μm)	Mean summit curvature of asperities
λ_f (μm)	Square wave feature width
λ_p (μm)	Square wave feature period
μ_k	Coefficient of kinetic friction
μ_s	Coefficient of static friction
ρ (kg/m^3)	Density
σ_{rms}	Standard deviation of asperity and summit heights
ν	Poisson's ratio
Ψ	Plasticity index
ω (rad/s)	Angular frequency

Abbreviations

3D	Three dimensional
AFM	Atomic force microscopy
AR	Aspect ratio
BEM	Boundary element method

CAD	Computer aided design
CCR	Cross correlation ratio
CNC	Computer numerical control
COC	Cyclic olefin copolymer
DED	Direct energy deposition
DIC	Digital image correlation
DMD	Direct metal deposition
ECM	Electrochemical machining
FDM	Fused deposition modelling
FE	Finite element
FEA	Finite element model
GW	Greenwood Williamson model
ICP	Induction coupled plasma
IPA	Isopropyl alcohol
JWNC	James Watt Nanofabrication Centre
LIGA	Lithographie, galvanik, und abformung (lithography, electroplating, and moulding)
LOM	Laminated object manufacture
MEMS	Microelectromechanical systems
NIL	Nanoimprint lithography
PC	Poly(carbonate)
PDMS	Poly(dimethyl siloxane)

PMMA	Poly(methyl methacrylate)
PET	Poly(ethylene terephthalate)
PP	Poly(propylene)
PS	Poly(styrene)
PSD	Power spectrum density
PVS	Poly(vinyl siloxane)
RMS	Root mean square
SEM	Scanning electron microscope
SLA	Stereolithography
TENG	Triboelectric nanogenerator
UV	Ultra-violet
μEDM	Micro-electrical discharge machining

Chapter 1.

Introduction

Surfaces are everywhere. Surfaces are contained in everything. They connect the world around us and function as the basis for all physical interactions from nano to micro, to macroscale. Surface interactions control how we live, how we breathe, and how the engineering world around us functions. If surfaces can be properly understood, then we can better comprehend our living environment. Though vastly complex, surface interactions can be broken down into an intertwined system of scientific problems that can be manipulated to develop innovative design solutions.

The work in this thesis explores how surfaces can be designed and fabricated to control and generate certain phenomena. Specifically, this is an exploration into contact mechanics and surface fabrication aspects. The projects aim to bridge the gap between material science, mechanical engineering, and surface engineering. The surface engineering and fabrication methodologies utilised are wide and varied, allowing for the generation of unique engineering concepts.

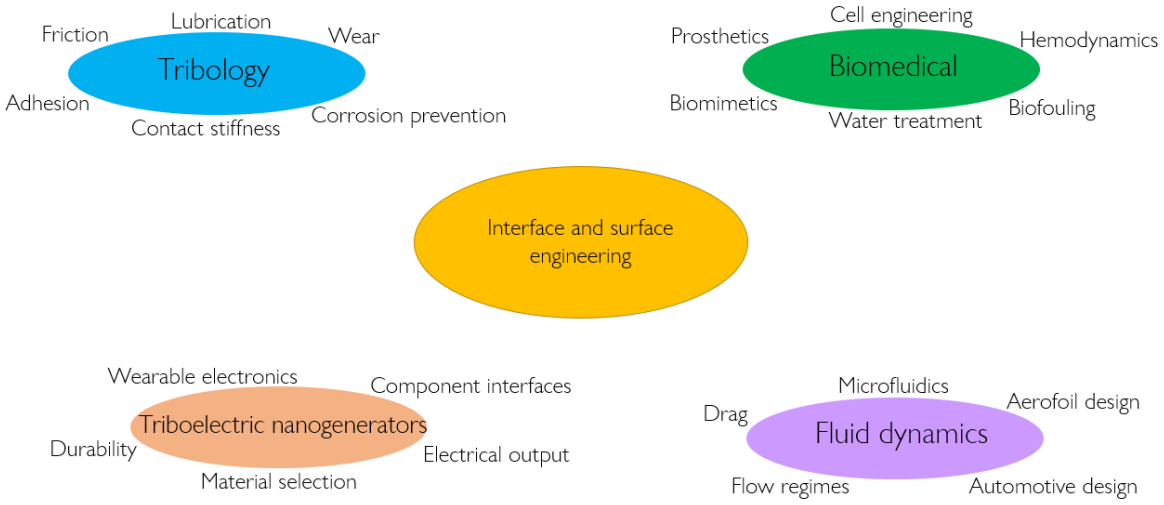

Figure 1.1 – Interface design and surface engineering applications

Interfaces can be considered a weak link in engineering design due to their unpredictability and unrepeatable properties. This makes interfaces difficult to optimise and tailor. Contact stiffness modelling and measurements allow interfaces in contact to be more fully understood. This is particularly important for design and modelling of high precision mechanical machines. Vibrational response and damping are affected by the contact stiffness of the vast array of surfaces in contact within a machine. The presence of real rough surfaces introduces compliance to the machine system, reducing the overall stiffness of the system. They also provide damping by dissipating frictional energy within the joints. Traditional surfaces in machine design can be difficult to model and define due to their unstructured and often random nature. This means the interfaces in contact throughout a system are not fully accounted for, causing reduced modelling accuracy and performance.

Contact stiffness is the property that defines the relationship of an interface's displacement to applied load. The contact stiffness is the reciprocal of the compliance introduced by a surface's topography. The asperities in contact over an interface will experience a deformation due to an applied load, this applies in both the normal and tangential direction. Real surfaces in engineering have varying roughness and surface properties based on their material properties and manufacture methods. Asperities can vary drastically in height, location, and concentration from surface to surface. If two surfaces are brought together, the interactions within the interface can vary greatly depending on positioning and the respective surface topographies. This creates an inherent unpredictability when considering the contact stiffness of interfaces.

Microfabrication techniques allow for production of structured surfaces through advanced manufacture methods. The techniques allow for extremely accurate design to be achieved. Tight tolerances can be achieved on the topographical designs of an interface. Microfabrication can potentially eliminate the unpredictability and multiscale attributes of interface features, typically associated with both traditional and more advanced manufacturing techniques. The fabrication of predictable and tailorable surfaces will allow interfacial properties to be determined without expensive experiments or analysis. Further

it will allow interfaces to be tailored for design or use and specific properties can be achieved through the microfabrication and structuring of surface design.

Tailored and optimised surfaces were explored, with the interfacial property of contact stiffness in mind. The work here has a strong focus on developing novel microfabrication techniques to develop controlled interfaces that could be designed and modelled numerically, and then mechanically tested. This was achieved by fabricating interfaces using the techniques and technology available at the James Watt Nanofabrication Centre (JWNC) and the Biomedical Interfaces at Glasgow (BIG) group. This was done in tandem with testing/exploring the mechanical engineering aspects using the expertise and equipment of the Materials and Manufacturing Research Group (MMRG).

These initial studies yielded promising results and proved that we can harness the geometry of an interface to provide specific designed mechanical properties. From here, the decision was made to explore further manufacturing tools for surface engineering. Specifically, the development of a rough surface design and fabrication tool for research. The aim here was to provide a method for researchers to design and produce prototypes of rough surfaces, and then replicate these in various materials for study. This allows the examination of how certain surface parameters influence engineering systems such as biological cell growth, triboelectric systems, and contact mechanics phenomena.

The replication methods incorporated within the fabrication tool took inspiration from the field of biomimetics. Biomimetics and surface replication is a field where biology and engineering meet to develop interfaces and surfaces that take inspiration from nature. Nature is often thought of as one of the best designers. It has developed geometries, materials, structures, and processes that influence the world for an organism to survive and flourish. The evolution of hierarchical structures from nanoscale to macroscale has allowed the development of systems in bacteria, to sea creatures, to plants that facilitate mechanical and biological advantages. Plants can embody self-cleaning mechanisms and superhydrophobic surfaces, animals can exhibit extreme adhesion through mechanical phenomena alone, and sharks can demonstrate drag reducing skin structures. Designers and engineers take inspiration from these systems extensively in far reaching disciplines to

improve their solutions and develop improved concepts. The tool developed here enabled the techniques from biomimicry to be transferred to a tribological context for rough surface systems to be further explored.

The fabrication tool was put to the test in a study where it was used to develop a series of rough surface interface designs. These interfaces were examined and mechanically tested to highlight how certain topography parameters can influence both contact stiffness and real contact area evolution of rough surface contacts. This was a case study to highlight the potential capabilities of the research tool.

This thesis approaches surfaces from a unique standpoint. The work examines and highlights how normal contact stiffness can be designed and controlled through novel fabrication techniques that are applied to both microstructured and rough surface interfaces. We not only explore the mechanical behaviour of interfaces, but how to harness the property of contact stiffness by generating innovative interface designs that behave in a manner defined by the user. These tools allow the investigation of interfacial phenomena and how surface design can develop innovative engineering solutions.

The specific aims of this thesis are as follows:

- Establish and develop novel fabrication routes that facilitate the production of complex microstructured thermoplastic polymer topographies. This will be achieved by combining reliable, repeatable fabrication and manufacturing techniques available both in the James Watt nanofabrication centre and the manufacturing technologies at the MMRG and BIG research groups.

- Further develop this fabrication technique to establish a clear cleanroom microfabrication to injection moulding rapid prototyping route for MEMS device design and manufacture. This technique should allow for high throughput for potential application into mass production.

- A clear analysis method must be established for assessing the topographical features of the microstructured polymer interfaces. This will allow for full assessment of microfeature quality, and part replication throughout the stages of the fabrication technique.

- Investigate the full capabilities of the microfabrication technique. How versatile is the fabrication method? Potential assessment can involve the range of features can be made, device complexity, feature shape and spacing, and aspect ratio of features the devices that can be fabricated using the techniques developed.

- Explore the capabilities of microstructured polymer interface's ability to provide tailored and repeatable normal contact stiffness. Develop appropriate mechanical test rig and methodology to facilitate the measurement of normal contact stiffness. Generate FE models to support, validate the empirical results, and guide the testing methodology of microstructured interfaces.

- Investigate how the microstructured surface designs can influence the tangential contact stiffness of an interface. With further aims of creating tailored and tuneable tangential contact stiffness characteristics of an interface.

- Attempt to develop a manufacturing route that can facilitate repeatable and tuneable rough surface interface designs. Explore how rough surface topographical features influence the normal contact stiffness of an interface.

- Establish a clear protocol to full analyse the quality of rough surface topographies and the quality of replica polymer samples.

- Explore what topographical features of rough surface interfaces influence TENG design and by extension device performance and efficiency.

- Fully document the success and failures of these aims. Explore where there are still gaps in the recorded knowledge gained from the projects that are a part of this thesis. All processes and manufacturing routes should be fully detailed to allow further work associated with the projects in this thesis.

Chapter 2.

Literature Review

2.1 Introduction

The property of contact stiffness governs the relationship between the displacement an interface experiences and load applied. Traditionally load is applied to an interface consisting of rough contacts and asperities. The interaction or contact between surfaces can be analysed in two ways. Surfaces can be considered to be perfectly smooth; this is an unrealistic simplification and approximation to the problem of analysing the contact interface between two surfaces. In this case, the stiffness measure would be entirely due to bulk material effects. More appropriately, surfaces are considered to be real and rough; this assumption encompasses the true nature of a rough surface where many multiscale asperities will interact and deform together when in contact. When the interface is modelled as a real surface with rough contacts, the behaviour of the interface as it displaces under loading can be described using contact stiffness.

The contact stiffness that is present at the interface between the two contacting surfaces is caused by the elastic and plastic deformations experienced by the asperities of a rough surface [1]. There are two types of contact that are considered with surfaces, these are incomplete and complete contact. During incomplete contact, the contact area is not defined by the topographical geometrical features, and this will increase as the loading increases until complete contact of an interface is achieved. This can be thought of as real contact area and considers the micro-scale interactions of a surface. Complete contact is defined by the global macroscale geometrical features of one of the interfaces and the contact area will remain constant despite changes in loading. This is idealised contact [2] [3]. This thesis will focus on incomplete contact regions.

Contact stiffness modelling, interfacial parameters and measurements are important for machines, particularly high precision machines, with joined mechanical interfaces such as the piston-cylinder mechanism in a combustion engine, the turbine blade to housing interface in jet engines and wind-turbines. Contact stiffness is also important in magnetic storage hard disk drives [4] and robotic grip systems where grip capabilities are affected by the stiffness of the contact made [5]. Contact damping is important to the design of interfaces as all these systems have vibrational responses and interfacial properties. These surfaces in contact are modelled to predict the machines operation, structural integrity, and efficiencies. Traditional surfaces in these machines are difficult to define and model; therefore, they are not fully accounted for in machine design. This results in reduced performance, inefficiencies, and reduced modelling accuracy [6]. If the contact stiffness can be fully characterised and be produced in a predictable, repeatable manner with defined parameters, then the interfaces can be fully understood and accounted for in simulation and mechanical design. This could also mean that surfaces could be tailored for their specific use rather than being random and unstructured.

The interfacial properties present when two real surfaces are in contact depends on the random nature of the interaction of asperities present on each surface. Unlike in idealised contact, real/rough surfaces have very few asperities that initially make contact. This can result in large local stresses present at contact regions. The nature of these interactions is therefore a mix of both elastic and plastic material behaviour [7]. Theoretical models often assume the contacts to be perfectly smooth and often elastic in nature. However, real surfaces do not have perfectly round or smooth contacts. This results in larger displacements than predicted by theoretical models as larger stresses are induced at the asperity contacts in real contact regions causing plastic deformation which is inherently larger than the elastic deformation present in the models [8].

2.2 Definition of contact stiffness

The following definitions assume the bulk material and interface material of each body to be of the same material unless stated otherwise. When considering two bodies that are pressed together, there will be a compression or relative displacement towards each other

as a result of the applied load. This is the result of the relative displacement of both the interface and the bulk material of the respective bodies [9].

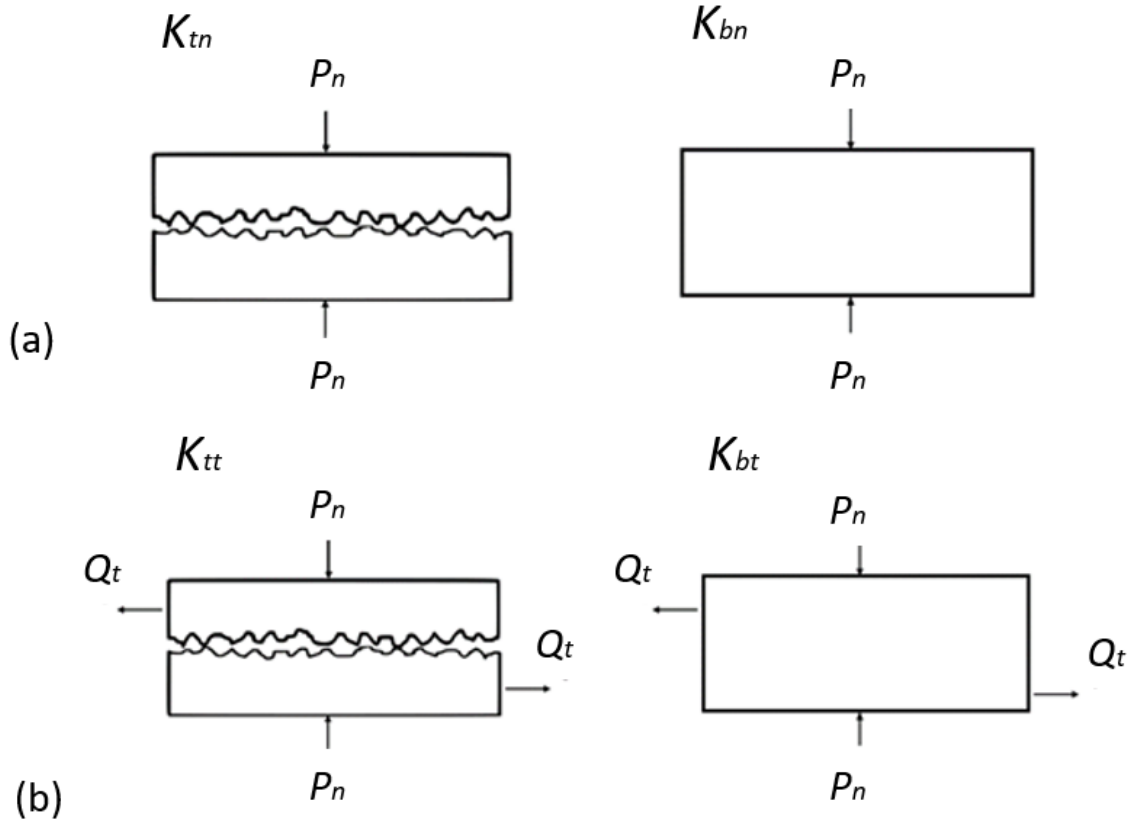

Figure 2.1 - Diagram of bulk, K_{bn} or K_{bt}, and total stiffness, K_{tn} or K_{tt}, in both the normal and tangential directions. Normal loading only case (a). Normal and tangential loading case (b).

The diagram in figure 2.1 shows the total stiffness in both the normal and tangential directions, K_{tn} or K_{tt}, respectively, and the bulk stiffness in both the normal and tangential directions, K_{bn} or $K_{bt,}$ respectively. Bulk stiffness can be thought of as if the two bodies were connected completely as one piece of material with no voids or interface, while total stiffness is the contact stiffness that arises from both the bulk stiffness and interfacial stiffness working together. The basic definitions of normal and tangential contact stiffness can be illustrated using Eqs. 2.1 and 2.2 respectively. Normal contact stiffness K_n is generally defined as the rate of change of the applied normal load, P, with respect to the change in normal relative displacement, d^*, of the interface as:

$$K_n = \left|\frac{dP}{dd^*}\right|$$

(2.1)

Tangential contact stiffness, K_t, can be defined in a similar manner as the rate of change of the applied tangential load, Q, with respect to the tangential displacement, δ [9].

$$K_t = \left|\frac{dQ}{d\delta}\right|$$

(2.2)

Both definitions of contact stiffness are due to the rough surface of the interface acting independently of the bulk material [10]. These properties of contact stiffness are related to the total and bulk stiffness previously mentioned. The total stiffness can be used along with the bulk stiffness of the material to give the interfacial contact stiffness properties. The contact stiffness properties of the bulk material and interface can be thought of as a system of springs in series. This gives rise to Eqs. 2.3 and 2.4 that illustrate the calculation of the interfacial contact stiffness. This enables the interface stiffness to be measured and analysed through the isolation from the effects of bulk compliance.

$$\frac{1}{K_n} = \frac{1}{K_{tn}} - \frac{1}{K_{bn}}$$

(2.3)

$$\frac{1}{K_t} = \frac{1}{K_{tt}} - \frac{1}{K_{bt}}$$

(2.4)

Fig. 2.2 illustrates the representation of the spring system approximation of the interface and bulk material that are used to build Eqs. 2.3 and 2.4. This assumption allows the use of Hooke's law to build an equivalent stiffness of the bulk material and interface stiffness in series.

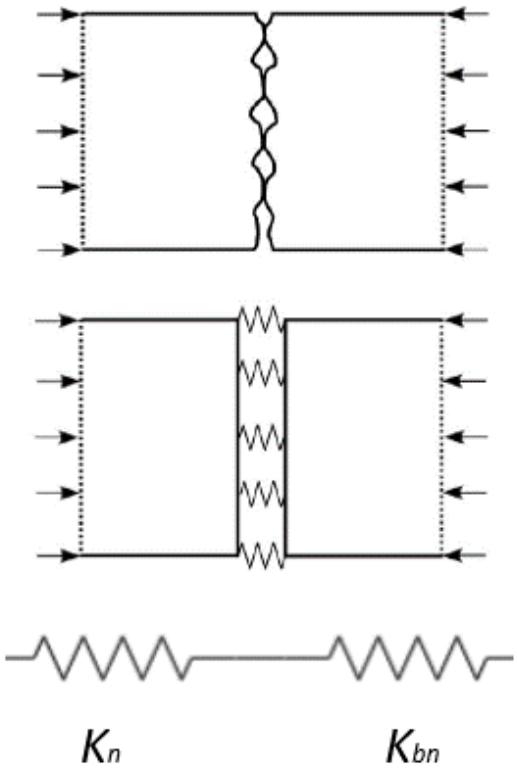

Figure 2.2 - Spring system approximation representing the compliance/stiffness of an interface, K_n, coupled with the bulk stiffness of the material, K_{bn}.

2.3 Normal contact stiffness

The way normal contact stiffness will be defined in this study is slightly different to previous definitions. The definition used in this work follows the definition approach in Parel [2]. The study defines normal contact stiffness as the rate of change of normal loading with respect to the change in the mean interfacial separation, i.e. the mean gap between the surfaces. The relative displacement between the surfaces will be measured using a displacement field close to the interface. This allows relative displacement measurements to be taken close to the interface, but without using the mean surface roughness of the actual interface and having to take exact nano/micro asperities into account. Parel [2] found this to be a more practical and laboratory friendly way to measure interfacial separation to make normal contact stiffness measurements.

Parel based his method on previous studies by Persson and similar studies of contact mechanics where the interfacial separation is defined as the mean gap or distance between a mean surface height line on each surface. This resulted in the relative displacement being

the relative displacement of the two mean surface height lines [3, 11]. Parel concluded that these methods are useful in construction of contact models for contact mechanics relations such as the contact stiffness. However, these methods were not particularly practical for making measurements between two surfaces directly as they are taken directly at the interface [2] [3, 11].

Mulvihill et al. [12] use a slightly different approach in their paper that compares the use of DIC (digital image correlation) and ultrasound techniques. Here, the relative displacement of the interfaces is taken from two points on either side of the interface. The distance between an array of points is then recorded during subsequent loading events and used in the measurement of contact stiffness. Wang et al. [13] used an interesting method where they pressed a nominally flat rubber surface into a rough asphalt surface. The relation between the penetration depth, or average interfacial separation, and applied pressure were used to determine the contact stiffness. This is comparable to the initial normal contact stiffness tests in this thesis where a structured surface will be pressed against a nominally flat surface with separation at subsequent loading events recorded. This approach has the viability to be explored and compared with measurements taken using Parel's method of interfacial separation.

Parel's approach will primarily be adopted for normal contact measurements in this thesis due to its practical nature and ability to analyse the full interface.

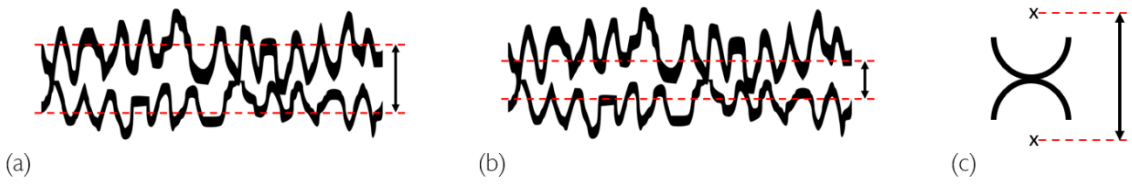

Figure 2.3 - Three types of normal contact displacements: (a) Considers mean surface height of a surface in contact, (b) Considers the mean peak asperity heights and their interaction, (c) Contact measured from a mean distance away from the interface interaction zone, typically influenced by the bulk material.

Fig. 2.3 describes the three main ways in which normal contact interfacial separation can generally be described. Fig. 2.3(a) shows the methodology used by Persson and similar studies where only the interfacial interaction of the pure asperities is considered. This is

typical for analytical solutions of contact mechanics. While the Fig. 2.3(c) approximates the methodology used by Mulvihill et al. This represents a line used to measure the approach of an interface at some distance from the interaction zone of the asperities. This method is more useful for experimental applications. Fig. 2.3(b) represents modelling situations where the peak asperities are concerned and coming into contact first, this would mainly be considered and useful in situations where lower loads are concerned. Therefore, the mean asperity height will be considered rather than the mean surface height line of the whole interface since fewer asperities will be in contact so a mean surface height line of the whole interface will skew measurements as it will produce values indicating more contact than is present. Medina et al [7] focuses on lightly loaded systems where asperities in contact are relatively widely spaced and used this definition of the interfacial separation.

2.4 Tangential contact stiffness

Information and techniques for defining tangential contact stiffness are more limited than the studies available concerning normal contact stiffness. Tangential contact stiffness is defined in the same manner mathematically. The instantaneous rate of change of the tangential loading with respect to the rate of change of the tangential position of the two interfaces. Tangential contact stiffness, K_t, can be defined as the rate of change of the applied tangential load, Q, with respect to the tangential displacement, δ [8]. See Eq. 1.2.

Kartal et al. [14, 15] found that tangential contact stiffness is highly dependent on both the normal pressure and nominal contact area. In two studies Kartal et al. used digital image correlation (DIC) to measure the tangential contact stiffness. However, it was concluded that the measurements made using the DIC were affected by the bulk material stiffness to some extent. Even if this effect is small, it becomes an issue that must be addressed for both normal and tangential measurements. Therefore, DIC cannot be alone used to predict the stiffness of an interface. This effect can be minimised by placing the targets close to the interface of the surfaces in contact. However, there is potential for a large influence on the combined stiffness of bulk effects, K_b, and the interface stiffness, K_n. Especially for the microstructured interfaces assessed in this work.

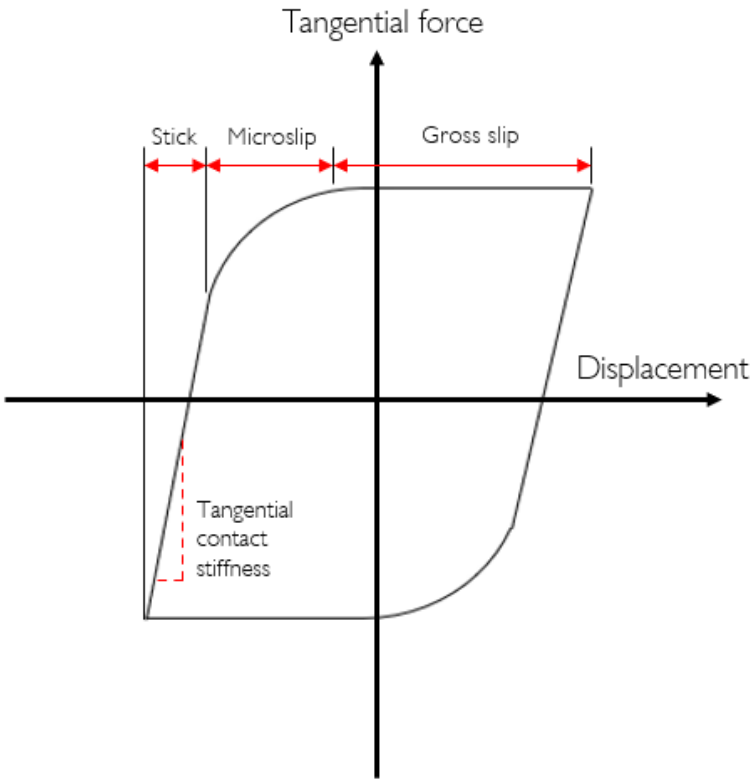

Figure 2.4 - Frictional hysteresis loop – Displacement vs. Tangential force/Frictional force. illustrating the microslip region used to calculate tangential contact stiffness.

Kartal et al. [14, 15] used a method that uses frictional hysteresis loops arising during fretting cycles to examine tangential contact stiffness. Tangential contact stiffness occurs within the microslip region of a hysteresis loop that arises when tangential force is plotted against tangential displacement during a fretting cycle. These relations are non-linear, as seen in Fig. 2.4. To gain a linear relationship of tangential contact stiffness, a measurement of tangential contact stiffness in the microslip region of the reverse sliding direction is taken. There are other methods that use ultrasound to measure the tangential contact stiffness. These methods are thought to eliminate the bulk stiffness contributions, but do not allow for a full field measurement of the whole interface to be achieved at the interface [7, 16-17].

When Berthoud and Baumberger focused on shear interfacial stiffness i.e. tangential stiffness [18]. They hypothesised that it was important to remove the bulk stiffness from overall stiffness measurements to enable the measurement of the true interfacial stiffness. In their study, strain gauges were used to measure micro displacements by loading the apparatus to

induce shear loading and shear contact stiffness measurements were obtained. These measurements were used along with the simple spring model previously described (Eqs. 2.3 and 2.4) to emphasise the interface's tangential contact stiffness independently of the bulk stiffness. After reading various studies into the tangential contact stiffness, it appears it is somewhat more difficult to characterise and measure than in the normal direction. However, it has previously been achieved with good accuracy. Mulvihill et al. [12] compared both ultrasound and DIC for measuring contact stiffness and concluded that DIC should be used when measuring tangential contact stiffness.

2.5 Basic contact theories and analytical models

Modelling of the elastic-plastic interactions of asperities on a micro and macro scale is important as this allows us to define the contact properties of a surface. One of the earliest models introduced was by Greenwood and Williamson [19]. This model concerned rough elastic asperity contact; however, the asperity interactions within the model are based on the Hertz contact solution. Hertz examined the 'smooth' or frictionless contact between elastic solids. These were approximated to be parabolic in the region close to the area of contact. Hertz's theory predicted that contact area increases in a non-linear fashion with the applied compressive force. Most of the contact theories approximate the asperities to be either spherical or elliptical, allowing for Hertz theory to be applied [20, 21].

Most theories of contact are observed to neglect elastic coupling between the asperities: essentially, the asperities act independently of each other. However, this is only reasonable if the contact regions are sufficiently spread out [6]. Another major assumption for the theory is that the area of real contact be small in relation to nominal contact area [21].

Hertzian theory describes the way two elastic spherical bodies behave when in contact. These spheres have radii R_1 and R_2 respectively. They are assumed to be perfectly smooth and squeezed together by a compressive force P. Hertz minimised the elastic deformation energy between the spheres to develop an expression for the deformation field between the solids. The radius r_0 represents the contact region as shown in Fig. 2.5 [22].

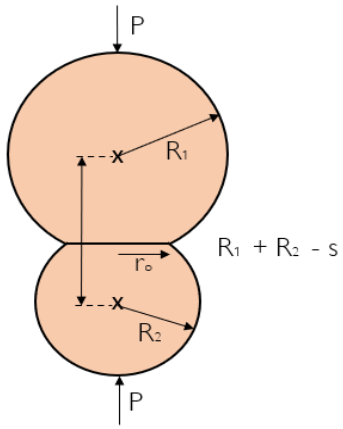

Figure 2.5 - Contact between two elastic spheres to illustrate Hertzian contact

Fig. 2.5 is the situation modelled by the following equations. The contact region is given by the expression:

$$r_0 = \left(\frac{R_1 R_2}{R_1 + R_2}\right)^{1/3} \left(\frac{3P(1-\nu^2)}{4E}\right)^{1/3} \tag{2.5}$$

where

$$\frac{1-\nu^2}{E} = \frac{1-{\nu_1}^2}{E_1} + \frac{1-{\nu_2}^2}{E_2} \tag{2.6}$$

E_1 and E_2 represent the Young's modulus of the spheres and ν_1 and ν_2 are the Poisson's ratio of the two spheres. While δ^*, in this case, represents the distance that the solids have penetrated each other resulting in a reduction of the distance from their respective centres (R_1 +R_2). This is given by the following expression:

$$\delta^* = \left(\frac{R_1 R_2}{R_1 + R_2}\right)^{1/3} \left(\frac{3P(1-\nu^2)}{4E}\right)^{1/3} \tag{2.7}$$

If Hertzian theory is applied to a sphere, with radius R, pressed against a nominally flat surface, the expression for contact area can be reduced to:

$$\pi {r_0}^2 = \pi R \delta^* \tag{2.8}$$

The compressive force can be approximated as:

$$P = \frac{4E}{3(1-\nu^2)} \delta^{3/2} R^{1/2} \tag{2.9}$$

Where $\delta^*$is equal to the indentation, penetration, or rigid body displacement. This can then be used to develop an expression for the theoretical normal contact stiffness present when considering Hertzian style contacts:

$$K_n = \frac{dP}{d\delta^*} = \frac{2E}{(1-\nu^2)} R^{1/2} \delta^{*1/2} \tag{2.10}$$

Greenwood and Williamson's (GW) model built on this contact theory to develop a general solution for an entire surface in contact. The original paper where they published the contact model highlighted the fact that, for a rough elastic contact area, the real contact area would be proportional to the normal load. This only applies for relatively low loads to ensure that the contacts remain elastic [23]. The work highlighted that, for an exponential distribution of asperity heights, the real contact area is proportional to the normal load applied. Further they showed that for a Gaussian distribution of heights, akin to a true engineering surface, the real contact area was nearly directly proportional to the normal load applied. The theory is a standard in predicting the load-displacement behaviour of rough surfaces in contact with contacting asperities. The theory can also be used as an inverse where asperity distribution can be determined based upon topographical measurements. This can allow the asperity height distribution to be monitored and evaluated as loading varies [24].

The GW model makes many assumptions in its construction: The roughness is on a single scale, the asperities can be approximated as spherical bumps with equal radius of curvature, the asperities are assumed to act independently with no influence on each other, the deformation is assumed to follow the Herztian model previously described, the bulk material has no influence on the deformation of the interface i.e. it does not deform, and finally the heights can be approximated using a Gaussian height distribution.

In the original paper presented by Greenwood and Williamson, no contact stiffness measurements were generated. Their analysis did not grant a closed form solution. However, this paper gave a method to describe how the asperity tips of an interface would

approach and interact as loading increases. Many papers have illustrated how this relationship is non-linear when considering the Hertzian contacts [6, 8, 11, 25]. Shi and Polycarpou used a modified version of the Greenwood and Williamson model to develop simulations of contact stiffness with varying rms roughness measurements for comparison with their experimental measurements [6]. They developed a closed form solution to the contact calculations in the model by using an exponential function to fit the end of the Gaussian Distribution used in the Greenwood Williamson model (to describe the heights of the asperities). This simplifies the asperity interactions and allows the comparison of load and surface roughness to develop simulated contact stiffness measurements.

The expression developed by Shi and Polycarpou to calculate stiffness, $k_c(d)$, is as follows:

$$|k_c(d)| = \left|\frac{\lambda}{R_q} P(d)\right| \tag{2.11}$$

Where $P(d)$ is a non-linear contact force that has been significantly simplified from the original Greenwood Williamson model using an exponential function as described above. λ is a curve fitting constant with the value of 3, while R_q is the rms roughness measurement of the surface concerned. This expression allows for the calculation of contact stiffness based on surface roughness measurements.

There have been many models developed since the original Greenwood and Williamson version. Many have made additions to the model's complexity. This has developed the original interfacial model further to improve its accuracy. For example, Bush et al. improved the model by introducing multi-scale roughness [26]. This is more appropriate as a real surface will have multiple wavelengths of roughness of varying scale all coexisting within the same interface.

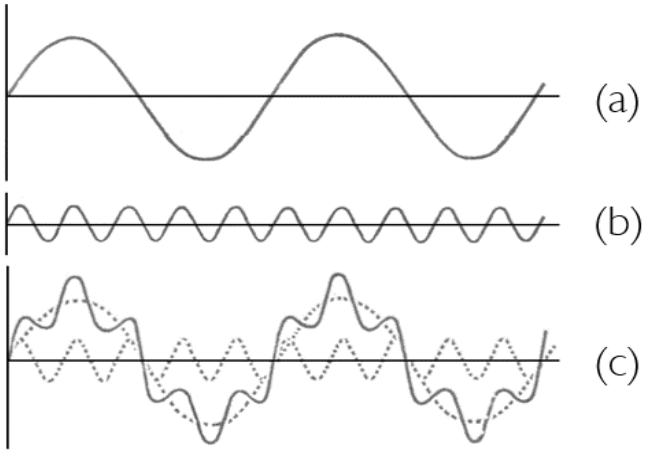

Figure 2.6 – Simplified wavelengths of roughness that contribute to a surface's topography: (a) Long wavelength waviness or curvature of a surface, (b) Short wavelength or high frequency roughness, typically used to illustrate the asperities of a surface and (c) Resulting topography from the combined attributes of the rough surface components.

Generally, there will be multiple wavelengths or frequencies of roughness coexisting on one surface. This gives rise to asperities on a miniature scale all tightly spaced with varying heights in contrast to large waves influencing the interface on a much larger scale. This results in asperities being present on the interface that have vastly different properties in terms of height, length, scale, and stiffness. A multiscale model is therefore more appropriate when describing a real interface and its interactions. Fig. 2.6 demonstrates this idea in a rudimentary form with only two wavelengths which then combine to give a multi wavelength and scale waveform. However, on a real surface many wavelengths will coexist to form an overall surface roughness and profile of the interface.

The Bush et al. [26] model resulted in the finding that when roughness occurs on different scales, the real area of contact A (for small loads) is proportional to the compressive force. They concluded that this property was only true when roughness occurs on many different scales. Their model again assumed that asperities are not influenced by one another on the same interface.

Interaction of asperities was included into the model developed by Ciavarella, Greenwood, and Paggi [27]. For lighter loads, the inclusion of interaction of asperities will have little effect on the model's results. However, for larger loads, the asperity contacts in this model

were treated to be uniformly distributed over the apparent contact area with the resulting deformation due to these asperities being assumed to be uniform. This paper noted that when there are a small number of asperities over a small area then the inclusion of interaction does not cause great variation in the results, but if a larger area is considered, then the number of asperities increases and the inclusion of interaction can cause large differences in the results of the original and improved version [27].

Bo Persson has published many papers that aim to improve and build on existing models that came before. Several of the models developed by Persson are energy based and build on the original Greenwood and Williamson models [11]. His models aimed to include the interactions of asperities to more accurately represent the behaviour of rough surfaces in contact [21]. The original model Persson developed is accurate for when $A_c < A_n$ and highlights that, during loading of surfaces, the contact area is proportional to the normal load applied [21]. The original model was developed for rubber against a stiff material and therefore the real area of contact, A_c, can be assumed to be equal to the nominal contact area, A_n. The nominal area of contact is the global area of a surface which does not consider the microscale interactions of topographical features. The real contact area takes into account the topographical features of a surface and their interactions which cause areas of no contact across the macro dimensions of a surface. When applied to low loads, Persson developed a solution that described normal loading in terms of the mean gap between the two interfaces in contact:

$$p_n \sim p_c e^{-U_m/U_o} \tag{2.12}$$

Where p_n is the normal pressure applied to the surfaces ($-P_n/A_n$), U_m is the mean gap between the surfaces, and U_o is the parameter determined by fractal surface profiles [11]. From the original definition of normal contact stiffness, this implies that contact stiffness can be given by:

$$K_n = \frac{p_n A_n}{U_o}$$

(2.13)

This equation is similar to previous expressions describing contact stiffness but directly depends on the fractal dimension of a surface, $U_o \approx \gamma_p h_{rms}$, where $U_o$is the characteristic length, which is the order of the combined h_{rms}. Eq. 2.13 applies for fractal dimension values near 2. Fractal dimension describes the complexity or surface roughness over many orders of magnitude. It is usually between the non-integer values of 2 and 3 [28]. For Eq. 1.13, h_{rms} is the root mean square roughness of the surface, while γ_p represents the ratio U_o/h_{rms}, a near linear constant [13, 29]. Wang et al. [13] developed this parameter from slopes calculated using measured surface roughness power spectrum as input. This gave a slope representing U_o/h_{rms} plotted over h_{rms}.

Another interesting feature of the Persson model is that for numerical results it can be seen that $A_c/F_N = P$ constant over a much larger range than for the Greenwood Williamson model [29].

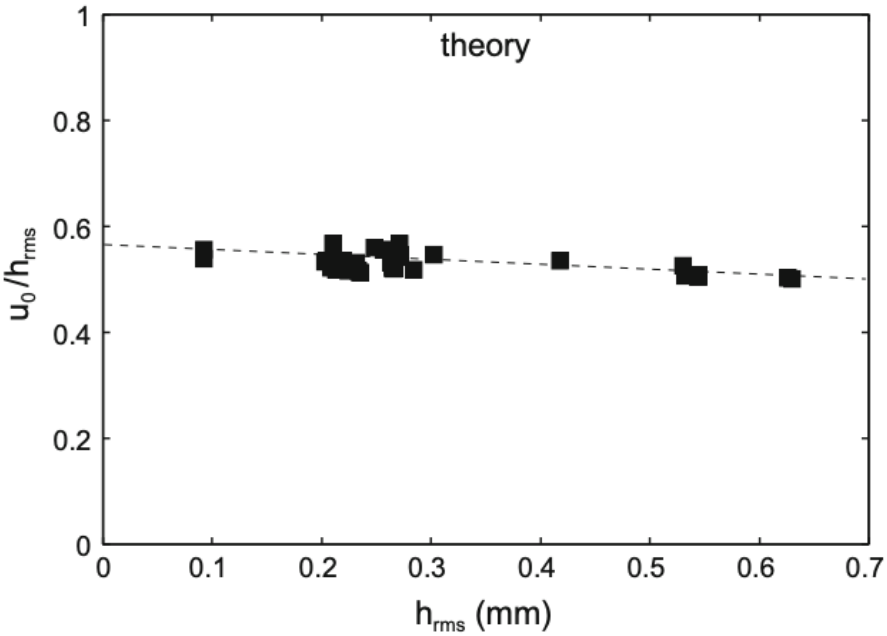

Figure 2.7 - The ratio U_0/h_{rms} as a function of the root-mean square roughness h_{rms} of the road surface examined in Wang et al [13]

Hyun et al. developed a FEA model for self-affine surfaces [30]. The model consisted of a rough elastic surface pressing against a nominally rigid flat surface. The model was used to follow the evolution of contact area with loading. The contact area between the two surfaces was found by finding how many nodes from the rough surface tried to penetrate

the flat surface through discretising the surface and finding all nodes in contact. In this model, Hyun found that, when the contact area remained below 10% of the nominal contact area, then the real area of contact was seen to be proportional to the squeezing force. The model is seen to show similar results to the Bush and Persson models [29-30]. A similar study was conducted by Pie and Hyun et al [31]. This model again followed the evolution of contacting region, along with local contact pressures, and subsurface deformations. However, this model used a fractal surface and modelled the elastic-plastic behaviour of the material.

Akarapu et al. [32] examined the effects of surface roughness on both the normal and transverse stiffness of the contact between two elastic surfaces/bodies. This was done by using molecular dynamics and continuum calculations. They observed the contact area and normal and lateral contact stiffness to increase linearly with the applied load, along with the load increasing exponentially as the surface separation decreased. The paper examined the variation of P_N with interfacial separation *u* for varying system sizes. Their results for varying system size, *L*, and Hurst exponent, *H* (The Hurst exponent characterises the roughness of a surface. With low values representing high roughness characteristics and vice versa, values usually range between 0.5 and 0.9), were all seen to have linear variations with a slope of $\gamma_p = 0.48$. The Hurst exponent characterises the roughness of a surface. With low values representing high roughness characteristics and vice versa.

The results of all the studies pursued within this paper come to the conclusion that there is a direct connection between contact stiffness and contact area: this agrees with many previous studies. The atomic-scale simulations in this study were used to model contact stiffness with roughness on varying scale and the results agree with Persson's continuum theory down to very small scales [32].

Pohrt and Popov used the boundary element method to calculate normal interfacial stiffness of two elastic bodies with randomly rough surfaces with varying fractal dimensions (between 2 and 3). The surfaces between the bodies were self-affine fractal surfaces. Their results show that, for low to medium forces, the normal contact stiffness is non-linearly connected to the force by a power-law dependence. Specifically, $K_n \propto P_N^{\alpha}$ with α ranging

from 0.51 to 0.77 [33]. The results were compared to Persson's models where a more linear relationship is observed. The validity of 'Method of Reduction of Dimensionality' has been questioned in subsequent papers, particularly by Persson [34]. Persson criticizes the method used as it effectively reduces the contact problem to a large system of one-dimension springs. Persson comments that the behaviour will differ vastly to the full interaction of a 3D surface. This results in qualitatively wrong results, particularly when applied to randomly rough surfaces that have roughness occurring over many length scales [35].

Pastewka et al. [36] performed numerical simulations of normal contact stiffness and found that results conform well to Persson's theory when they plotted a log-log plot of nondimensional stiffness, $K_n h_{rms}/E^*$against nondimensional pressure p/E^*. However, at extremely low loads, they found a power law relationship. Thus, it was concluded that this was due to the stiffness following the Herztian expression for contact of a single asperity, $K \propto p^{1/3}$. This was believed to be due to the contact diameter being smaller than the smallest wavelength of roughness on the surface [36]. This occurs at very low loads, possibly explaining the phenomena observed by Pohrt and Popv [33].

Medina et al. [7] again considered the elastic contact of rough surfaces. They developed analytical and numerical asperity models that were analysed to develop simple analytical expressions for the stiffness of contacts under tangential loading. They found that the tangential stiffness is proportional to the normal stiffness but also independent of the Young's Modulus of the material [7]. The model explores methods to predict tangential stiffness for rough elastic contacts using the expressions derived. Their model seems to work well for low loads when asperity spacing is large, but the numerical model can be inaccurate for larger loads as it predicts a reduced stiffness. The model does not include asperity interactions and these become more influential at larger loads [27]. Hence this could be why the model is less accurate at larger loads. The expression developed for tangential contact stiffness is as follows:

$$K_t = \frac{2(1-\nu)}{(2-\nu)}\frac{P}{\sigma_{rms}}$$

(2.14)

This expression applies to the no-slip case considering elastic interaction of asperity contacts and shows that the tangential contact stiffness is proportional to the applied load, inversely proportional to the standard deviation of the asperity peak heights, σ_{rms}, and depends on the Poisson's ratio of the material [7]. The expression used to define normal contact stiffness in this study was developed from the GW representation of rough elastic surfaces with no-slip as:

$$K_n = \frac{P}{\sigma_{rms}}$$

(2.15)

A stiffness ratio between K_n and K_t has been developed by Mindlin [9] and was used in this paper and by other studies to describe the ratio of the two properties and show their proportionality. The Mindlin ratio is a constant:

$$\left(\frac{K_t}{K_n}\right)_{Mindlin} = \frac{2(1-\nu)}{2-\nu}$$

(2.16)

This ratio is only applicable when two elastic bodies are squeezed together, and the surfaces exhibit quadratic surface profiles. Mindlin developed this solution for when an elastic ball was squeezed against a flat surface. This is similar to a Herztian contact and therefore it follows that this ratio should apply to contact regions between two elastic solids with Herztian contacts [9, 37]. The solution and ratio neglect elastic coupling between contacts (asperity interaction) which, as discussed, can have severe results, especially as loading increases.

Campañá et al. [9] extended Persson's theory to derive expressions for contact stiffness. They derived expressions for both normal and tangential contact stiffness and used them to form the Mindlin ratio. They explored how the ratio holds using molecular dynamics

simulations and found the results to be close to the theoretical value of the ratio with some slight scattering of results. They also the compared the theoretical ratio to experimental data presented in past papers. It was found that the theoretical value for $\frac{K_t}{K_n}$ is generally twice the value of the experimental data recorded. It was hypothesised that this could be due to the reduction of the true tangential stiffness from small slip occurring, plastic deformations, and possible adhesion [8]. These effects were not included in the model. It will be interesting to examine how the ratio holds for structured surfaces.

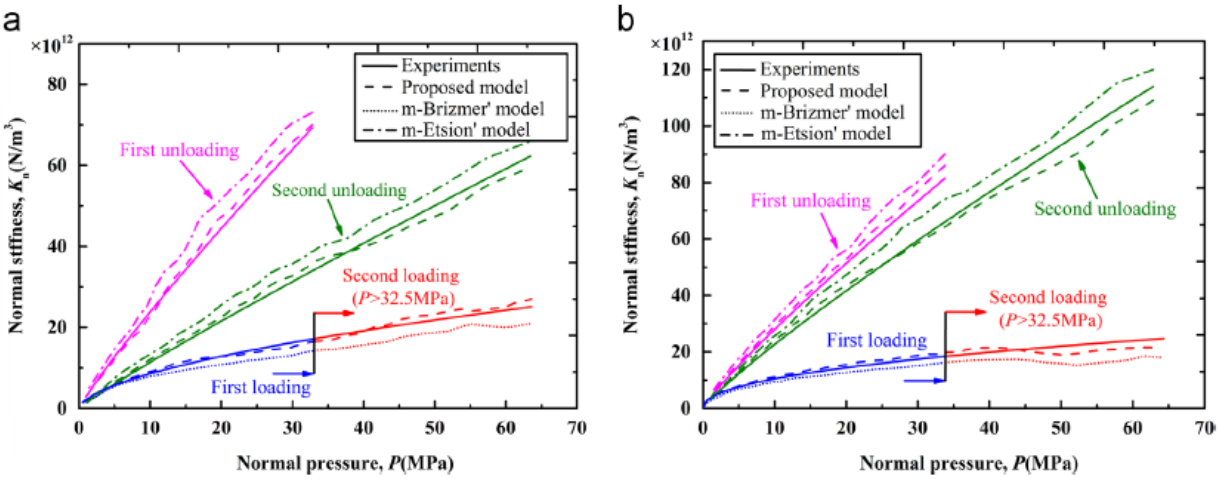

Figure 2.8 - Comparison of normal contact stiffness predicted by various models in Zhao et al and experimental data of AlZn6CuMgZr aluminium alloy (a) and 18CrMo4 steel (b). [38]

Zhao et al. [38] developed a model that aimed to consider the power-hardening behaviour of materials. They calculated the normal contact stiffness of a single asperity contact using the power-hardening of a hemisphere against a rigid flat surface and shoulder-shoulder contact of asperities. The effects were analysed and used to build a stiffness model based on specimen contact surface. The model was used to analyse the normal contact stiffness produced during loading and unloading events of the contact surfaces. The stiffness generated from the model was compared to experimental data produced by the research team as well as the contact model of Etison et al. [39] and single asperity pair model of Brizmer et al [40]. The models of Etison and Brizmer were used at unloading and loading events respectively. Zhao et al found their models to be more accurate and appropriate for predicting loading and unloading profiles when compared with experimental data and hence show the potential benefit of including the power-hardening effects of materials into contact models - See Fig. 2.8.

Paggi et al. [41] considered a tangentially loaded system. They examined the contact area, tangential force, and tangential stiffness associated with the stuck portion of the contact area as a function of the total applied tangential load. This study explored how, as tangential force increases, the stuck portions of contact reduce until eventually vanishing and sliding occurs. A numerical analysis of randomly rough, fractal surfaces was simulated by boundary element method and compared to a simulation using the Greenwood and Williamson

model. The paper found that for the GW model, there exists a linear relationship between the area of stick and the tangential force: this held true for self-affine rough surfaces with Hurst exponent values varying from 0.1 to 0.9. However, a power-law dependency was found for the BEM simulations conducted and found a strong dependency on the normal contact response. Unsurprisingly, both models showed that, as tangential force increases, more contact points begin to slip and the area of static contact reduces as does the relative tangential force. When tangential force reaches its maximum value, which is equal to the coefficient of friction multiplied by the normal force, the stuck areas of contact and the tangential sticking force disappear. As seen in many theoretical and experimental examples of the onset of slip.

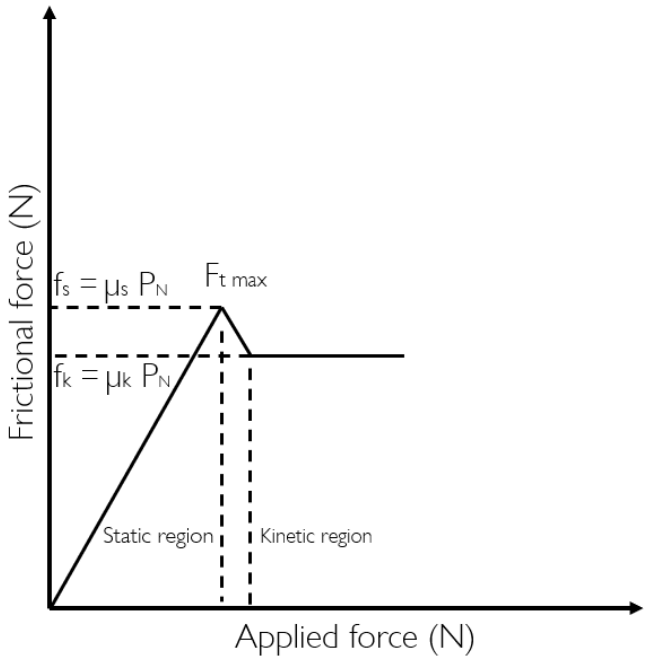

Figure 2.9 - Transition from static contact to kinetic behaviour. Static to slip transition, indicating maximum tangential force. Dashed lines indicate the applied and frictional forces that associated with the peak of the static friction regime and the onset of the kinetic friction regime.

The contact models described in this section give insight to the accuracy which can be realised through modern modelling techniques of rough surfaces. However, it also highlights the complex degree of models required to develop accurate results. This has important implications when modelling systems with many rough interfaces or modelling large areas accurately and appropriately. Large computing times and expensive equipment are

inherently linked to properly modelling complex machine surfaces in contact. If regularly patterned surfaces that have structured design with repeatable and tailorable properties can be manufactured and integrated into machine design, then the modelling of these contact interfaces can be optimised for efficiency and accuracy. The mechanical properties and operational/structural simulation of a design could be explored in a reduced timeframe with improved accuracy through microstructuring the contact interfaces.

A particularly relevant precursor study to this project was conducted by Li et al [42]. They explored the contact stiffness exhibited by a regularly patterned multi-asperity surface. A discrete model was constructed that consisted of a hexagonally patterned multi-asperity interface being pressed into a nominally flat surface. The study again highlighted the importance of the elastic interaction of asperities on a contact interface, but in a structured manner rather than for randomly rough surfaces. Observations in this study strongly suggest that the elastic interplay of the asperities on a surface play a fundamental but complicated role in influencing contact stiffness.

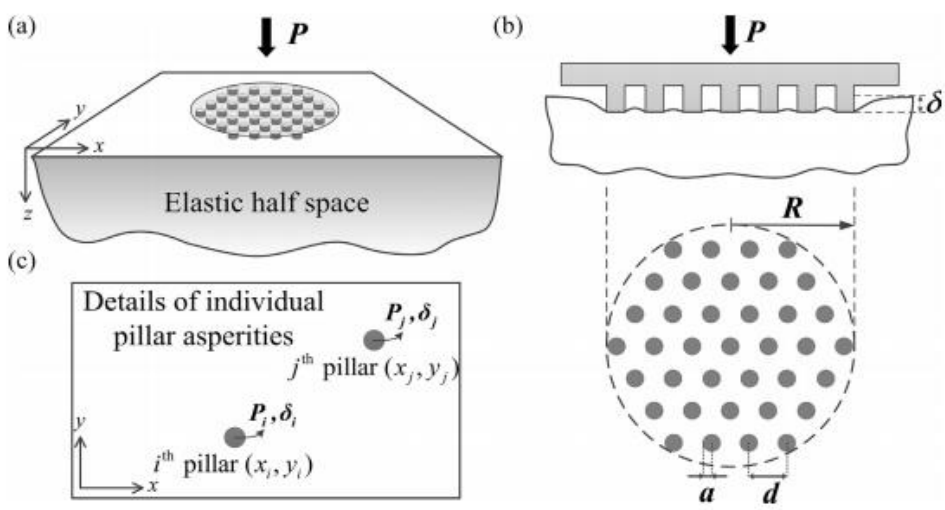

Figure 2.10 - Diagrams that detail the model developed: (a) The indenter containing the structured hexagonally patterned asperities pressing against the elastic half space, (b) Asperity interaction and normal displacement, δ, caused by the patterned surface pressing onto elastic half space, apparent contact radius R and (c) Forces and displacements experienced by individual structured asperities [42].

In the study, Li et al found that, as inter-asperity spacing increases, the normal contact stiffness increases. This can be understood by considering the elastic interaction of the

pillars. When the asperities are spaced out, there is less elastic coupling between them, and the pillars will act independently with the flat surface to cause displacement. Fig. 2.11 illustrates this point well. Contact stiffness is proved to have a strong dependence on the relative spacing, $\tilde{d}$, of asperities in contact and their number, *N*.

$$\tilde{d} = d/a \tag{1.17}$$

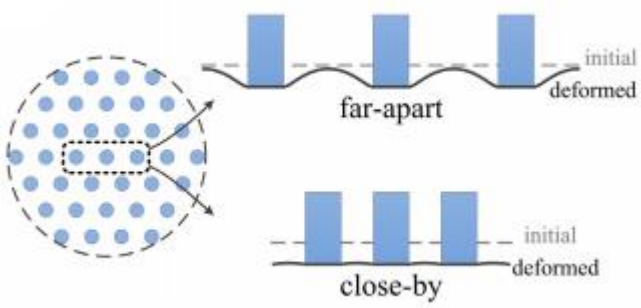

Figure 2.11 - Contact deformations under two cases where asperity pillars are either close to each other or far apart [42].

Li et al. models the contact stiffness using two respective functions that are slightly different and their accuracy depends on the spacing of the asperities. The models are named $\widetilde{K}_n^{app}$ and $\widetilde{K}_n^{iso}$. The study progressed to develop a dimensionless parameter that describes the packing of the structured asperities. Eq. 2.18 details this parameter, λ. For interfaces where $\lambda \ll 1$, the asperities can be considered closely packed and normal contact stiffness can be well approximated by the $\widetilde{K}_n^{app}$ stiffness model. The second stiffness model, $\widetilde{K}_n^{iso}$, is more appropriate when $\lambda \gg 1$ or the asperities are viewed as widely spaced.

$$\lambda = \left(\frac{3}{4\pi^2}\right)^{\frac{1}{4}} \tilde{d} N^{-\frac{1}{2}} \tag{2.18}$$

The results of the study were validated using an experiment involving structured PDMS surfaces. The models confirm that elastic interaction of asperities are important when determining the mechanical behaviour of contact interfaces. The models from this study may also be useful when trying to develop a specific contact stiffness for an interface based

on contact area, relatives spacing, number of asperities etc. Although this study was only carried out for hexagonally patterned surfaces with structured micro-pillars, the fundamental theory developed here helped to guide some of the analysis of the work carried out in this project.

2.6 Measurement of Contact Stiffness

Contact Stiffness measurement methods can be split into two main groups. These are measurement by digital image correlation (DIC) techniques (a load-deflection method), and ultrasound method.

2.6.1 Digital Image Correlation

For the load-displacement method, the load can be measured relatively simply using load cells that are appropriate to the conditions being tested - i.e. can handle the range of load measurements. The displacement (in this work) will be measured using digital image correlation techniques. This technique works by taking high resolution images of the area of interest when loading events occur. The area of interest here would be the local area either side of the interface. The images are taken of the area of interest at the beginning of loading and during subsequent increases in loading. The images will show the area of interest and how the material displaces as loading increases. The process of DIC can be divided into three steps:

1. Produce a pattern on the sample and area of interest for tracking

2. Capture images of the sample during loading events that produce movement/displacement.

3. Analyse the images to generate displacement measurements of the sample surface.

The DIC software works by taking the first image in the sequence, this is treated as the reference image, and then comparing the subsequent images taken at loading events to see how the patterns on the surface compare. The pattern displacements can then be calculated between the reference and deformed image [43].

The accuracy of DIC is strongly dependent on the pattern on the sample's surface. The pattern must cover the entire area of interest, move and deform with the sample material without exerting an influential stress on the sample and adhere well. The pattern features must be relatively random and uniform in size will produce the best results. Features that are 3 by 3 pixels on the image work best and should not exceed 7 by 7 pixels. The features of the pattern should have a density of roughly 50%, i.e. covering 50% of the surface [44]. A good greyscale level is advisable to achieve the best accuracy and reduce error from poor image quality [45].

DIC has been widely used in experimental mechanics since its development in the 1980s [45]. It can be applied to many situations from the micro to macro-scale in areas such as fracture mechanics and deformation analysis of machine components such as turbine blades [46]. DIC has also been applied to biomechanics where it can be used to measure stresses and strains on both soft and hard tissue on a micro-scale to macroscopic organ sized specimens [47].

It was Kartal et al. [14, 15] that first used DIC to measure contact stiffness and de Crevoisier et al. [48] also produced studies at a similar time that used DIC to investigate interface mechanics. These studies highlighted the effectiveness of digital image correlation in the measurement of interface stiffness. However, they also indicated that, when using DIC, there is inevitably an amount of bulk deformation affecting the results as the area of interest cannot be too close to the interface. There must be a minimum space on either side [of the interface] required for the technique to work correctly. This must be considered when applying DIC experimentally.

2.6.2 Ultrasound Method

The ultrasound method works by harnessing vibrations above the human audible range and projecting them at an interface. The ultrasound waves are typically required to be in the MHz range to be effective. Two studies have seen success using piezoelectric heads that project 2.5 MHz longitudinal and transverse waves [49, 50]. A similar study investigated the reflection coefficient for cyclic loads above the yield limit using a transducer capable of producing 10 MHz longitudinal waves [51].

The amount of ultrasound reflected from an interface is related to the contact stiffness of the interface. Ultrasound waves incident with an interface are either transmitted or reflected depending on whether there is material contact between the surfaces (rough surfaces will inevitably have areas out of contact). The wave will be transmitted in areas of contact but reflected at areas out of contact at the material-air boundary. This can be quantified using the reflection coefficient, *R*, which represents the portion of the amplitude of the incident wave that is reflected from the interface [8]. For two materials of similar properties the reflection coefficient will range from 0 to 1 (0 representing complete contact and 1 representing no contact).

The first ultrasound models were based on dynamic spring models that represented the compliance introduced at the interface of two surfaces in contact. Kendall and Tabor [52], Tattersall [53], and Baik and Thompson [54] all developed similar models. As previously detailed, the solid materials and interface can be thought of as a system of springs in series. The interface itself can be thought of as a series of parallel springs with all the connections or areas of contact contributing to the compliance of the system. If the materials on either side of the interface are the same, the expression for the reflection coefficient can be reduced to:

$$R = \frac{1}{\sqrt{1 + \left(\frac{2K}{\omega Z}\right)^2}} \tag{2.19}$$

Where K is the contact stiffness, ω is the angular frequency equal to $2\pi f$, is f the frequency of the ultrasound wave, Z is the acoustic impedance equal to ρc (product of material density, ρ, and wave speed, c). Eq. 2.19 can be applied in both the normal and transverse directions. Longitudinal or shear waves would be used respectively. This would require different types of ultrasound transducer to produce the correct waves for measurement. Eqs. 2.20 and 2.21 highlight how the reflection coefficient equation can be rearranged to calculate normal and tangential contact stiffness. The subscripts ‘n’ and ‘t’ in both the

reflection coefficient R, and wave speed, c, denote the normal and tangential directions respectively.

$$K_n = \rho c_n f \pi \sqrt{\frac{1}{R_n^2} - 1} \tag{2.20}$$

$$K_t = \rho c_t f \pi \sqrt{\frac{1}{R_t^2} - 1} \tag{2.21}$$

The concept of measuring rough surface contacts was developed several decades ago but is still investigated today. However, there is no standardised technique that can be applied to the ultrasound method. Different studies will use varying ultrasound signals and transducers to produce measurements. The experimental set ups for ultrasound measurement of contact stiffness also often vary. These inconsistencies introduce variability to the measurement process and potential differences in the contact stiffness measurements [55].

2.6.3 Comparison of DIC and Ultrasound

It is difficult to make a comparison between DIC and Ultrasound methods. This is due to many parameters becoming variable between different studies such as materials used, loading conditions, surface topography. Mulvihill et al. [12, 56] conducted a study to alleviate these problems and shed new light on which measurement method is more accurate or appropriate for contact stiffness studies. The tests focussed on both the normal and tangential contact stiffness of an interface at varying load conditions. DIC and ultrasound were used to measure the values of contact stiffness on the same interface being progressively loaded.

The DIC produced distinct load vs. displacement curves for both contact stiffness measurements. These were non-linear, indicating plastic deformation in the material and rough contacts of the interface. When measuring the tangential stiffness Mulvihill et al.

discussed the hypothesis that the ultrasound method measures the local unloading stiffness which is wholly elastic, meaning none of the plastic behaviour (plastic softening) of the interface and asperities will affect the measurements [12]. This causes the stiffness to remain constant as load increases while the DIC measurements saw the tangential stiffness decreasing as loading increased as can be expected [12, 14-15]. For the normal contact stiffness, both measurement methods observed an increase with the increasing normal loading, due to increasing real area of contact. DIC measurements were again lower: this can probably be attributed to the plastic softening of the interface measured by DIC but neglected by ultrasound [10, 12].

Mulvihill et al. found that, on average, the ultrasound was always stiffer than the DIC. This is due to the DIC technique always including bulk material within the measurement which reduces the contact stiffness measured. The ultrasound method isolates the contact stiffness of the interface without any bulk material inclusion, resulting in a larger contact stiffness. This can be seen from eq. 2.3 and 2.4. For normal stiffness at an applied pressure of 70MPa the measurements were 3.5 times larger, and tangentially they were 2.7 times larger at the same pressure [10]. The authors concluded that, while DIC has its drawbacks when used in tangential contact stiffness tests, such as detecting the micro-slips present, it should be used over ultrasound methods especially for tangential tests. DIC will be used in this study as it is perceived to be more accurate and appropriate as it considers the entire contact due to the measurements being taken along an interface and includes potentially neglected interfacial compliances. Ultrasound also has the risk of including additional compliance from the components in the experimental apparatus. However, ultrasound has its benefits and is suited to measuring the elastic unloading stiffness.

2.7 Surface Engineering

2.7.1 Overview

The advent of advanced manufacturing has generated the means and requirement for more novel and precise designs for systems and components. The need for more advanced components has restricted the use of conventional manufacturing methods. Nonconventional machining and manufacturing methods have gradually found a foothold in a

myriad of industries and research areas. Engineers are increasingly using advanced manufacturing techniques such as chemical machining processes - chemical blanking and photochemical machining, ultrasonic machining and welding, water jet cutting and machining, electro discharge machining, laser beam machining, ion beam machining and 3D printing. The list of available manufacturing techniques continues to grow and generate specialised fields [57].

Surface engineering concerns modifications to a surface that will allow a system or component to alter how it interacts with the surrounding environment. Surface engineering deals with surface texturing, coatings, and modifications. Alterations to a surface can allow for components and systems to behave more effectively and efficiently in their technological role. This section will focus on surface texturing, as this is critical to the work executed within the research project. The ability to alter a surface's texture is utilised in many fields. Through various machining and manufacturing methods, certain geometries and properties can be generated from a surface or material.

2.7.2 Surface texturing

Surface engineering can apply to large scale applications such as anti-ice, anti-insect fouling, and erosion prevention on wind turbine blades [58]. Surface texturing can also apply to very niche areas, such as generating geometrical features that mimic the topography of gecko feet for improved dry-adhesion and self-cleaning applications [59].

Periodic surface structuring is a common technique applied to many applications. A periodic structure can be generated by many techniques. Lasagni et al. [60] generated selective surfaces to improve solar absorption. The surfaces were structured using laser interference, enabling micro-structures to be fabricated on bulk materials. The aspect ratio and periodicity of the microstructures was studied. It was found that large aspect micro-structures enable an increase in solar absorption. Fig. 2.12 shows examples of the type of micro-structures that can be generated by laser interference.

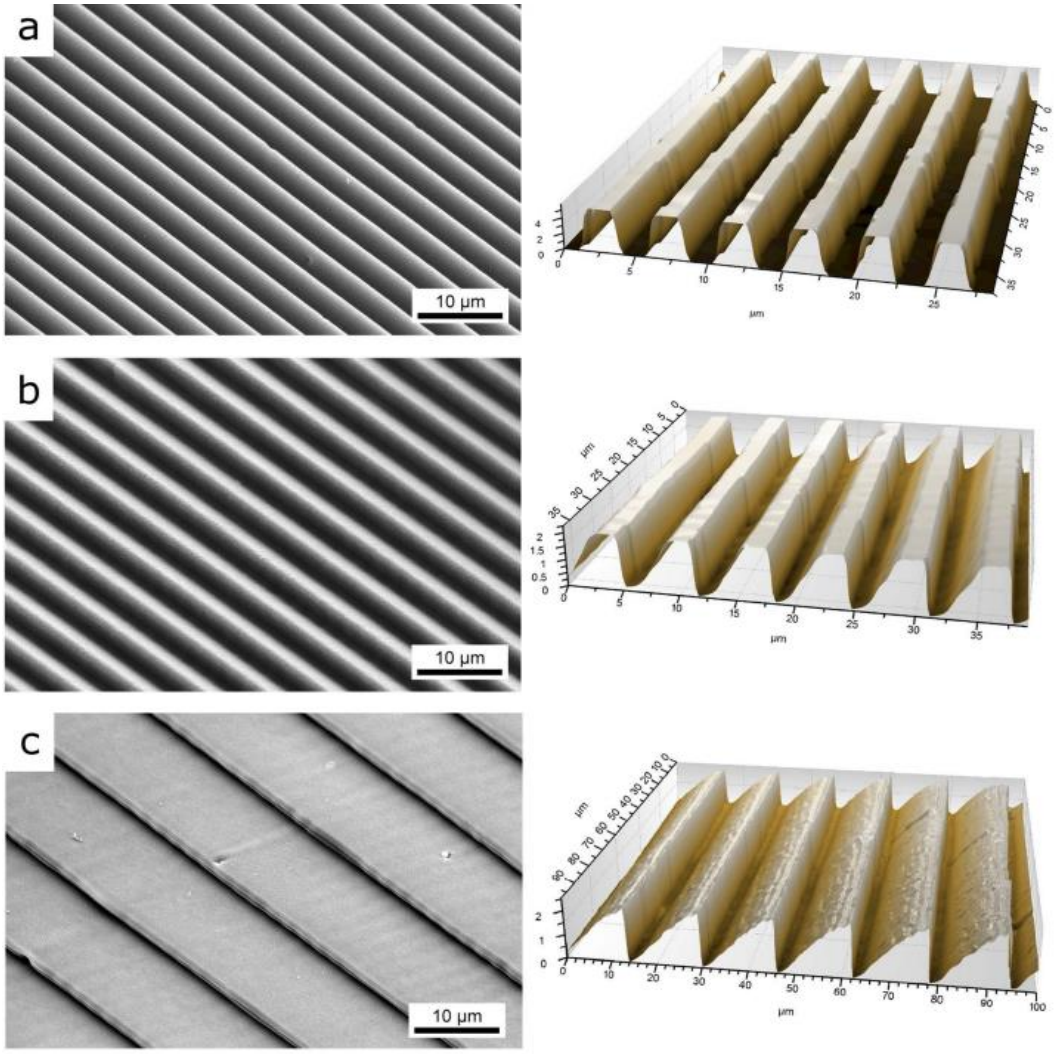

Figure 2.12 – SEM images (left) and confocal topography (right) of structured polyamide foils. Generated using a spatial period of 4.6µm, laser fluence of 1.32J/cm^2, 20 pulses per laser spot and different sample inclinations (a) 0°, (b), 45°, (c) 75° [61].

Laser structuring of polymers and metals is extremely prevalent in the field of surface engineering. It is a technique used by many researchers due to its accessibility and effectiveness. Lang et al [62] investigated the limits of resolution and speed at which regularly patterned surfaces can be produced. This type of research is particularly important as it highlights the importance of surface engineering, but also the difficulties and limitations that can be encountered. Speed and scalability are paramount in manufacturing, so elucidating ways to optimise these parameters is a key area of interest.

Surface texturing is utilised to produce specific patterns on material to improve their properties. Textured surfaces allow for improved tribological performance, biological applications, wettability, and optical properties can be tailored for specific use also.

Texturing a surface can introduce and improve anti-reflection properties [63], generate self-cleaning surfaces [64], enable superhydrophobic surfaces that facilitate anti-corrosion characteristics [65] and anti-fouling surfaces can be generated by replicating topographies found in nature [65,66]. These examples give a small insight into the expansive catalogue of novel applications that surface texturing enables. Laser structuring has far reaching applications and has been extended into optical device design [67], solar cell design and operation [68,69], and metallic joint design [70].

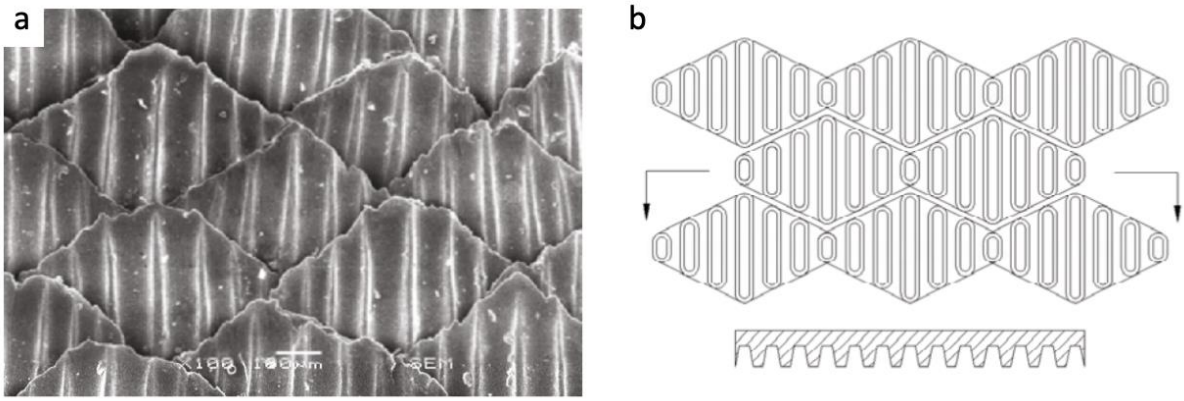

Figure 2.13 - SEM image of shark skin surface (a) Shark skin inspired micro-structured surface (b). [65]

2.7.3 Tribological applications

Tribological applications show that textured surface patterns are effective for introducing traps for wear debris, lubricant reservoirs, and micro-features to reduce friction. There has been considerable research into introducing micro-structured surfaces for tribological improvement. Laser surface texturing has been used extensively to generate structured surfaces in the hope of improving the tribological performance of materials. Applications such as improving the tribological performance of automotive components have been investigated [71-73]. Reducing friction, tailoring vibrational characteristics of interfaces, and creating wear debris traps would all facilitate improvements to the efficiency and effectiveness of the systems. Therefore, the area is of major interest to the tribological community.

Many studies have focused on investigating how the size and spacing density of microfeatures can influence tribological properties [74-79]. All found that the production of micro-pores facilitated a reduction in friction interaction between surfaces. Many

hypothesise that this is due to the reduced contact area observed when introducing micro-structured surfaces. The materials wear life was also observed to increase as the micro-structure or micro-dimple density increased. Laser surface texturing has also been applied to surfaces that experience cavitation in an attempt to improve service life. The laser surface texturing of turbine blades has been documented in many studies that show drastically improved erosion and corrosion resistance capabilities of the material [80]. This illustrates that the degradation associated with cavitation can be limited allowing for improved service life of turbine blades.

2.7.4 Microfluidics

Another prevalent and crucial area in surface engineering is the fabrication of biomedical devices. Specifically, the manufacture of microfluidic devices is a large area of research with many techniques and materials being utilised. The fabrication of a microfluidic device requires a fabrication method that can create high quality micro-features of varying size. The devices allow for small volumes of fluid to be controlled to investigate chemical, biological, and physical processes. For example, the features can generate systems of micro-channels that are often used to simulate biological environments, allowing for research into areas such as drug development. The fabrication of the devices using polymers is particularly attractive to many researchers due to the vast number of materials and versatile microfabrication methods available, polymers are often cheap, and polymers can easily be optically transparent for analysis. Injection moulding, 3D printing, and cleanroom techniques are attractive processes utilised in the fabrication of microfluidic devices. The main aim being to produce large numbers of the devices can be produced in various polymers with high quality microfeature [81-89].

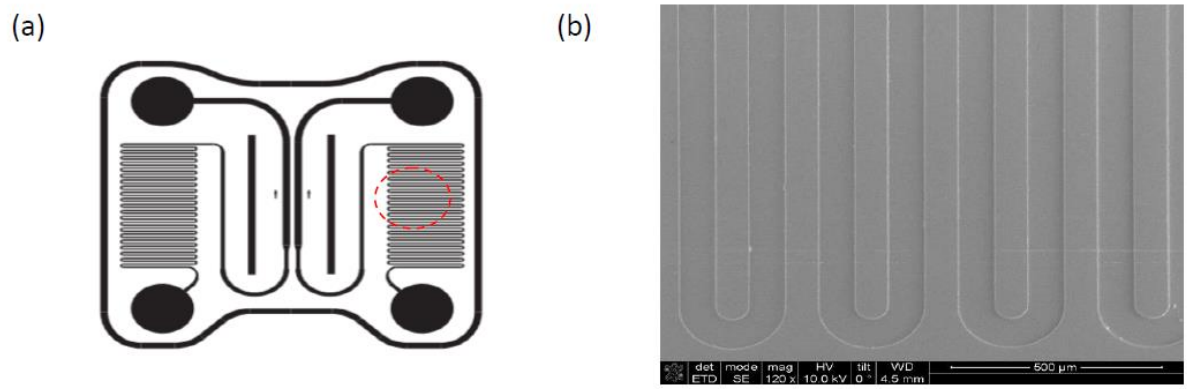

Figure 2.14 – (a) Design of microfluidic device for imaging bacteria culture under flow and (b) SEM 120x magnification image of polymer device. Red circle in (a) corresponds to region shown in SEM (b). From Hamilton et al. [90].

2.8 Manufacturing methodologies

This sub-section will give a brief overview of the manufacturing technologies that were integral to the research carried out. Each individual part of the thesis draws on different yet similar techniques, while some blended various techniques to create something new. The summaries will give a brief insight into each technique's operation and application. This information is expanded in the appropriate subsequent sections where the technology was utilised.

2.8.1 Injection Moulding

Injection moulding exhibits a myriad of benefits such as high-throughput, consistent and high component quality, design flexibility, large range of material options, and rapid component production. Typically, the manufacturing method is applied when mass production of a product is required. The process facilitates a large number of near identical components or products to be manufactured in a relatively quick process time. Initially, the manufacture method aided in the mass production of commercial products such as industrial components, polymer furniture, toys, polymer computer components etc. However, in recent decades, the manufacture method has been applied at the micro and nanoscale. Specifically, to produce micro or nano-topographies in the fields of surface engineering. Full technical details and operation methodology of injection moulding is conveyed in subsequent chapters that cover how the manufacturing method was utilised within the research of this thesis.

To facilitate high quality production of micro and nano-topographies, an adequate mould insert for microinjection moulding is crucial. However, these inlays can be time consuming, costly, and difficult to produce. Novel fabrication methods are often employed to generate the micro-topography required. Many researchers have trialled silicon mould inserts produced using well-known cleanroom photolithography techniques, but these inlays are highly susceptible to failure due to their brittle behaviour and break easily when subjected to the processing conditions associated with injection moulding [83, 90, 91, 92]. Metals have been explored extensively due to their increased strength and durability. However, their increased conductivity causes an increase in cooling rate when processing the polymer. Poor filling can be generated as the micro features can occur due to a frozen layer of polymer developing before the mould cavity is properly filled [93]. Metal inserts can typically be manufactured using methods such as micro-electrical discharge machining (μEDM), micro-mechanical milling and electrochemical machining (ECM) [94-96].

Another common manufacturing method for generating mould inlays is LIGA or UV-LIGA. This is a method used in the MEMS industry to create replicas of micro/nano topographies through electroplating a substrate pattern with a material that can be separated and used as a moulding insert. Typically, the materials can include polymers, nickel, and nickel-based alloys [97]. These methods are comparatively expensive. Hybrid inlays are another avenue that has been explored. Hybrid inlays require novel manufacturing techniques developed from various micro/nanofabrication procedures [89, 90, 98]. The inlay will normally consist of two materials or more: polymer and nickel for example. The polymer allows for lower heat conductivity, eliminating the frozen polymer layer produced during the process of injection moulding discussed earlier.

2.8.2 3D printing

3D printing is an additive manufacturing technique that allows the freedom to produce complex components or structures quickly and easily. The process involves printing materials in a predefined pattern or shape in successive layers to produce the desired component or design. The process is attractive to a wide range of engineering disciplines as it offers many benefits over conventional manufacturing methods. The recent uptake and

explosion of available 3D printing hardware, materials, and methods was largely driven by the expiration of early 3D printing related patents. This opened the door to a myriad of designs and technologies that could be utilised and developed to form the 3D printing industry we know today. Open-source technology rapidly became available and 3D printing developed from being a technology exclusively used by high end design and engineering firms for rapid prototyping into a versatile tool with wide ranging applications [99].

The manufacturing method offers many benefits over conventional methods, and this has driven the uptake and expansion into many sectors ranging from architecture and construction [100], the automotive industry (particularly novel engine components) [101, 102], aerospace components [103, 104], and biomedical engineering for patient-specific components, research, and microfluidic design [105-107].

The process of 3D printing has many benefits such as high precision fabrication of complex geometries, reduced material wastage, increased design flexibility compared with traditional techniques, and a wide range of input materials. The available materials have expanded to include polymers, metal alloys, biomaterials [108], and ceramics [109], with the list of available materials constantly growing. Various types of printing method have been developed and allow printing in various sizes ranging from micro-scale to macro-scale. The material selected and specific printing process are selected to suit the design parameters of the component. For instance, certain metallic alloys are better suited to automotive or aerospace applications, and biocompatible polymers and ceramics are utilised for biomedical applications. One crucial benefit that distinguishes 3D printing from other manufacturing methods and allows it to be so attractive to so many industries is its mass customisation. This allows 3D printing to be tailored easily to suit the required purpose and produce highly personalised design for the brief in a vastly reduced time for a lower cost. However, there are drawbacks to all 3D printing technologies. Typically, high quality 3D printing methods suffer from high initial costs for the hardware, niche materials can be required, as well as time-consuming fabrication of the required designs. These issues are recognised across the research and implementation of 3D printing as the main issues and drawbacks that must be improved to realise wider application of the technology [110].

There are a handful of processes that make up the main types of 3D printing methods. These include but are not limited to: Fused deposition modelling (FDM), powder bed fusion, inkjet printing, direct energy deposition (DED), laminated object manufacturing (LOM), and Stereolithography (SLA). Each has its benefits, drawbacks, and specific field where the method thrives and can be utilised in the most beneficial manner. This overview will give a brief description of each of these methods. The SLA method was the process utilised throughout all research projects presented in this thesis. This was due to its high-quality surface finish and extremely high-resolution printing capabilities. The process is fully detailed and explored in subsequent chapters. Diagrams of the processes are shown in Fig. 2.15.

3D printing methods:

- FDM is probably the most well-known method. FDM typically prints using polymer filaments which are heated at the nozzle and then deposited in a semi-liquid state onto a build plate or on top of previous layers of polymer to build the desired component. This method benefits from being a relatively low-cost method that is simple to implement but suffers from poor mechanical properties of the finished products, as well as poor surface finish/layered appearance [111].
- Powder bed fusion or selective laser sintering uses thin layers of powder material that are spread onto a build platform and then fused together using a laser beam or binding agent. Layers of material are rolled onto the subsequent fused layers to incrementally build the final component. The final component usually requires post-processing such as coatings or full sintering to improve the mechanical properties of the product [112]. This method offers high resolution and quality of printing, making it ideally suited for industries where high precision is key. The method suffers from slow processing and high costs, along with potential material porosity issues.
- Inkjet printing is the method typically used for printing ceramic materials. This method allows the high precision required for biomedical scaffolds. The fabrication uses ceramic suspensions (either liquid or wax-based inks) that are deposited in droplets using a nozzle onto a build plate or substrate. The materials then solidify by either evaporation or melting, for liquid or wax-based inks respectively. This method

offers high resolution prints and design flexibility, but suffers from many process variables due to its more complex nature. This can decrease the print fidelity and by extension its applicability to high precision manufacturing applications [109, 113].

- Direct energy deposition (DED) or direct metal deposition (DMD) is the method commonly used for manufacturing high performance metallic alloys. A laser or electron beam is used to focus onto a substrate material and a feedstock material at the same time. The feedstock material, a powder or filament, is melted onto the substrate in a predefined pattern to build the printed component. The materials are bonded together with the feed material solidifying very quickly. This method can also be utilised to repair existing components, such as minor cracks along with combining components that would be difficult to manufacture as one solid unit [114]. The method has the advantages of being able to bond different materials, multiaxial and high speed of deposition, and good control over the mechanical properties of the material. However, this method suffers from poor surface finish and high costs for hardware, materials, and operation [115].
- Laminated object manufacturing (LOM) is used to form structures using polymer composites, metallic sheets, and ceramics. The method works by cutting layers of material and laminating or bonding them together to form the final desired structure. Sheets of material are cut either by laser or a mechanical cutter and then bonded to the successive layers of material. The process can also be done in the opposite direction: i.e. bond and then cut. The direction of process depends on the desired product. Post-processing may be required depending on the substrate material. The process is suited to generating large precision structures and has the benefit of being available in a wide range of materials. The process is fast and requires less complex tooling than other printing methods. However, it suffers from poor surface finish and dimensional accuracy [116].
- Stereolithography (SLA) is one of the oldest printing methods and offers a relatively low-cost rapid prototyping method. The SLA process works by using a UV laser to cure photocurable resin. The laser cures and solidifies layers of the resin in a predefined pattern, building the desired component layer by layer. The unreacted

resin can then be removed once the components are completed. Post-processing is typically employed to achieve improved or desired mechanical properties. This is done by photocuring or heating. This method is desirable as it produces high resolution parts, resolution as low as 10μm [117]. However, the process suffers from a limited range of resins, the photocurable process is complex and difficult to optimise and the hardware is also typically expensive.

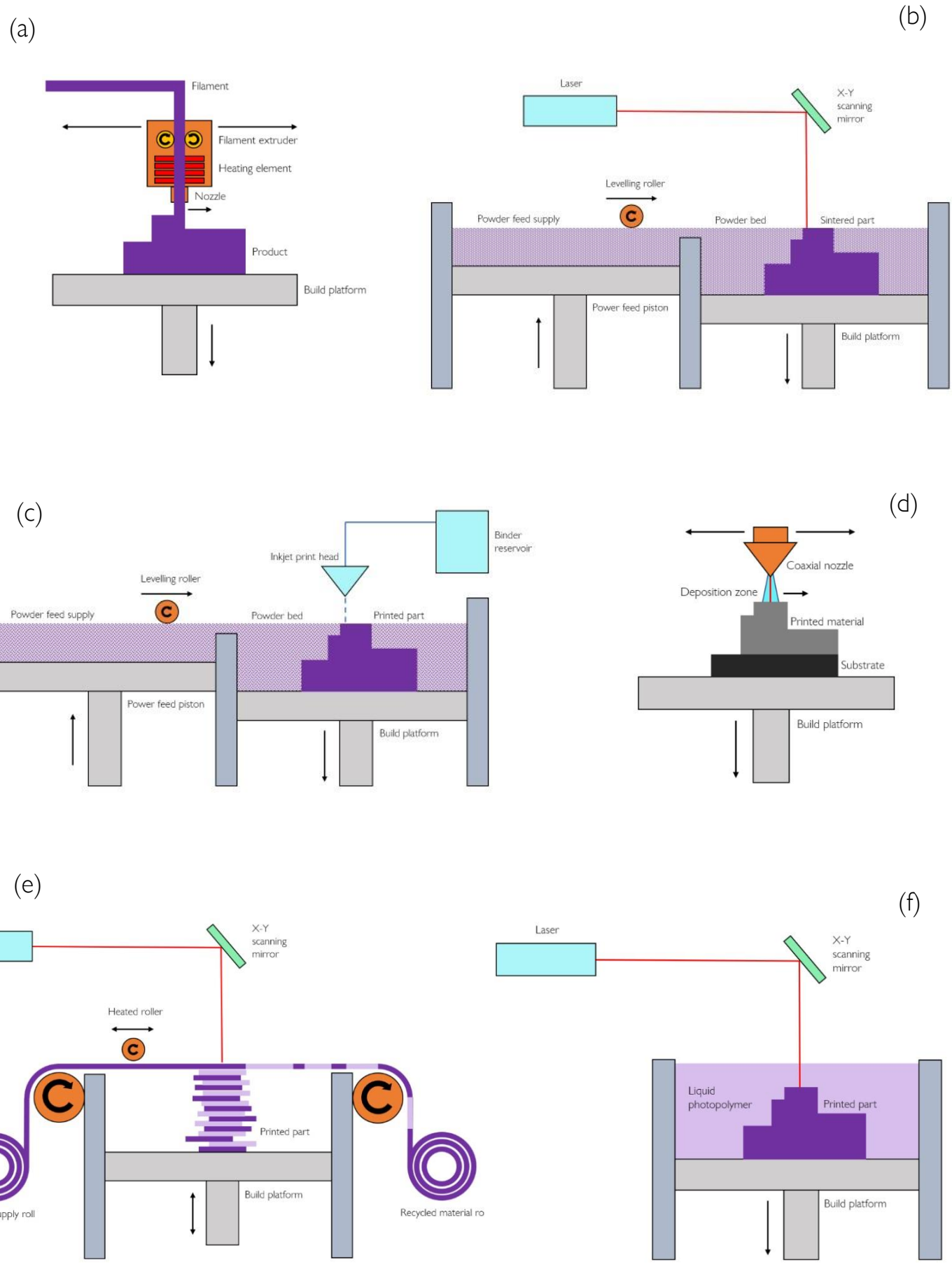

Figure 2.15 - Common popular methods of 3D print additive manufacturing: (a) Fused deposition modelling (FDM), (b) Powder bed fusion or selective laser sintering, (c) Inkjet printing, (d) Direct energy deposition (DED) or direct metal deposition (DMD) (e) Laminated object manufacturing (LOM) (f) Stereolithography (SLA).

This final section of the literature review aimed to give a snapshot at the extensive list of the various applications and techniques employed in the field of surface engineering and related manufacturing methods that were critical to the research presented in this thesis. Surface engineering and its related manufacturing methods are expansive areas of research, ever growing and finding new avenues. Many topics have been omitted, or briefly mentioned due to the sheer amount of research that falls under the larger area of surface engineering and fabrication. However, the topics illustrated in this section are closely related to the work produced during this research project and will be discussed further in future chapters.

2.9 Conclusion

A critical analysis has been performed of the available literature concerning both contact stiffness and surface fabrication. It was important to gain a wide understanding of these topics to effectively identify gaps within the research that could be explored in this thesis.

Initially a broad understanding of tribology and contact mechanics were considered. Contact stiffness is a small section of interfacial mechanics and phenomena, so it was important to analyse how it had previously been considered and explored in these fields. It was natural to first consider contact mechanics theories and interfacial interactions. This highlighted what the important factors are in rough surface interactions and how researchers contact theories differ, whether that be including plasticity, asperity interaction, or what critical parameters are used to build their models. Many researchers consider the approach of surfaces with respect to normal loading, through surface separation and an applied load. Models are often considered in comparison to experimental tests, with high similarity between the two indicating a successful contact theory. This occurred frequently in the literature, many would consider a rough surface, often arbitrary in nature, and examine how it would react under loading i.e. surface approach [3, 6, 7, 9, 11, 21]. The surfaces were often manufactured and then tested, with the main consideration being what topographical parameters were most crucial in affecting the approach of the surfaces, and how they manipulate the models performance. However, it was relatively rare to see a consideration to how roughness affected contact stiffness directly and anyone trying to control contact stiffness [32, 36]. There are always considerations of what topographical parameters affect

the approach of surfaces and which are most important, but not how we can manipulate these to advantage or control them through interfacial design. The clearest example of a demonstration of interface design to manipulate contact stiffness was by Li et al [42]. However, this focussed how microstructured asperity arrangement and their elastic interactions can affect the stiffness of an interface. It is clear from the literature that if we can develop novel fabrication methods to generate interfaces with control over both microstructured and rough surface attributes then we can exert a level of control over contact stiffness and the mechanics of an interface.

Initial studies focused on novel development of microstructured interfaces to control contact stiffness, this was then extended into rough surface fabrication and how to control topographical parameters and by extension an interfaces stiffness. Both required extensive investigation into surface engineering and structuring methods to highlight the best way to produce the required surfaces. There are extensive method of fabricating surface micro and nano topographies to generate an interface to benefit an engineering system. Whether this be laser texturing, 3D printing, photolithography/EBL, EDM etc [57, 59, 60]. The process selected will have benefits specific to the devices needs, often feature fidelity being at the top. However, there are always inherent drawbacks to any manufacturing process. Tribological processes have explored previously using micro structuring of interfaces, mainly using laser structured surfaces [70-74].

Cleanroom techniques are highly adept at manufacturing micro and nanostructured interfaces with extremely low roughness. This is beneficial to the work here as it was thought that if we can eliminate the difficult variable of roughness and isolate a microtopography that can be controlled, then the contact mechanics of a surface can be more easily controlled. However, the materials used are often fragile and do not lend themselves to mechanical design purposes. Hence, the challenge was to translate cleanroom microfabrication techniques into a durable material for the mechanical testing of an interface. A modified microfabrication technique was required to enable the manufacture of controlled microstructures in a mechanically suitable material, with a relative absence of surface roughness that would affect the contact stiffness exhibited by the interfaces. The

work in controlling microstructured interfaces and their contact stiffness encompasses Chapters 3 and 4.

Controlling a microstructured interface can enable the control of certain contact mechanics phenomena, especially contact stiffness. Much of the tribological research indicates and highlights topographical parameters that can affect contact mechanics interactions, and by extension contact stiffness. It was established that if a method of controlling rough surface interface parameters could be developed, then this could extend to control over the mechanics of an interface. Therefore, if you could manipulate a rough surface to have certain key characteristics then you could alter the contact stiffness of that interface. In previous work there are instances of researchers replicating rough surfaces and examining there tribological characteristics. Mainly the surfaces are either optically or mechanically scanned and then replicated through 3D printing [158, 159,190-192]. However, there is an opportunity that lies in being able to mathematically generate a rough surface topography with controlled user defined characteristics. The generated surface then has the potential to be manufactured through the correct process and enable the control of certain mechanical interfacial properties, such as contact stiffness. These concepts are the foundations of the work in Chapters 5 and 6. This literature review serves as a guide to the research that has informed the initial concepts that developed into the research projects outlined in the subsequent chapters.

Chapter 3.

Fabrication of micro-structured interfaces

3.1 Introduction

One of the major initial aims of the research of this thesis was to develop microfabrication routes that would enable the production of micro-structured polymer interfaces. These interfaces were produced to aid in the understanding of the mechanical behaviour of micro-structured surfaces. Conventional rough surface interfaces present challenges across engineering design and are often considered a weak link: their behaviour is often unpredictable and unrepeatable. This behaviour makes them difficult to optimise, especially for mechanical engineering applications. By extension, engineering solutions can be hampered if interface behaviour has not been fully considered in the design of a system.

Nano and microfabrication techniques allow for non-random structured interfaces to be produced. These interfaces can then be utilised in a combined experimental and modelling approach to develop a deeper understanding of their fundamental behaviour. The final aim is to produce micro-structured polymer interfaces that will have predictable, repeatable, optimised, and tailored mechanical properties. The property chosen to then assess tailorability in this work is the contact stiffness of the interface.

A well-defined microfabrication process and protocol was designed to allow the production of microstructured polymer interfaces that could be designed and tuned to the users specifications. This involved developing an understanding and practical knowledge of key cleanroom micro-fabrication techniques and integrating them to develop a new process to suit the requirements of this research. This chapter will give a brief introduction to the techniques utilised, followed by a detailed analysis of the capabilities of the micro-fabrication process that was developed to produce the micro-structured polymer interfaces. The

fabrication techniques that were explored and integrated were photolithography, silicon dry-etching, nanoimprint lithography, and injection moulding. Various metrology techniques were required to perform the analysis of all produced interfaces. All cleanroom techniques were explored and carried out in the James Watt Nanofabrication Centre (JWNC). With subsequent and related work executed in the Materials and Manufacturing Group (MMRG) labs.

3.2 Silicon master fabrication – Photolithography and silicon etching

In the field of micro-electromechanical systems (MEMS), a typical starting point is to design and fabricate a micro-structure on a silicon substrate. Patterning of materials and surfaces via lithographic methods allows structures to be synthesised on a nano or microscale. The interfaces examined in the research here were characterised by features in the microscale in the order of 50-100 microns. Photolithography was the process that was used to define a predefined pattern that would form the micro-structured silicon master. The process typically gives good resolution down to 1-2 μm.

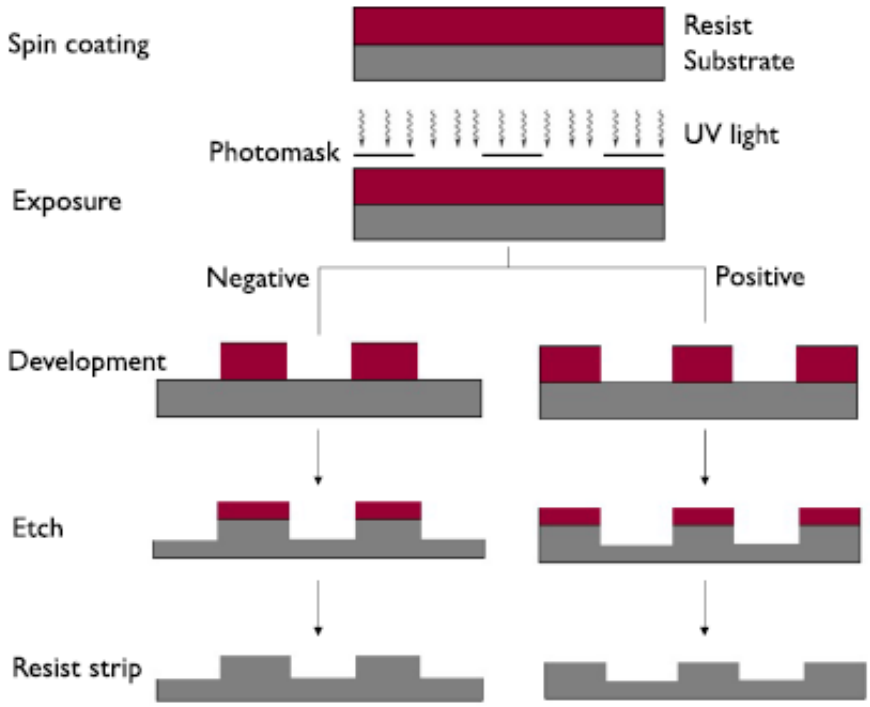

Figure 3.1 - Simplified photolithography and etching process utilised in the silicon master fabrication [118].

The photolithography process begins the developed microfabrication route. Photolithography works by exposing photosensitive materials, or photoresists, through

predefined patterns on photomasks. The photoresist is spun onto a silicon substrate and then exposed through the photomask to produce a defined pattern on top of the silicon. This allows the transfer of the designed pattern to the photosensitive material. The UV exposure of the resists causes a chemical change in the material – resulting in positive photoresists becoming soluble in photoresist developer and unexposed resist material remaining insoluble. The opposite effect occurs for negative photoresist materials. The remaining photoresist can then guide subsequent treatments of the substrate to produce the desired microstructures in the silicon. All photolithography was carried out using the Karl Suss MA6 mask aligner in the JWNC. The optics in this mask aligner are designed to give an output of midrange UV light (~250nm). The process of photolithography is shown in Fig. 3.1. The photoresist that was used in the photolithography process was SPR 220-7. This photoresist was utilised due to its ability to produce high resolution features and previous use in generating relatively large height microfeatures, ~100µm. The protocol for the photolithography process using SPR 220-7 is as follows:

- Photoresist spinning and pre-exposure treatment
    - Solvent cleaning of silicon sample in acetone, methanol, and isopropyl alcohol (IPA) for 5 minutes each, using agitation via an ultrasonic bath.
    - Dehydration bake at 180°C for 5 mins. Let substrate cool gradually outside the oven by placing into a watch glass also heated to 180°C.
    - Expose to O_2 plasma for 2 mins for 80W.
    - Spin MCC 80/20 primer using a syringe to dispense ~2ml onto the wafer. Spin the primer at 4k rpm for 5 seconds. Followed by a N_2 purge to remove any remaining ammonia.
    - Spin SPR 220-7 at 3k rpm for 30s.
    - Let substrate undertake a 30 mins solvent evaporation delay.
    - Soft bake at 118°C for 90s, transfer to watch glass heated to 120°C allowing to cool gradually.
    - Allow the sample to sit for 1 hour to enable photoresist rehydration.

- Photolithography and development
    - Exposure in MA6 mask aligner for 22.5s. Leave exposed substrate to rehydrate for 1 hour.
    - Post exposure bake at 118°C for 90s, transfer to watch glass heated to 120°C allowing to cool gradually.
    - 20 mins delay preventing thermal shock to wafer and photoresist.
    - Develop in CD-26 developer for 2 mins. Rinse in deionised water for 2 mins.
    - Hardbake at 125°C for 10 mins.

All the parameters listed in the fabrication protocol can be altered slightly depending on the nature of the microfeatures required. Once the required pattern has successfully been transferred to the photoresist, then the coated silicon substrate is ready to be etched. Two types of dry etching were used when exploring the capabilities of the process. These will be briefly detailed, and their capabilities analysed in subsequent sections of this chapter.

Dry etching is a destructive process used in nano and microfabrication to remove material by means of subjecting exposed areas of a substrate material to high energy plasma. The process gradually destroys the exposed areas and etches downwards into the substrate. The exposed areas are predefined through the photolithography process previously detailed. The two etching processes that were utilised in this research were the widely known Bosch process and a mixed etching process. The different combination and ratios of passivation and reactive ions of the gases used in the etching process control what type of profile and angle will be etched into the substrates surface.

3.2.1 Bosch process etching

This type of etching is a well-established process that is widely used in the MEMS community. The Bosch etch process provides a controlled approach that facilitates a highly directional process resulting in high aspect feature fabrication. The process allows for high selectivity between the applied photoresist and silicon substrate, allowing for a high etch rate. The process works by switching between reactive and passivation phases. The reactive phase facilitates the ion bombardment of the exposed silicon, which is then removed from the substrate. While the passivation phase protects the exposed side walls of the etched

features by depositing a protective layer. This etch process was enabled by an inductively coupled plasma tool, STS ICP (JWNC). The tool uses octoflurocyclobutane (C_4F_8) during the passivation phase of the etch cycle – applying the protective layer. While the destructive etching uses sulfur hexafluoride (SF_6). Initially the protective layer will be removed during the reactive stage, followed by flurorine free radicals reacting with the exposed silicon substrate. This cyclical chemical etching process results in a highly vertical features with a nano-serrated sidewall. A process schematic is shown in Fig. 3.2. It is possible to alter the size of the serrated side wall profile by altering the etch stage parameters. The scalloped edge can have direct implications in surface replication from Bosch etched substrate: this effect can make it difficult to separate a replication material from the silicon microfeatures. This is further discussed in subsequent sections of this chapter.

3.2.2 Mixed process etching

To allow for improved separation from the etched silicon microfeatures, a modified etch recipe can be used. The mixed etch process results in a slightly sloped profile, giving the microfeatures a draft angle of ~10°. During a mixed etch process, the reactive and passivation stages of a traditional Bosch etch will occur at the same time. This limits the effect of the serrated side walls and introduces a desired draft angle. However, the mixed etching process cycle results in a reduced selectivity between the applied photoresist and the exposed silicon substrate. By extension this reduces the process' etch rates, meaning features of high depths are more difficult to achieve as thick layers of correctly processed photoresist are required to protect the substrate effectively.

The draft angle produced in the microfeatures follows the same principal of traditional manufacturing techniques such as casting into moulds. Draft angles allow for easier separation and reduced adhesion between the cast material and the mould. The etched features with a slight slope enable a simple separation mechanism between the replication material and micropatterned silicon master. This is integral in the fabrication process developed for generating micro-structured polymer interfaces.

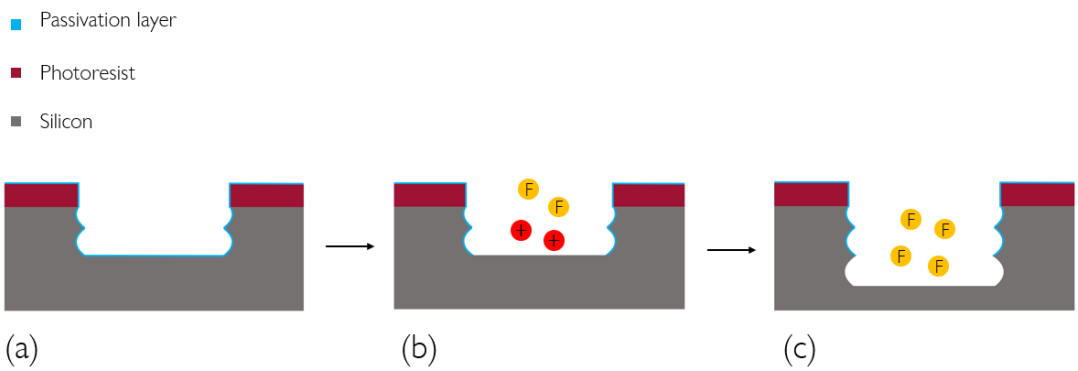

Figure 3.2 – Process diagram illustrating a typical Bosch etching process. The passivation stage deposits a layer that protects the exposed silicon from etching, C_4F_8 plasma forms the passivation layer (a). The passivation layer is then etched vertically using ions (red) which are attracted to the surface via an electrical potential difference (b). The exposed surface of silicon is then etched by SF_6 plasma (orange) while the side walls are protected by the passivation layer (c). These phases of the etch cycle are repeated until the required depth is achieved.

3.3 Injection moulding and nanoimprint lithography of micropatterns

The micro-structured silicon samples have a very consistent and repeatable profile but are not suitable for mechanical testing as the material is very brittle due to its mono-crystalline structure. Micro-structured polymer surfaces are less fragile and suitable for mechanical testing. Injection moulding was selected to produce micro-structured polymer surfaces. Injection moulding allows for the rapid manufacture of polymer components, particularly thermoplastics, from machined moulds. The initial mould costs and machining equipment are expensive. However, the injection moulding process is popular for mass produced components and products due to the high throughput of products, repeatability and quality, and cheap production costs.

To produce a micro-structured polymer surface via injection moulding, a suitable inlay must be produced. The inlay for the mould cavity in the injection moulding machine must be of suitable quality and material properties to produce repeatable structured surfaces on a micro-scale of good quality. The inlay must be able to endure the intense pressures and temperatures induced by the process of injection moulding. A micro-structured inlay for injection moulding was produced using the EVG 6200 Automated nano-imprint lithography system (EV Group, Austria). The injection moulding unit used for producing the polymer

samples was the Victory 28 fully hydraulic injection moulder (Engel, Austria), shown in Fig. 3.3.

Figure 3.3 - Engel victory 28 injection moulding unit.

The production of the injection moulding inlay used begins with the etched silicon wafer produced by the photolithography process previously described. Fig. 3.4 shows a simplified fabrication route of the micro-structured polymer interfaces. The inlays produced by the EVG nanoimprint machine consist of a PET sheet and cured imprinted working stamp material. The two materials together form a micro-structured EVG foil. To begin the process, an anti-stick layer is applied to the patterned silicon master to facilitate easy separation of the cured imprinted material. The working stamp solution is a proprietary material similar to PDMS, an elastomer widely used in the MEMS industry. This is spun onto the silicon substrate on top of the anti-stick layer. The prepared silicon master is placed in the nano-imprint machine and a PET sheet is brought into contact with the coated substrate. An imprinting roller then presses the PET sheet into the silicon master ensuring complete contact and the working stamp material is distributed effectively. Once all materials are sufficiently in contact, a UV lamp is then used to cure the working stamp material for 10 minutes. After curing, the materials can be removed from the machine and the cured EVG foil can be peeled from the silicon master. The EVG foil produced contains a mirrored micro-structure of the silicon master. The structured foil can then be laser cut to appropriate size and used as an inlay for injection moulding.

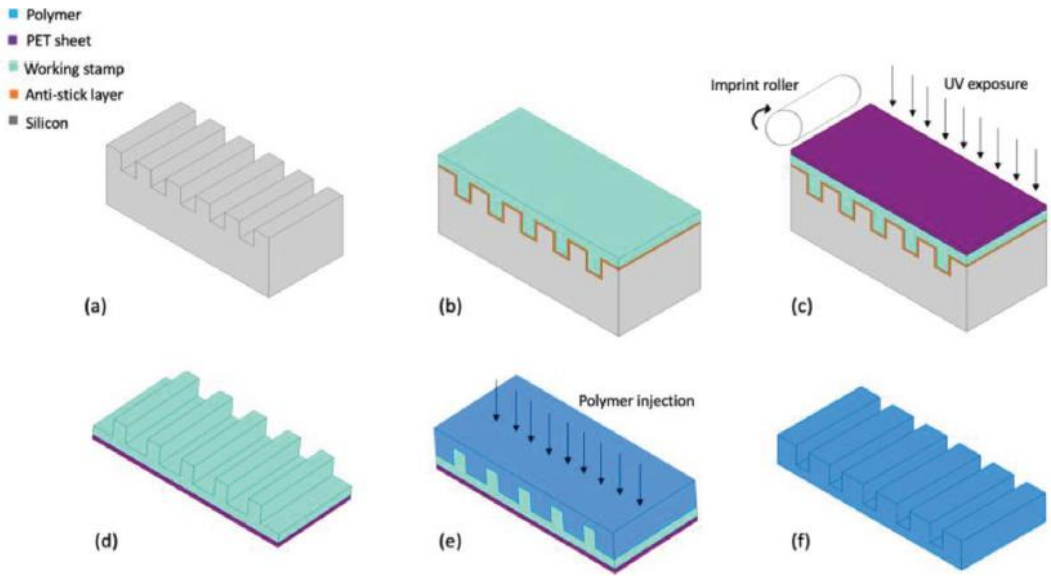

Figure 3.4 – Injection moulding and mould inlay fabrication overview: (a) Micropatterned silicon master, (b) working stamp imprint material is spun on top of the initial anti-stick layer (orange) to allow for separation of materials, (c) micropatterned features on the silicon are imprinted to the polymer working stamp, followed by the UV exposure to cure the imprint material, (d) separation of the hybrid polymer inlay with inverse micropattern to be used as moulding inlay, (e) polymer injection moulding using mould insert, (f) produced polymer micro-structured interface with same pattern as the silicon master.

This inlay production process of nanoimprint lithography is typically used to replicate nanofeatures; as such, it was necessary to slightly modify the process for the replication of the silicon microfeatures. The imprinting polymer material that is initially spun onto the silicon master to facilitate the replication of the features is normally spun at extremely high speeds, ~4k rpm, to ensure correct filling of nanofeatures. For replication of microfeatures, the polymer resin is spun at significantly lower speeds, 1-1.5k rpm, to allow for a thicker layer of the polymer layer for imprinting.

2.3.1 Injection moulding cycle

In a conventional injection moulding cycle, the prepared thermoplastic is fed into a hopper which funnels the material into a large screw. In the screw, the polymer is gradually heated along a barrel into a liquid state as it moves towards the mould cavity. This process is called plasticising. The liquid polymer is then 'shot' into the mould cavity at a programmed velocity and pressure so that it fills the cavity determined by the mould inlay and tooling. The injection speed and pressure vary depending on mould material, inlay topography/features, and the polymer being used. A simple schematic of an injection moulding is shown in Fig. 3.5. There are many factors to consider when injection moulding:

• Injection speed

• Tooling temperature

• Holding pressure

• Melt temperature of polymer

• Cooling time

• Moisture of polymer

These parameters need to be optimised for the best results when processing polymers. If the parameters are not treated with care, then poor-quality components are produced and the efficiency of the process is reduced. Generally, plastic manufacturers will provide injection moulding guidelines for polymers which can be applied. However, these often need to be modified depending on inlay material and tooling temperatures etc.

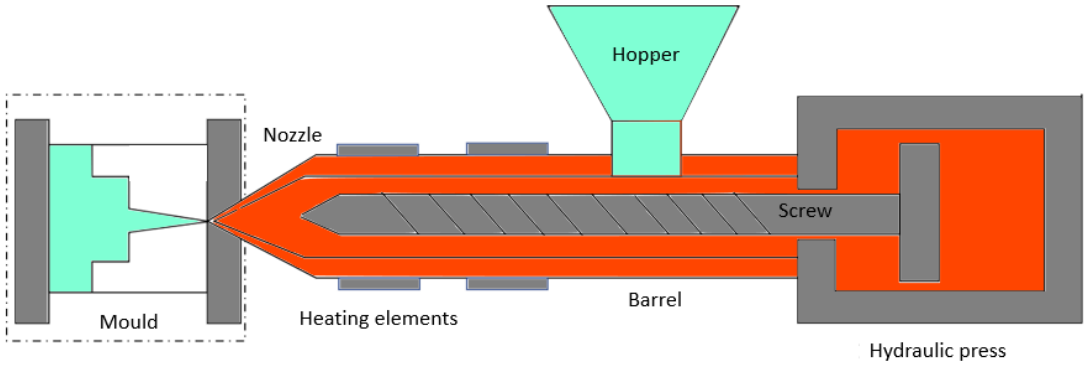

Figure 3.5 – Simplified schematic of the internal machinery and main components of an injection moulding machine.

Optimising the listed parameters is crucial to ensure the sufficient filling of the microfeatures of the mould inlay. This ensures high part quality and geometric accuracy of the microfeatures. This is essential to ensure the parts in a moulding cycle have high identicality. In the initial development of the fabrication process, the thermoplastic selected for moulding was polycarbonate (PC). PC (Makrolon OD2015) was selected due to its simple processability and high melt-flow rates. The material is often used in nano and microinjection moulding as it provides excellent replication capabilities, making it ideal for the replication of microfeature designs of the polymer interfaces. A list of the moulding

parameters used for the polymer interfaces and subsequent design studies on the fabrication method are listed in Table 3.1.

Table 3.1 - Injection moulding parameters for polycarbonate (PC) micro-structured interfaces

Injection mould parameter	Value
Melt temperature (°C)	270
Tool temperature (°C)	60
Injection velocity ($cm^3\ s^{-1}$)	18.3
Holding pressure (bar)	1400
Holding time (s)	8
Cooling time (s)	15
Shot volume (cm^3)	4.5

Before the polycarbonate can be plasticised and shot into the microcavity with the structured inlay by the moulder, it must be dried for a minimum of 2 hours at 110 °C. This should ideally be done in a vacuum oven to ensure the best results. There were two sets of tooling available (in the lab) to house any inlays for injection moulding. These measure 25 mm x 25 mm for the smaller tooling, with the larger slide tool fitting measuring 75 mm x 25 mm. The components measure 2 mm and 1 mm respectively for the available tooling.

The parameter values listed were developed to ensure high quality replication and part quality. The holding pressure listed here is relatively high compared with conventional moulding parameters. This allows the process to minimise the effect of polymer shrinkage and reduction in replication quality as the component cools following injection. The holding and cooling time can also be increased if the replication quality is not up to the desired level. Typically, the tooling temperature would be at 80 °C which inhibits the polymer freezing before correct filling of the microcavities. However, this was lowered to prevent damage to the hybrid polymer inlay [89, 90]. Metal inlays such as nickel inserts etc. can easily withstand the increased tooling temperature, but polymer hybrid inlays are more fragile and susceptible to damage under the intense pressures and temperatures associated with injection moulding cycles. The parameters listed in Table 3.1 were optimised over

several manufacture cycles specifically for the micro-structured polymer interfaces to ensure the best replication of the designed microfeatures and part identicality.

Table 3.2 - Engel victory 28 specification capabilities.

Specification parameter	Value
Maximum injection pressure (bar)	2200
Maximum clamping force (kN)	280
Screw diameter (mm)	18
Maximum barrel temperature (°C)	450
Minimum tool temperature (°C)	~15
Maximum shot volume (cm^3)	15

3.4 Metrology and characterisation

Throughout the fabrication process, the produced silicon masters, hybrid inlays, and moulded polymer samples had to be inspected and analysed to identify the key dimensions of the microfeatures produced. Two methods were used to analyse the samples. The quantitative analysis was performed using optical profilometry. This allowed feature heights, widths, feature spacing and feature top roughness to all be analysed. This method provides a full quantitative analysis of the feature dimensions and by extension the replication quality through the fabrication process developed. Scans were taken at five key locations over the course of the sample to allow multiple measurements of the critical dimensions. Each scan can provide many measurements. At least 25 individual measurements were gathered per sample. Multiple samples from the moulding run were analysed to ensure there was not significant degradation of the inlay and quality of the polymer parts produced. The samples selected from the moulding run depended on the feature design and desired output from the design study. These data sets will be discussed and analysed subsequently in a case-by-case basis. The second type of analysis used was scanning electron microscopy (SEM). This metrology method was used as both a qualitative analysis method, allowing accurate visualisation of all samples involved, but also the comparison of the results from the SEM images allowed the verification of the quantitative results from the optical profilometer.

3.4.1 Optical profilometry

Two types of optical profilometer were used. The Contour GT optical profilometer, (Bruker, Germany) and the Alicona InfiniteFocus 3D optical profilometer (Alicona, Austria). The Contour GT is more suited to structured samples while the Alicona InfiniteFocus is designed for rough surface analysis.

Both profilometers are high resolution microscopes that operate using a white light interferometry to build high resolution 3D images of the scanned areas of the samples. The profilometers allows analysis of both line profiles and areal surface scans to facilitate the calculation of topography parameters required. Both systems work on the same scientific principles, detailed below. Table 3.3 details the critical capabilities of the optical profilometers.

Table 3.3 - Optical profilometer critical lenses and vertical resolution

	Contour GT-X8	Alicona InfiniteFocus
Objective lenses available	1x, 1.5x, 2x, 2.5x, 5.0x, 10x, 20x, 50x, 115x	x2.5 x5 x10 x20 x50 x100
Vertical resolution	0.01nm (laser-controlled reference system)	2300nm x2.5 10nm x100

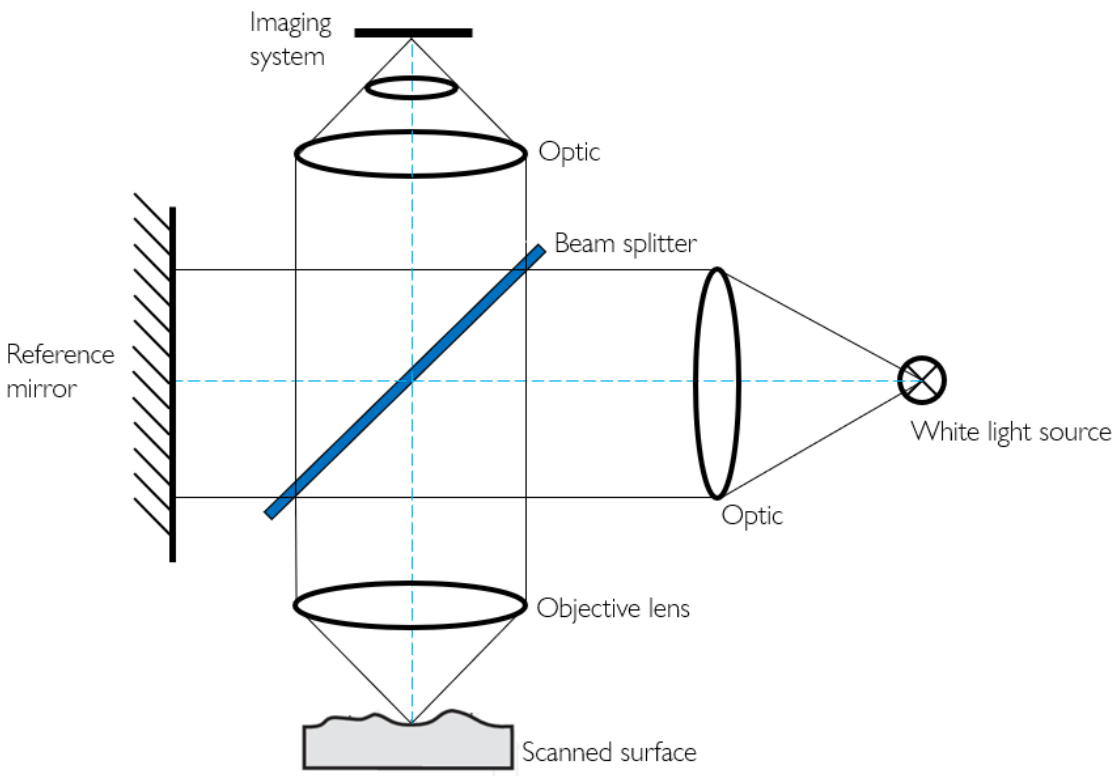

Figure 3.6 - Optical profilometry scanning system. General schematic of the optical system used to build 3D images of scanned surfaces.

The white light source is passed through an optical system which splits the beam creating a reference signal and then another scanning signal that is directed towards the sample. The beams are combined via the optical system and directed towards the computational imaging system and digital sensors for processing. From here, the signal is used to build a 3D image of the surface. Typically, the depth of field of all the objective lenses is incredibly short so the system builds the 3D image by moving the system vertically, capturing images as it moves through the set z-axis range of the scan. The systems software can then process the data to build a full 3D dataset of the scanned surface by identifying the in-focus areas of each image. The system can also move in the *x* and *y*-directions to allow for stitched images of larger areas to be constructed. The lateral sizes of the image decreases as the objective zoom value increases. This means that, the higher resolution scans take far longer to capture compared with the lower resolution objective lenses.

3.4.2 Scanning electron microscopy

A SEM is a microscope that uses electrons to produce an image of a scanned sample rather than UV visible light. This means that smaller details of surfaces or items can be identified using an SEM. It is common for features of the order of a few nanometres to be scanned and visualised using these types of systems. A SEM will typically operate in vacuum conditions to ensure a steadier stream of electrons incident with samples. The stream of electrons is directed at a conductive sample and detectors within the SEM will detect x-rays, backscattered electrons and secondary electrons. These signals produced from the raster scan of electrons incident with the sample can be used to generate greyscale visual images of the desired objects. The process is a serial process due to the nature of electron beams. Care should be taken with particularly fragile samples as they can be damaged by the firing of electrons at their surface.

The samples being scanned need to be conductive to ensure the correct interaction of the electrons with the objects surface. Metal samples do not require preparation and are typically fine for SEM analysis. Materials that do no exhibit conductive properties can be surface coated with a light metal deposition. In the JWNC a light gold coating was used to coat any polymer samples that required analysis. The JWNC at Glasgow University provides a range of SEM systems. However, the FEI Nova NanoSEM 630 was selected for all of the scans carried out for this work. It provides excellent images down to an extremely low nanoscale, ~20nm and supports an intuitive user interface.

3.5 Results and analysis

Once the fabrication process was refined and perfected, the polymer samples for contact stiffness research could be produced and mechanically tested. However, it was decided that it would be of benefit to test the capabilities of the fabrication process using a design study to fully investigate the process. It was decided that an aspect ratio and feature spacing study would be carried out to study what range of microfeatures and designs could be achieved using the fabrication process. The design study involving aspect ratio and microfeature spacing was executed using the mixed process etched silicon masters. The mixed etched masters were used as this etch process allowed for a draft angle (of the microfeatures) which better allows the separation of the hybrid inlay copy and part ejection of the polymer copies during the injection moulding process. In other words, these silicon masters are optimised for use in the developed fabrication process and can demonstrate the best level of the capabilities of the process. This study allowed the process to be fully characterised.

Once the design study was achieved and analysed fully, the research shifted slightly to focus working with Bosch etched silicon masters and their integration into the fabrication process. Bosch etch capabilities are far more widespread and accessible when it comes to cleanrooms. A Bosch etch is typically a standardised process that can be achieved easily in cleanrooms. Unlike the mixed process etch with a designed draft angle, this process is bespoke and required extensive research before it could be achieved by the technicians in the JWNC. It was felt necessary to show that microfabricated designs produced using Bosch etch techniques could be utilised in the hybrid inlay replication and by extension the injection moulding of polymer replicas. The integration of Bosch etches as a starting point of the process highlights that the fabrication process is incredibly versatile, but also able to be achieved with standardised tools and processes (rather than just with highly specialised techniques developed within the JWNC). Fig. 3.7 shows SEM images of both the mixed etch and Bosch etch profiles to illustrate the difference in the sidewalls of each type of silicon etching.

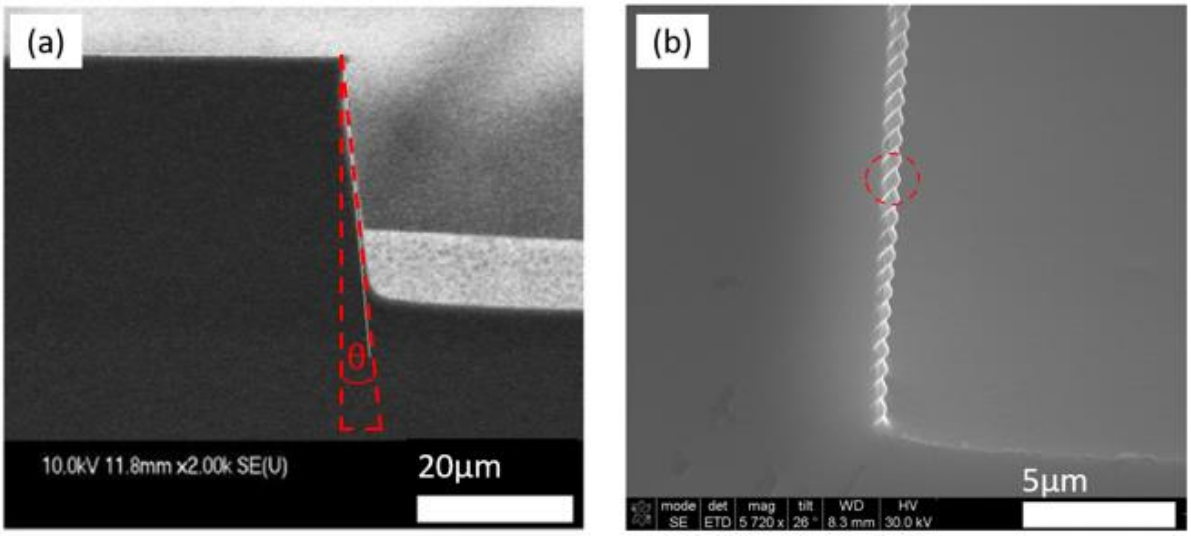

Figure 3.7 – Cross sections SEM images of the two etching types used. (a) Mixed dry etch process, providing sloped sidewall critical for improved inlay and moulding replication. Draft angle, θ, is 10°(b) Bosch etch process, image shows nanoscale scalloping induced by the two phases of the process. Red circle indicates scalloped region.

Fig. 3.7(a) exemplifies the smooth side wall provided by the mixed process etching. This type of draft angle is typically included in casting moulds or replication moulds where easy separation of the master and the inverse replica is required. The scalloped sidewall shown in fig. 3.7(b) causes difficulty when separating replicas from the silicon master. The serrated edge causes increased adhesion and stress concentration points that result in damage to the replica component material and sometimes even the master. This is further discussed in the Bosch process replication section.

3.5.1 Aspect ratio characterisation

An aspect ratio study was performed to further understand what could be achieved using the microfabrication route developed. High aspect ratio features are desirable in the MEMS community and are typically easily achieved using well established silicon etching protocols [119]. Along with integrated photolithography techniques, production of high aspect ratios microfeatures for a generation of components is enabled: such microfluidic devices [120, 121], micro-gears [122] etc.

The imprint stage for the hybrid inlay production uses the EVG nanoimprint tool, as previously mentioned. This equipment was developed to replicate features that are on the micro to nanometre transition stage. The fabrication process developed in this work aimed to achieve features in the region of ~50-100μm. This meant that the tool was being used in previously unexplored avenues as the height of the features being replicated were considerably larger than what the tooling was designed for and previous fabrication routes. The adapted nanoimprinting and polymer injection moulding stages of the process needed to be tuned and optimised for the fabrication process as it was developed. This meant the process had to be analysed to understand what the limitations of the replication were. Investigating what aspect ratio features could be replicated was an essential study to quantify the capabilities of the fabrication process, especially for the MEMS community.

The first step in the process characterisation study was to design a photo mask that would allow the fabrication of a range of aspect ratios in the silicon master. The required silicon master can then be generated for use in the microfabrication protocol. It was decided that microfeatures exhibiting aspect ratios ranging from 0.5 to 4 would be fabricated. If these initial designs could be achieved, then higher aspect ratio features would be designed and fabricated. The initial design of the microfeatures is shown Fig. 3.8. All design dimensions are given in Table 3.4. The feature length is determined by the photomask design, while the height of the microfeature is controlled by the etch depth into the silicon substrate.

Table 3.4 – Dimensions of designs for silicon master for aspect ratio study.

Aspect ratio, AR	Feature length (μm)	Feature height (μm)
0.5	160	80
1	80	80
2	40	80
4	20	80

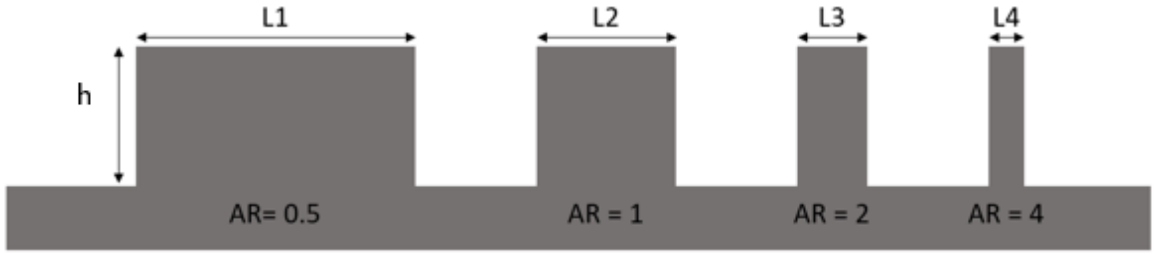

Figure 3.8 - Silicon master design for the aspect ratio study. Feature length is represented by all L variables. Feature height is represented by h.

The design shown in Fig. 3.8 was the silicon master that was used in the imprinting process to produce the required hybrid inlay, followed by the polymer injection moulding. The etch across the silicon master is typically uniform so it was felt easiest that aspect ratio should be controlled by the length of the width. Therefore, the design of the photomask had microfeatures designed to measure 160, 80, 40, and 20μm. These were then etched to a depth of 80μm to produce microfeatures in the silicon that exhibited aspect ratios of 0.5, 1, 2, and 4. The designs on the photomask were grouped by aspect ratio into an array of microfeatures with the same length. The designs measured 10mm x 10mm to give adequate features of each design for measurement. Once the silicon master was produced, it was optically scanned at various points to allow the produced features to be measured before replication. The hybrid polymer inlay was then produced following the previously described imprint protocol and subsequently optically measured. Finally, the inlay was used in the injection moulding process to produce polymer copies of the original silicon master. Parts 1, 10, and 20 were taken from the moulding run to analyse again using the optical profilometer. This meant the polymer replicas could be analysed and compared through the

moulding cycle to check that there was no degradation of the moulding inlay causing a differential in the moulded components.

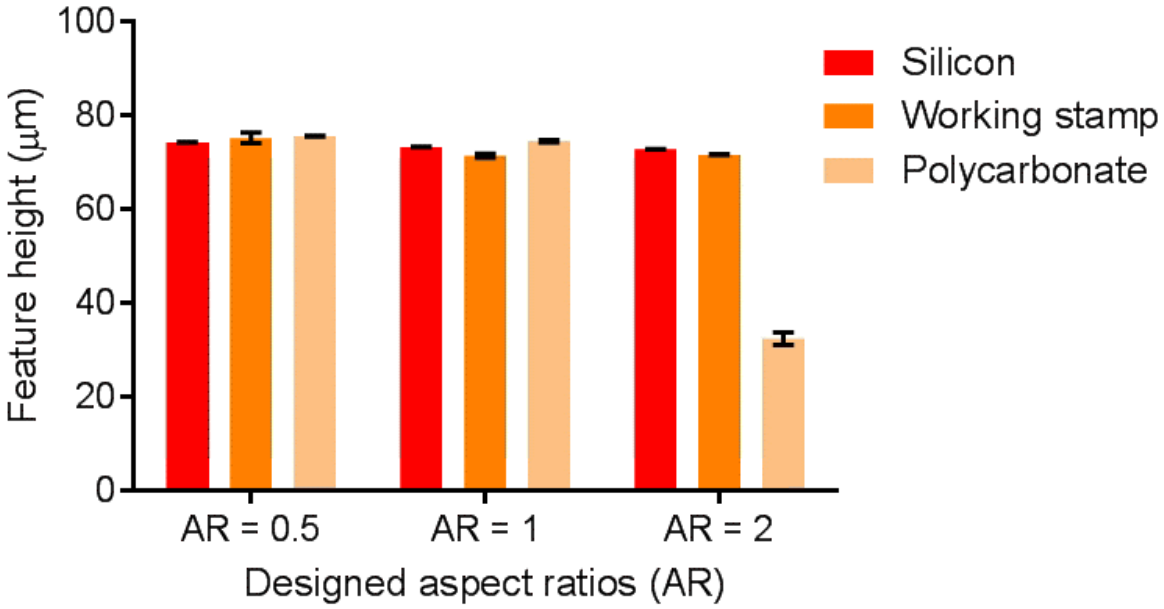

Figure 3.9 - Bar graph representing the results from the aspect ratio study. The results demonstrate the dimensions of the original silicon master, the hybrid inlay, and the polymer replicas (parts 1, 10, 20).

The results from the aspect ratio study are shown in Fig. 3.9, with the full tabulated results given in Table 5. The polycarbonate column in Fig. 3.9 represents the average replication results across Parts 1, 10, and 20 from the injection moulding cycle. The height measurements shown are taken from optical profilometer scans. These scans were taken at five key locations across each AR design for the silicon master, the hybrid inlay, and polymer replica. Each optical measurement was taken using the 5x objective lens and gives a scan measuring 1.8mm x 1.3mm. This allows for multiple measurements of the critical dimensions to be gathered for the replication analysis.

Table 3.1 – Results from the aspect ratio characterisation. Results show mean measured heights at all stages of the fabrication process along with standard deviation.

Measured height (μm)			
Measurement	AR = 0.5	AR = 1	AR = 2
Silicon master	74.3	73.3	72.8
Imprint hybrid inlay	75.2	71.4	71.6
Part 1	75.5	74.4	32.4
Part 10	76.7	74.7	32.5
Part 20	75.2	74.1	30.9
Polymer replica average	75.8	74.4	31.9

The replication across the fabrication process is successful for the aspect ratio designs of 0.5 and 1. This is demonstrated by the extremely similar heights shown by the data in Fig. 3.9 and Table 3.5. There is minimal variation across the heights from the silicon master all the way through to the polymer replicas. This demonstrates a successful replication and production of good quality replicas. There is slight elongation of the features present in the polymer replicas produced via injection moulding. It is hypothesised that this occurs due to a slight stretching of the polymer in the moulding cavity. When the polymer is injected into the moulding cavity, it requires adequate cooling time to hold the required shape defined by the inlay and mould cavity. However, if the polymer is not completely cooled there is an increased risk for microfeature deformation. The injected polymer will typically experience anisotropic cooling, the polymer on the surface will cool or 'freeze' on contact with the cavity while the internal material of the component will take slightly longer to cool. Increased friction on top of the friction results in the feature tops sticking to the base of the microfeature cavity as it is ejected while the rest of the part material has slight mobility, leading to a slight stretch in the profile of the moulded part. Fig. 3.10 illustrates this process. This has been shown in multiple cases by previous polymer injection moulding studies on both a micro and nanoscale [89, 93, 123-125]. If this effect was particularly detrimental to the performance of the desired component and if the dimensions need to be extremely

precise, then anti-stick coatings on the injection moulding inlay such as fluorosilane deposition can be used to negate the effect of feature stretching.

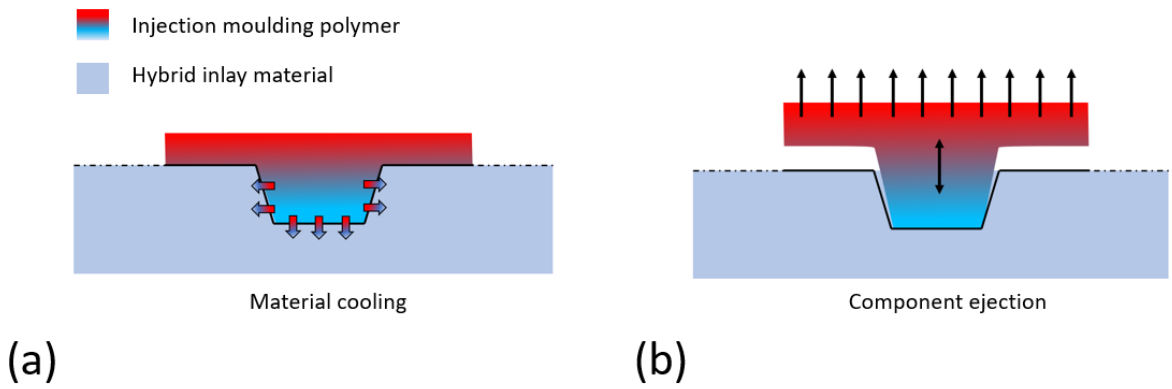

Figure 3.10 – Anisotropic cooling of injected polymer resulting in feature stretching: (a) The material cools anisotropically causing the feature tops to cool faster than the bulk material and feature centre. The tops are below the glass transition temperature, Tg, while the other material remains above Tg and (b) The component is ejected from the mould causing a stretch in the material as the frozen polymer is gripped by a frictional traction.

The results indicate that the replication into the injection moulding stage for an aspect ratio of 2 was not successful. Here the measured heights from the hybrid inlay to the injection moulding stage suggest that there is impartial filling of the mould cavity, resulting in feature heights that are only 55% of the original silicon master. The silicon master and imprinted inlay compare well from the optical measurements; this suggests the problem is in the final moulding stage. It is hypothesised that the polymer freezes prematurely before being fully able to fill the slenderer moulding cavity of the high aspect ratio microfeature. Typically, the way to solve this problem would be to increase the tooling temperature along with increasing the injection velocity and pressure. However, the hybrid polymer inlay is more fragile than the widely used metallic tooling, such as an inlay made from Nickel via electroplating. Therefore, it was thought to be unwise to pursue this route as it would highly likely just damage the imprinted inlays still resulting in poor replication quality. Unfortunately, the AR = 4 designs were not successfully produced in the silicon masters. The mixed etch process used to produce silicon master microfeatures was designed to be used for shallower features. The sloped edge of the designed etch results in extremely fragile features when their width is reduced, and the aspect ratio is increased.

The results suggest that the replication using this fabrication process should be limited to features of AR equal to 1 or lower. It would probably be possible to achieve higher aspect ratio polymer components using the fabrication route, but it would require more extensive optimisation into the already large number of variables controlling the various stages of the manufacturing process.

3.5.2 Feature spacing characterisation

The second design study that was explored was the feature spacing of the microchannels in the silicon master designs and how these could be translated through the fabrication process. The study was developed to investigate how closely the microfeatures could be positioned together, and by extension, if closely positioned features can be translated through the fabrication process to produce polymer replicas. This is a crucial capability in processes designed for MEMS device production. If microfeatures can be produced in high fidelity and in close proximity, then this can reduce device size, and by extension, production costs for components and engineering solutions. The close positioning of microfeatures can also aid in producing more complex solutions in tight spacing confinements.

A new photomask was designed for this characterisation study. This time the mask was designed with 20μm wide features spaced at reducing intervals of 20, 40, 60, and 80 μm. Fig. 3.11 illustrates the designs for clarity. These designs were again produced in areas measuring 10mm x 10mm. The features were designed to be etched to a shallower depth of 25μm to avoid any interference from unwarranted feature depth issues as previously discussed in Section 2.5.1. Optical profilometry was used to examine samples at all stages of the fabrication process, following the same protocol as the aspect ratio study.

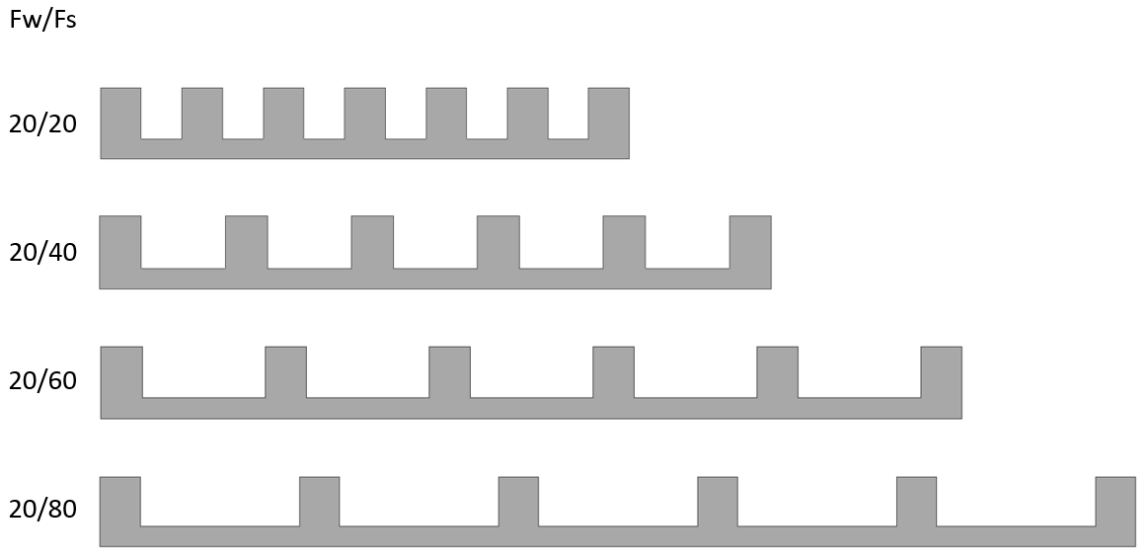

Figure 3.11 – Feature spacing designs. Feature width (Fw) to feature spacing (Fs) ratio shown next to design profiles of the microfeatures.

The results from the feature spacing study are shown in Fig. 3.12, with numerical results shown in Table 6. The data in Fig. 3.12 shows the measured feature spacing taken from the optical scans of the samples at the key stages in the fabrication process. The feature spacing in each case is measured directly from the leading edge of each microfeature to the adjacent feature edge. The data is grouped by the designed feature spacing.

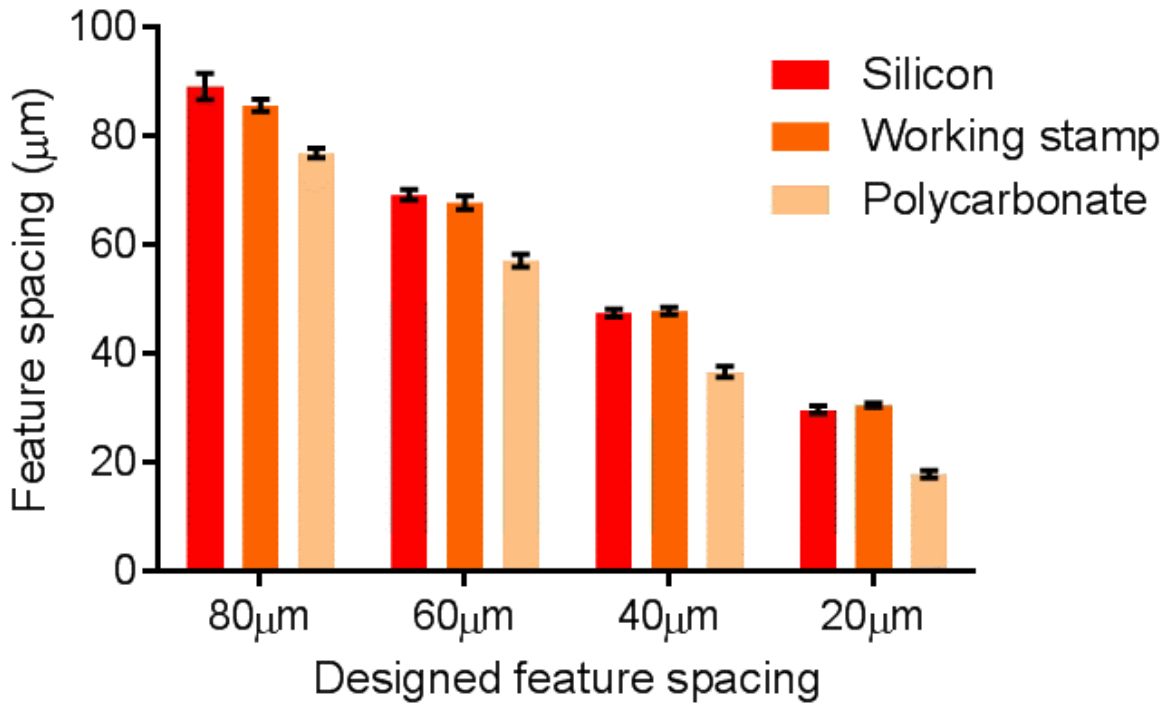

Figure 3.12 - Feature spacing characterisation results. Data grouped by spacing design.

The data shown here indicates that the replication from the silicon master to the polymer replica is of high quality but results in an increase of microfeature width and therefore a slight reduction in the designed feature spacing. This phenomenon is shown across all feature spacing designs. It is believed that this is the result of the hybrid polymer inlay distorting during the moulding cycle resulting in an expansion of the moulded polymer features. Typically, moulding inserts are made from hard wearing materials that can withstand the operating conditions induced during an injection moulding cycle. The hybrid polymer inlay is made from PET sheet and a UV cured working stamp material similar to PDMS. The hybrid inlay materials are durable and can withstand the conditions associated with a moulding cycle, but it is possible to distort or damage the inlays during a moulding run due to the intense pressures and temperatures in the manufacturing process. Here, we see that, when the polymer is injected, it causes the microfeature cavities to expand slightly, leading to an increased microfeature width and reduction in the channel spacing. However, the polymer samples produced are still of high quality and display replicated dimensions well within an acceptable margin of error as seen by the results shown in Table 3.6. Finally, the feature spacing results indicate that tightly spaced features can be replicated on a microscale

in polymer materials via injection moulding. The smallest mean spacing observed was 17.6µm. The results also show no part variation across the components measured for the feature spacing and aspect ratio analysis. This indicates that the fabrication process developed is a prime candidate for users seeking to rapid prototype micro-structured designs with tightly spaced complex features in polymer materials.

Table 3.2 - Results from the feature spacing characterisation. Results show mean measured feature spacing at all stages of the fabrication process along with standard deviation.

Measured height (µm)				
Measurement	Fs = 20µm	Fs = 40 µm	Fs = 60 µm	Fs = 80 µm
Silicon master	29.6	47.4	69.1	89.1
Imprint hybrid inlay	30.5	47.8	67.7	85.6
Part 1	18.5	38.7	57.5	77.6
Part 10	18.1	35.6	58.5	76.6
Part 20	18.2	36.5	56.9	76.1
Polymer replica average	18.3	36.9	57.6	76.8

All studies executed to further elucidate the capabilities of the fabrication process were carried out using acetate photomasks. These were chosen due to their rapid production time and reduced cost. The option to use quartz masters was not an option due to time constraints and because many designs were required across the investigation to fully analyse the process. It is hypothesised that if quartz photomasks were used, then feature fidelity could be increased. This would yield an increase in the minimum feature spacing that could be replicated into the polymer prototypes using the method portrayed here. Quartz photomasks provide increased dimensional control, design production quality, and reduced diffraction of the light used in the photolithography process. All of which could improve the quality of the fabrication capabilities by improving the quality of the silicon masters produced.

3.5.3 Durability test – Mixed dry etch

Durability tests for injection moulding inlays are normally undertaken to ensure that part quality does not deteriorate over the course of an injection moulding cycle. Durability tests are typically used to gauge whether an injection moulding inlay is suitable for larger production runs. If 100+ samples can be achieved with little or no degradation in quality, then it is reasonable to assume that the process is durable. Typically, in industry a moulding inlay would be expected to produce thousands of samples as the process of injection moulding is conventionally used for mass production of products. These inlays would be machined from metal alloys and therefore are far more hardwearing than the polymer hybrid inlays considered in this research.

The fabrication process here is aimed at developing inlays capable of rapid prototyping complex micro topographies in polymer materials via injection moulding. The key advantage of the process is that it theoretically could be executed in one single day - while conventional methods of inlay production can take multiple days or even weeks. Rapid prototyping methods typically aim at producing small batches of products. Therefore, the number of samples required from the production run is significantly less. If 50-100 parts of high quality can be achieved, then the process is durable enough to sustain a run of rapid prototyped designs. For the durability test, a simple design of microchannels like those seen in microfluidic designs was fabricated. The mixed etch process was used as this allows for the optimum microfeature profile for part ejection and has already been established in previous design studies as being able to produce small batch runs (20 parts) of high-quality parts. An inlay was produced from the mix etched silicon master and then used to produce polymer replicas in an injection moulding using the same conditions as described in Table 3.1.

Parts were selected and examined at predetermined intervals to analyse the durability of the inlays. The parts were examined in a qualitative manner using SEM images. This allows the user to examine the quality of the produced polymer microchannels and see if any visible degradation has occurred. The dimensional replication has already been established as high quality in the previous studies. Parts 10, 100, and 200 from the moulding run were

selected and then imaged at various locations over the polymer designs. Fig. 3.13 shows SEM images of the same area on components taken from the moulding run.

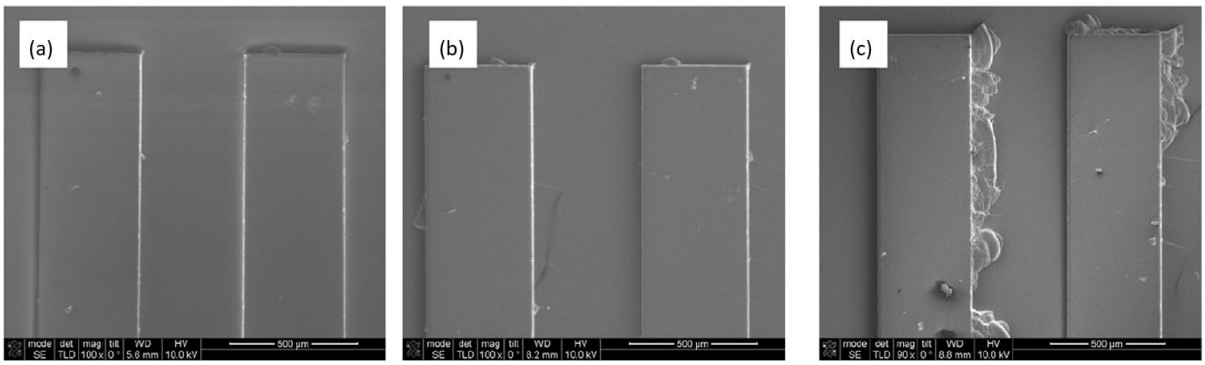

Figure 3.13 – Plan view SEMs of the same area for qualitative analysis of the durability test: (a) Part 10 (b) Part 100 and (c) Part 200.

The images in Fig. 3.13(a) and Fig. 3.13(b) show that 10 and 100 display reliable quality. There are also no changes in the microfeature widths and minimal feature defects were observed in both parts when all SEM images were surveyed. This indicates that the process is completely viable to produce polymer micro-structured components up to at least 100 components. The image in Fig. 3.13(c) shows that there has been inlay degradation by the time Part 200 is encountered. The overall microfeature structure is intact, but the channels have suffered damaged and allowed extra polymer into the mould cavity creating defects in the components. The residual polymer and channel degradation indicate that the fabrication process struggles to create reliable microstructures at this number of components.

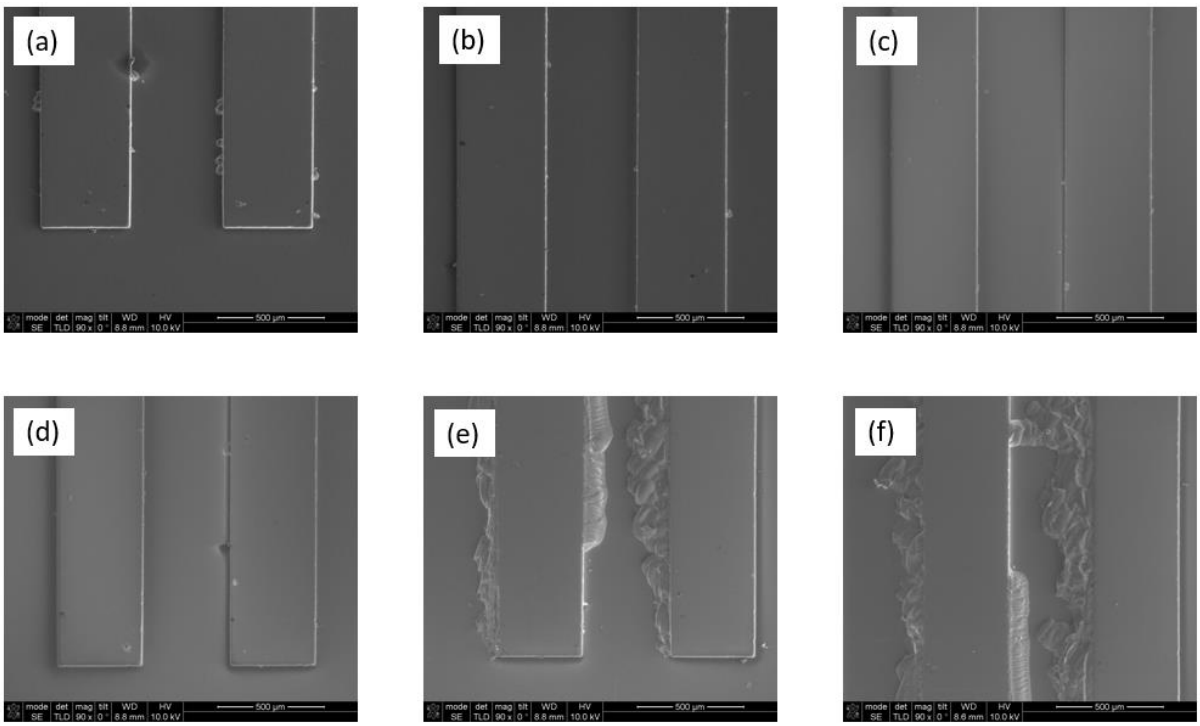

Figure 3.14 - SEM images of Part 200 from the durability test. (a -d) indicate good replication and high part quality. (e) and (f) show inlay degradation.

Part 200 indicates definite degradation of the inlay in select areas of the component. This is shown in Fig. 3.14 (c), Fig. 3.14(e) and (f). However, in general the component was still showing high microfeature fidelity and reliable replication. The images in Fig. 3.14(a)-(d) show high quality features that are concurrent with the quality and replication seen in all areas of Parts 10 and 100 from the durability test. The inlay is therefore only partially damaged in the key areas shown in the previously mentioned SEM images. This would suggest that generally the inlay has been able to withstand the operating conditions of the injection moulding cycle with only small areas of damage occurring. The high quality of the microfeatures in all other areas suggests that, if these areas of damage could be mitigated, then potentially 200+ components could be fabricated using the hybrid inlays. It is hypothesised that if the injection moulding conditions were further optimised for specific designs, then the number of components could be significantly increased. Further optimised moulding parameters for specific designs and the hybrid inlay would mitigate the damage sustained by the inlay and suggest more polymer replicas could be produced. For the current moulding parameters, it is recommended to constrain rapid prototyping runs to

100 components or less as high-quality replicas can be achieved to this number of components.

3.5.4 Bosch etch process replication

As previously discussed, injection moulded components beginning with a dry etched silicon master require a mixed etch profile as this provides the samples with a sloped sidewall enabling separation of the polymer components during the ejection stage of the process. The nano-scalloped sidewall that occurs during the Bosch etch process encourages interlocking of materials during the nanoimprinting and injection moulding stages of the fabrication process. This causes partial replication due to the replica material being damaged as it is unable to fully separate in a low stress manner from the parent cavity. This can also mean that separation can be prevented due to the interlocking nature of the nano-scalloped microfeatures. This process is illustrated in Fig. 3.15.

The successful injection moulding of components using a Bosch etched silicon master is of great advantage to the MEMS community. Bosch etching is a standardised process that requires far less specialist plasma processing expertise than with the bespoke development of mixed etching processes typically used. This would enable users to more easily make use of the fabrication process detailed in this chapter.

It was hypothesised that the low stiffness of the hybrid polymer inlay would allow easier separation from the silicon master and the polymer injection moulded components. The hybrid inlays exhibit much larger flexibility than typical microinjection moulding inserts, allowing the defined microstructures to distort during separation and return to their original shape without causing excessive damage to any components involved in the process. A simple microchannel design was used to test this hypothesis. This was etched using two different Bosch etches, one with fine scalloping, and another with larger scalloping on the etched sidewalls. The characteristics of the scalloping of the etch can be varied by how long each phase in the Bosch etching cycle lasts for, and the power rating of the plasma used on the etching tool.

Samples were moulded using the two different Bosch etch profiles, along with a control that used the mixed etch recipe. The three etch profiles were used to fabricate the same microchannel design. The microchannel designs were all etched to a depth of 35µm. These silicon masters were used to generate hybrid inlays, which were used to injection mould components using the same conditions as the characterisation studies. SEM images were taken of Parts, 1, 10, and 20 to examine the quality of the moulded components.

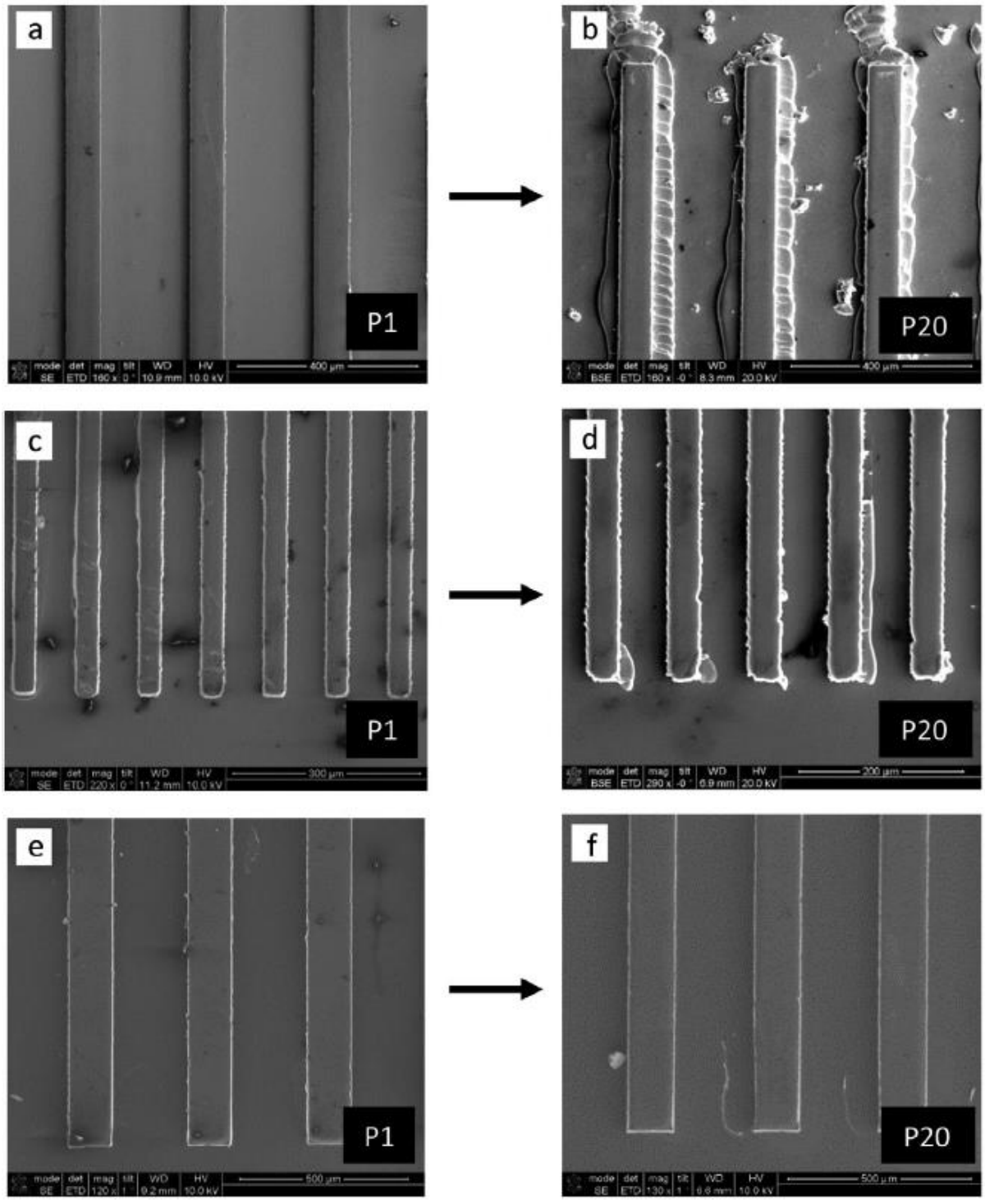

Figure 2.15 – Bosch etching study. SEM images used to investigate the inlay damage and part quality as the moulding cycle progresses. The arrows indicate Part 1 (P1) to Part 20 (P20): (a-b) Indicate the parts moulded from the silicon master with coarse scalloping, (c-d) Indicate the parts moulded from the silicon master with finer scalloping and (e-f) show the control samples that were moulded from the mixed process etch recipe. Magnification used for each image (a) 160x (b) 160x (c) 220x (d) 290x (e) 120x (f) 130x.

The images in Fig. 3.15 show the results from the Bosch etch study. Fig. 3.15(a-d), show that there was increasing damage to the inlay as the moulding cycle progresses. This is to be expected as the scalloped edges will cause the moulded components to grip to the inlay during ejection. However, in both cases, part replication is possible. Highlighting that it is possible to use Bosch etch recipes for microinjection moulding. Optical scans of the original silicon masters and moulded components confirm that the full microfeature depth was replicated. The images in Fig. 3.15(a-b) show the coarser scalloping and a faster rate of damage to the inlay, indicated by the poor replication quality of Part 20. The results from the finer scalloping are more encouraging. Significantly lower degradation to the inlay is observed in Part 20, shown in Fig. 3.15(d). This suggests that there is more scope for the development of the use of Bosch etching methods along with the fabrication method developed here. If Bosch etch profiles were to be used in the future, then a finer scalloped edge should be encouraged to minimise the damage to the hybrid inlay. These results are encouraging as it broadens the scope of where the fabrication tool can be utilised. Components were ejected from the hybrid inserts successfully without great difficulty. Cross-sectional SEM mages were taken of some components to observe if the nano-scale scalloping translated through to the moulded polymer components.

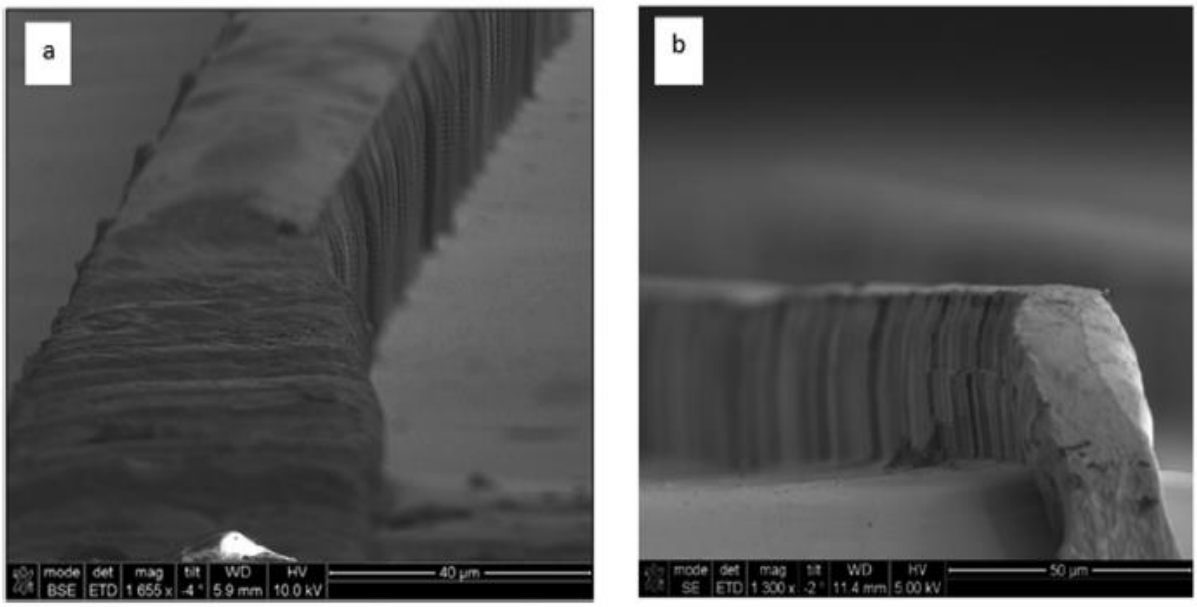

Figure 3.16 – Cross-sectional SEM images of Part 10 from the moulding cycles to observe the etched scalloping: (a) Fine scalloping. (b) Coarse scalloping.

The images shown in Fig. 3.16 indicate that nano-scalloping inherent to the Bosch etches has translated through to the moulded components. Both the fine and coarse scalloped etches successfully exhibit the etched sidewall from the original silicon masters. This indicates high quality part replication as well as further evidence of successful part ejection. If the scalloping was absent in the moulded components, then it would be reasonable to assume that the polymer components were either damaged during ejection or incomplete filling of the mould cavity was occurring.

Even though it is possible to successfully mould from the silicon masters, the process is still far less efficient than moulding using a mixed etch silicon master. The work here has highlighted the feasibility of the process, but this must be further developed and optimised. Part quality and prototype numbers of designs must be increased for the process to be fully viable. Realistically, a full optimisation study must be done into the required moulding parameters that would best suit a Bosch etch master. A study into what size of scalloping on the microfeature walls best suits the process developed here would also be useful.

3.5.5 Proof of concept – Microfluidic device

A final study was executed to illustrate the potential research applications of the fabrication process. A microfluidic device was developed and then produced using the process. This aimed to show that the fabrication process can be used to manufacture complex MEMS designs. The mixed etch process was used during this study as it yields the best results when used with the fabrication process. The microfluidic design and a SEM of the moulded polymer device are shown in Fig. 3.17. The moulded channels were of high quality and correspond well to the original design. The original CAD design in the serpentine section has channel widths of 100µm, with the corresponding polymer devices channel widths measuring 90.5µm ± 0.7. The etch depth of the design was 9.44µm. This shows that good feature translation through the process can be achieved even in the case of complex designs.

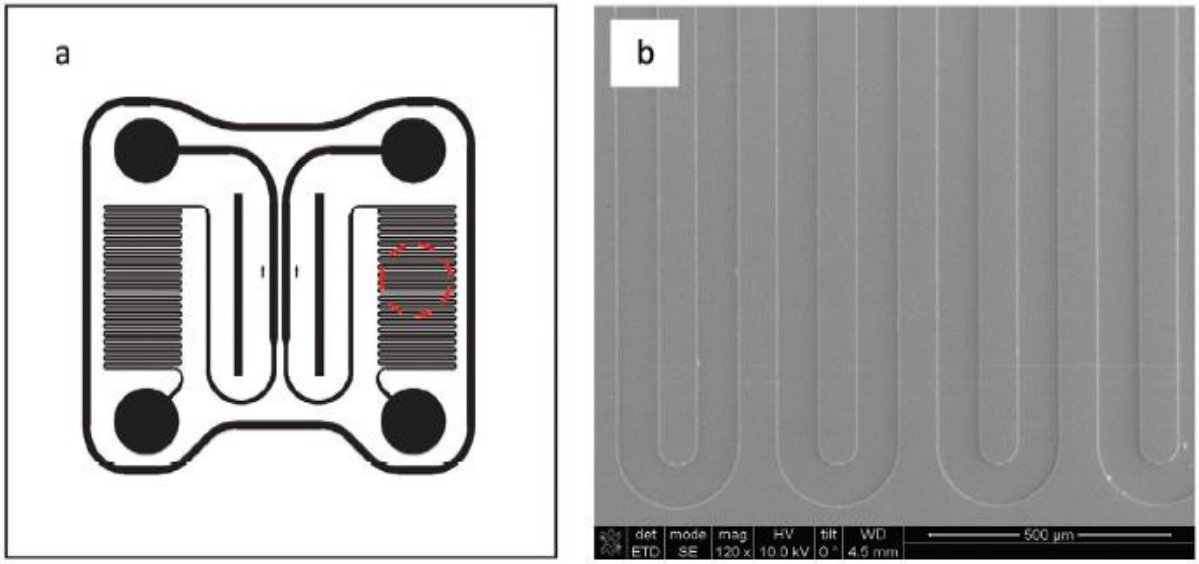

Figure 3.17 – (a) Microfluidic design and (b) SEM image of the serpentine channels of the moulded polymer device. The red circle in (a) corresponds to the channel region shown in (b).

3.6 Conclusion

This chapter has presented a novel microfabrication technique where silicon etched masters are used in a nanoimprint lithography (NIL) process to produce flexible inlays for injection moulding. Initial microfeatures and patterns were produced through both modified and conventional dry etching techniques. The initial research used a fully optimised process to mould complex microstructures, created through a mixed silicon etching process. These initial designs were used to formulate design studies where the capabilities of the developed process could be explored, aspect ratio and feature spacing of the microstructures were investigated. It was found that an AR of 1 and below can be effectively replicated in polymer microstructures. It is theoretically possible to generate microfeatures of higher AR. However, this would require further optimisation of the process specific to the higher aspect ratio micro-structured designs. The feature spacing study highlighted that the process is highly adept at producing tightly spaced microstructures, the study shows that high quality features spaced as tightly as 20 µm can be produced.

A study was then performed to explore the fabrication capabilities of replicating and successfully injection moulding microfeatures generated from a Bosch etched silicon master. This is difficult due to the scalloped sidewalls presented in the features produced using this etching process, causing mechanical interlocking of features during the moulding process.

However, the work here shows this can be successfully performed using the fabrication process developed in this chapter. It is hypothesised that the flexible nature of the injection moulding inlays plays a crucial part in enabling the successful ejection of Bosch etched microfeatures. Finally, a durability study was performed to confirm the viability of the fabrication process to be used in the rapid prototyping of complex microstructured devices. This study confirmed that ≈100 devices can be produced successfully from a mixed process etched silicon master without any significant part deterioration. A proof-of-concept microfluidic device was also manufactured to highlight the potential applications of this fabrication process.

The work here has developed a novel microfabrication technique to produce flexible inserts for injection moulding. This enables high quality complex microstructured devices to be manufactured in a relatively short time frame. From start to finish the process can be completed in one working day, from silicon etch to final polymer moulded component. The studies in this chapter highlight the ability of the process to be tailored to novel production types, such as mixed process and Bosch etching. The process is ultimately suited for rapid prototyping complex devices, that can then be tested and modified to suit the specific engineering purpose, such as the microfluidic proof-of-concept. The process also displays cost effective attributes when compared to the industrial moulding processes such as LIGA inlay production. Following initial equipment investment, the process could be implemented easily in an industrial environment to explore the viability and performance of microstructured designs.

Chapter 4.

Repeatable and Tailored Normal Contact Stiffness

4.1 Introduction

This chapter explores the viability of developing micro-structured polymer interfaces that exhibit repeatable and tailorable contact stiffness. Normal contact stiffness plays a large role in the mechanical behaviour of an interface. The stiffness of an interface is the inverse of the compliance of the surfaces in contact. Normal contact stiffness and can be mathematically defined as the rate of change of normal load, *P*, with the relative approach, *d*, of two surfaces in contact ($K_n = |\mathrm{d}P/\mathrm{d}d|$). Typically, the stiffness of an interface is thought of as the deformation of the rough surface topographies in contact. However, depending on where contact stiffness is measured from, a measurement can include some degree of contribution from the bulk material. As discussed in Chapter 2, the measurement of normal contact stiffness will be considered at a mean distance from the interface to allow for simpler empirical measurement.

The contact stiffness of an interface can have a great influence on mechanical design of engineering systems. The contact interfaces across a mechanical system introduce areas of compliance that can influence damping and mechanical behaviour on a micro and macroscale. Contact stiffness of mechanical interfaces is important to consider in a wide range of areas such as: bone-implant interface design [126], the vibration behaviour and response of mechanical joints [127-129], thermal and electrical resistance of interfaces [25, 130, 131], robotic gripper system behaviour and efficiency [132], and even the performance of precision machinery [133]. These systems all indicate the influence that contact stiffness can have. However, all these examples concern engineering surfaces where the surfaces in contact are randomly rough and unpredictable. This makes their tribological properties (such as contact stiffness) difficult to easily predict without the aid of complex mathematical

modelling and numerical schemes that model the behaviour of rough surfaces. This can slightly restrict interface design to experts in the field, as engineers without tribological knowledge may be unaware of the numerical tools and skills to appropriately produce interfaces that exhibit the properties required.

Predicting the contact stiffness of rough engineering surfaces imparts its own challenge due to the complexity of the asperity interactions of an interface. Numerical models exist, as previously discussed, but these are time-consuming, complex, and difficult to integrate into engineering system simulations. Repeatability of contact stiffness in engineering interfaces presents another hurdle. If a joint exhibiting a set of mechanical properties is taken apart and reassembled, then it is likely to display a different mechanical response and contact stiffness due to the new contact interactions of the surface asperities on a micro and nanoscale. This issue is widespread and problematic when designing for repeatable and reliable engineering solutions. An example of this would be in turbine blade housings or aeroengine vibrations. Accurate FE models can be generated to simulate the bulk material behaviour of these critical components, but interface properties and interactions are far less accurately modelled and this gives rise to errors in the vibration modelling of large multicomponent systems. The key interface parameters such as contact stiffness often need to be measured empirically rather than simulated [134]. Essentially, the random multiscale nature of a randomly rough surface makes difficult to produce interfaces with predefined characteristics for engineering design unless the engineer or designer has keen skills in the fields of tribology and contact mechanics.

A route to repeatable and tailored normal contact stiffness could allow an interface to be designed for a specific engineering solution. The manufacture of microstructured polymer surfaces opens up the possibility of producing deterministic interfacial properties such as contact stiffness. Related aspects of microstructured interfaces have been explored recently by colleagues: the frictional properties of structured interfaces were investigated by Bin Jaber et al [135], and their behaviour in adhesive joints by Hamilton et al [136]. The most relevant study to the work in this chapter is that of Li et al [42]. This work investigated the contact stiffness of a rigid patterned surface of cylindrical micropillars being compressed

into a flat deformable surface. Here the authors employed elastic flat-punch theory to investigate the pillar's interaction and their influence on contact stiffness. The study highlighted how contact stiffness is dependent on micropillar or feature spacing, and the number of contacting features, or real contact area.

The work here begins by exploring the viability of achieving repeatable and tailorable normal contact stiffness measurements via mechanical testing of the microstructured polymer interfaces. These results are compared and validated using FE models designed to simulate the mechanical tests. An array of microstructured polymer interfaces were designed and produced to investigate how normal contact stiffness could be tailored based on the designed dimensions of an interface. All microstructured interfaces were produced using the fabrication methodology outlined in Chapter 3.

4.2 Experiment methodology

An adequate testing methodology had to be developed before the contact stiffness of the microstructured interfaces could be explored. This required the development of a bespoke mechanical testing rig, and investigation into the most appropriate method for measuring normal contact stiffness during the experiments. This section outlines the experiment design and techniques used for the measurement of normal contact stiffness throughout all investigations. The experimental equipment can be divided into two sections: the mechanical testing rig, and the optical measuring system. These two systems facilitated the measurement of both applied normal force and relative displacement of the interfaces which were used to obtain normal contact stiffness measurements during the experiments.

4.2.1 Mechanical testing rig

An existing micromechanical testing machine (5 kN Dual leadscrew, Deben, UK) was adapted for the normal contact stiffness measurement tests. The Deben micromechanical test machine was selected as it offers good control over both load and displacement driven tests. The force sensitivity of the microtest rig is based on the load cell that is installed during the test. The displacement control is where the Deben really excels, as this can be

controlled on a micron scale. This is particularly useful when considering contact mechanics tests.

The Deben was modified to allow it to apply a normal load to the interfaces with the force being measured via the machine's in-built load cell. Custom designed fixtures that allow for self-alignment of the samples were integrated into the original test rig. The self-alignment fixtures were designed to ensure maximum and uniform contact of the microstructured interfaces during the tests. This self-alignment feature was also added to prevent the interface making a point or edge type contact. This would risk incomplete contact and exaggerated plastic deformation due to inconsistent load distribution across the interface.

The modified microtest rig is shown in Fig. 4.1. The photograph shows the microtest rig with the custom experimental fixtures inserted. The red box indicates the modified area with the test samples included. The schematic inside the red dashed line illustrates the fixtures designed to facilitate the self-alignment contact of the polymer samples. The original fixtures were made from stainless steel and machine milled. However, as extremely minor changes were required, it was decided to 3D print the new fixtures and use these in all the subsequent normal contact stiffness tests. All basic design elements of the fixtures remain consistent throughout testing.

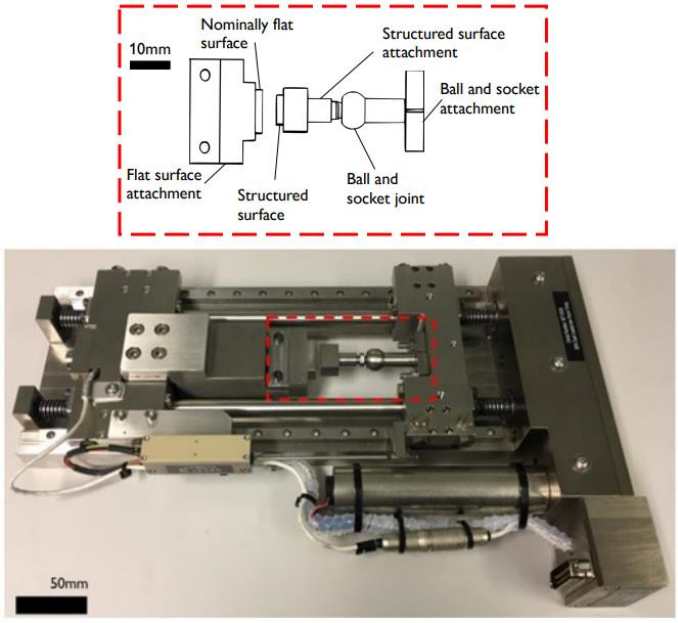

Figure 4.1 - Experimental test rig for normal contact stiffness experimentation. Micromechanical test rig with custom designed self-aligning fixtures (red outline box).

The nominally flat and microstructured samples were glued to fixtures as shown in Fig. 4.1. The microstructured sample is glued to the fixture attached to the ball and socket joint that allows for self-alignment during the tests. The fixtures were designed so that the central (perpendicular) axis of the samples is in line with the load cell's line of action measuring force in the micromechanical test rig. This helps to reduce error when the applied normal force is measured during the mechanical tests. All the tests were completed with ambient conditions of temperature, pressure, and humidity. The samples were cleaned using IPA and compressed air before mechanical testing.

4.2.2 Displacement measurement using digital image correlation

The approach and compression of the samples had to be tracked to allow *local* measurements of the relative displacement of the interface to be made during the mechanical tests. Digital image correlation (DIC) was selected to make the measurements of the relative displacements required for normal contact stiffness calculations. DIC is a point-by-point experimental method that can be used for stress analysis by tracking the displacement or deformation of the material area in question. The surface or material section is analysed by tracking movements of patterns applied to the critical measurement area. This makes the measurement versatile as it can be applied to a wide range of settings and scales. Typically, the results can be compared to strain gauge measurements to verify the results. However, the microstructured sample tests required a non-contact measurement method to track the displacements and therefore only DIC was considered.

DIC requires 2D or 3D imaging systems, depending on the situation and measurements required. No contact is made with the experimental samples during mechanical tests. An applied pattern or textured material surface is required for the camera system to map and track the deformations of the measurement area. The pattern distorts as the material area deforms, allowing the displacements of the material to be tracked by the DIC system. The first practical DIC systems that were applied to engineering problems were developed in the 1980s. With Sutton et al. [137] being one of the pioneers of DIC system application for engineering solutions. Digital images are taken during the loading events of a mechanical test, measuring the displacements as the normal loading is applied to the microstructured

interfaces. Good levels of light are required to allow the camera to track the samples during the tests. The optical microscope can be used to ensure that the surfaces are properly aligned. The relatively low range of depth of focus on the microscope lens system means that the sample edges must be properly aligned to be in focus for the DIC. Once the surfaces have been brought into contact the alignment can be checked by eye at the rig and then a closer inspection can be made using the optical microscope to ensure the samples are in focus and aligned in contact properly before the loading of the test can begin.

The basic concept of DIC systems is relatively simple. A pattern or surface texture is applied or generated on the material area. This is used to track the deformations. The camera system is positioned to allow images to be collected during the mechanical tests. In this case the microscope system was positioned above the modified microtest rig to track the displacements during the application of normal loads. The camera is calibrated accordingly to ensure accurate measurement of the displacements. Fig. 4.2 shows a simplified diagram illustrating the basic concept of the mechanical tests, and how the relative displacements of the interface were tracked. The relative displacement of the interfacial separation is the change in d^* shown in Fig. 4.2. This definition of d* is more practical than measuring the classical d, which accounts for the interface alone. The introduction of this new parameter is necessary as DIC must measure the interfacial separation but at a distance away from the interfaces topography to allow the DIC to focus and collect accurate measurements. This means that d* will include bulk material effects, which increases as the measurement area moves further from the interface. In this work the distance of d* was set to 200 μm at the test start point as this included the full microstructured interface and allowed for a clear measurement point but also aimed to minimise the bulk material inclusion in the measurements.

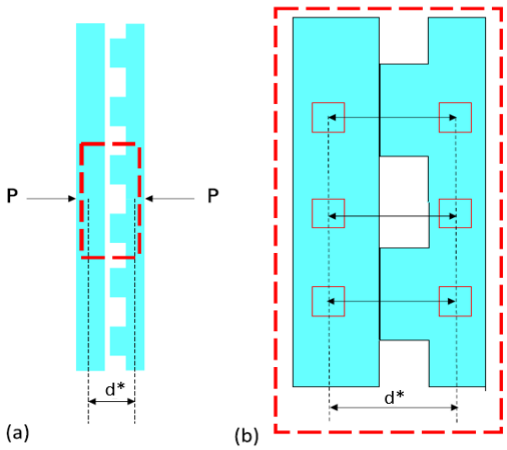

Figure 4.2 – Simplified schematic illustrating the mechanical testing: (a) Shows the application of the normal load, P, and then the relative mean interfacial separation, d*, being measured and (b) illustrates a zoomed-in region (denoted by the red box) to show how the DIC system tracks the relative approach of the samples. Five target pairs were used with only three shown here.

The tests work by applying an initial pre-load of 5 N for alignment of the surfaces. The contact of the interface is then loaded up to a value of 1500 N at a rate of 0.5 mm/min. This slow loading rate was used to ensure a quasistatic test. As previously mentioned, the loading is measured by the load cell in the Deben microtest rig. The relative normal interface displacement is then tracked by the DIC system positioned above the experiment. The tracking of the displacements is facilitated locally at the interface by positioning the DIC tracking targets close to the contact interface of the samples. These were separated by approximately d^* = 200 µm. Five targets were used along the interface in pairs as shown in Fig. 4.2.

The images were captured using a digital camera (PL-D732 2.2MP, Pixelink) and a high magnification adjustable lens system (Zoom 6000, Navitar, USA). The lens system was used as it allows for a large depth of field, making sure the samples remain in focus during the tests; thereby, increasing the accuracy of the DIC measurements. The field of view provided by the camera setup was 6.3 x 4.7 mm with 680 x 480 pixels providing an image resolution of 9.8 µm. The lens and zoom system settings allow for sufficient detail in the measurements. Imetrum Video Gauge DIC software was used for the measurements. The software quotes that it can track 1/200th of a pixel; therefore, the smallest resolvable displacement should be roughly 0.05 µm. The sampling rate was set at 0.5 s, this was the

same for both the microtest rig and the image capturing systems. This provided easy integration and synchronisation of the measurements from the separate systems.

4.2.3 FE model design

Finite element models were developed to help to verify and better understand the mechanical behaviour of the microstructured interfaces during the tests. The FE model was also used as a comparison to ensure that the values being measured were realistic and acceptable. The FE models were designed and built using ABAQUS. The models were first developed for use in the repeatability study and future models were developed for the tailored contact stiffness study. Fig. 4.3 illustrates a schematic of a typical FE model used during the structured normal contact stiffness studies.

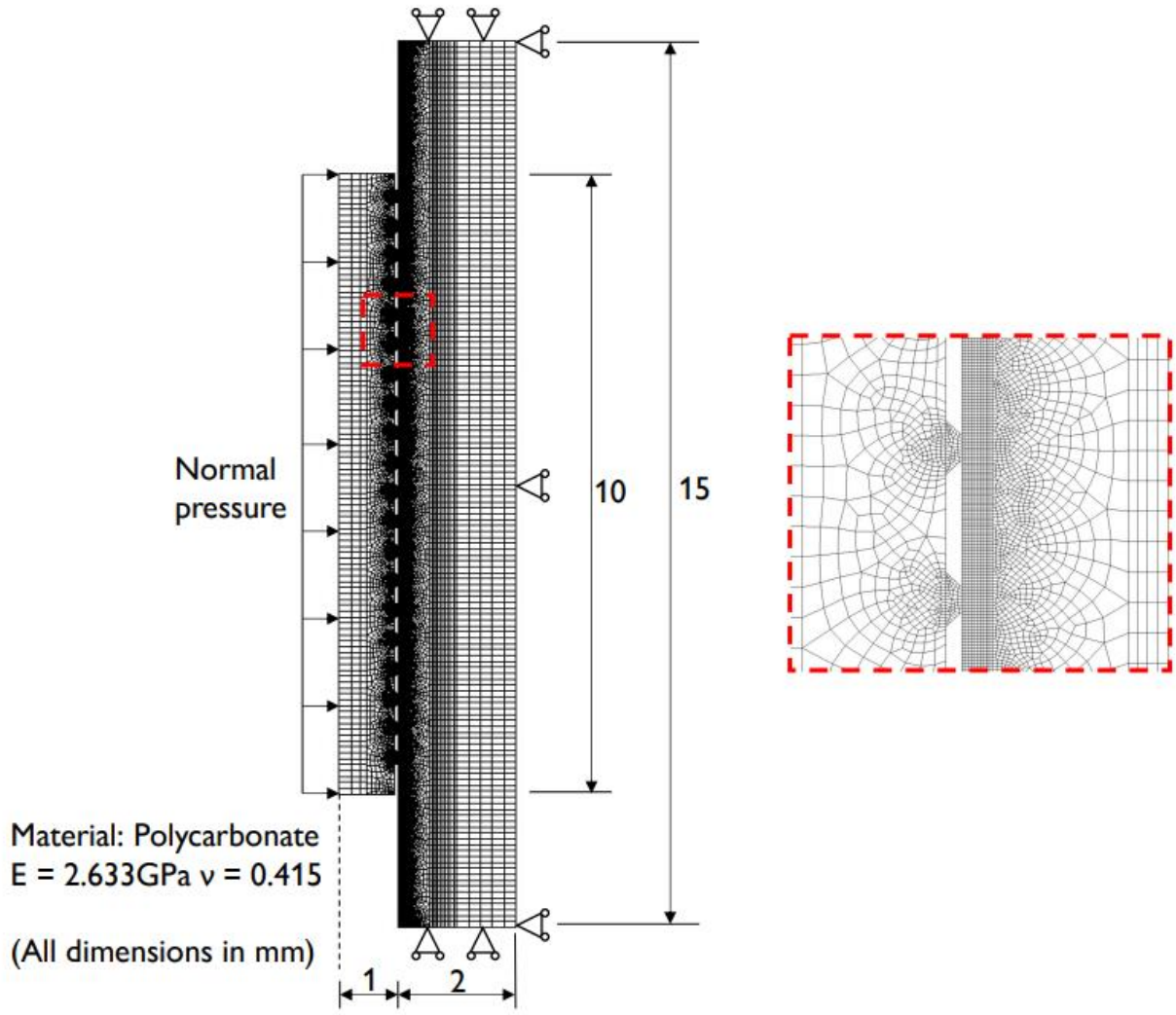

Figure 4.3 – Finite element model for calculating normal contact stiffness behaviour of the microstructured interfaces.

The models developed were linear elastic 2D plane strain in nature. The decision was made to keep the models as 2D as this would reduce computational time and allow for simple tailoring of the models for comparison with the mechanical tests. The topographies of the structured interfaces were used to design the FE models. The optical profilometry scans and SEM images guided the dimensions and design when building the models to ensure that the contact interface was sufficiently comparable. The red dotted line in Fig. 4.3 indicates the microfeatures at the contact interface that are designed based on physical measurements of the tested interfaces. The mesh used in the models was designed to have increased density at the interface and critical areas, with the mesh density reducing away from the interface in a structured and controlled manner. The mesh was designed to fit accordingly with the design parameters of the model so as to avoid element distortion. Mesh sensitivity studies were conducted on all models to ensure accurate results. The structured surfaces in the models were constrained to be fixed in the y direction and could move in the x direction to allow them to compress against the idealised flat surface. The idealised flat surfaces were fully constrained using ENCASTRE boundary conditions. The surface contacts were constrained using master-slave surface frictional contacts. The element numbers in the mesh increased as the microfeature size and percentage real contact increased. The 16%, 34%, 55%, and 77% models contained 36965, 41429, 50880, and 56298 elements respectively.

All global sizes of the surfaces used in the models were measured from the test samples. The material properties used in the model were measured from polycarbonate samples produced using the same injection moulding parameters used to produce the microstructured samples. The properties were measured from simple tensile tests of the polycarbonate samples. The tensile tests were carried out using the unmodified Deben microtester. All boundary conditions implemented in the model were representative of the conditions used during the mechanical testing of the structured interfaces. For calculation of the FE contact stiffness, nodal pairs on either side of the interface were tracked. These nodes are positioned apart by a distance $d^* = 200$ μm. This the same distance that separates the tracking targets used in the DIC to measure the rate of change of relative displacement

of the interface. The results from the FE models are discussed and compared to the experimental results in the repeatability and tailored normal contact stiffness studies.

4.3 Repeatable normal contact stiffness

Firstly, it had to be established if the microstructured polymer samples could exhibit repeatable normal contact stiffness. The initial tests that were conducted aimed to achieve repeatable measurements from multiple tests of samples that were produced from the same moulding run and exhibited the same microstructures. These samples were designed to have relatively large microfeatures, before tailoring of the structures and normal contact stiffness could be explored. The samples were produced in the thermoplastic polymer, polycarbonate.

4.3.1 Repeatable sample topography design

Repeatable microstructured topographies were produced using the fabrication method detailed in Chapter 3. The samples were taken from the same injection moulding run, using the same hybrid inlay. The topographies were examined using optical profilometer measurements and SEM imaging techniques. The designs consisted of 450µm channels with spacing of 450µm. The channels run parallel to one another and fit into an area of 10 x 10mm. Fig. 4.4 shows multiple images and scans to illustrate the designs used in the repeatability study.

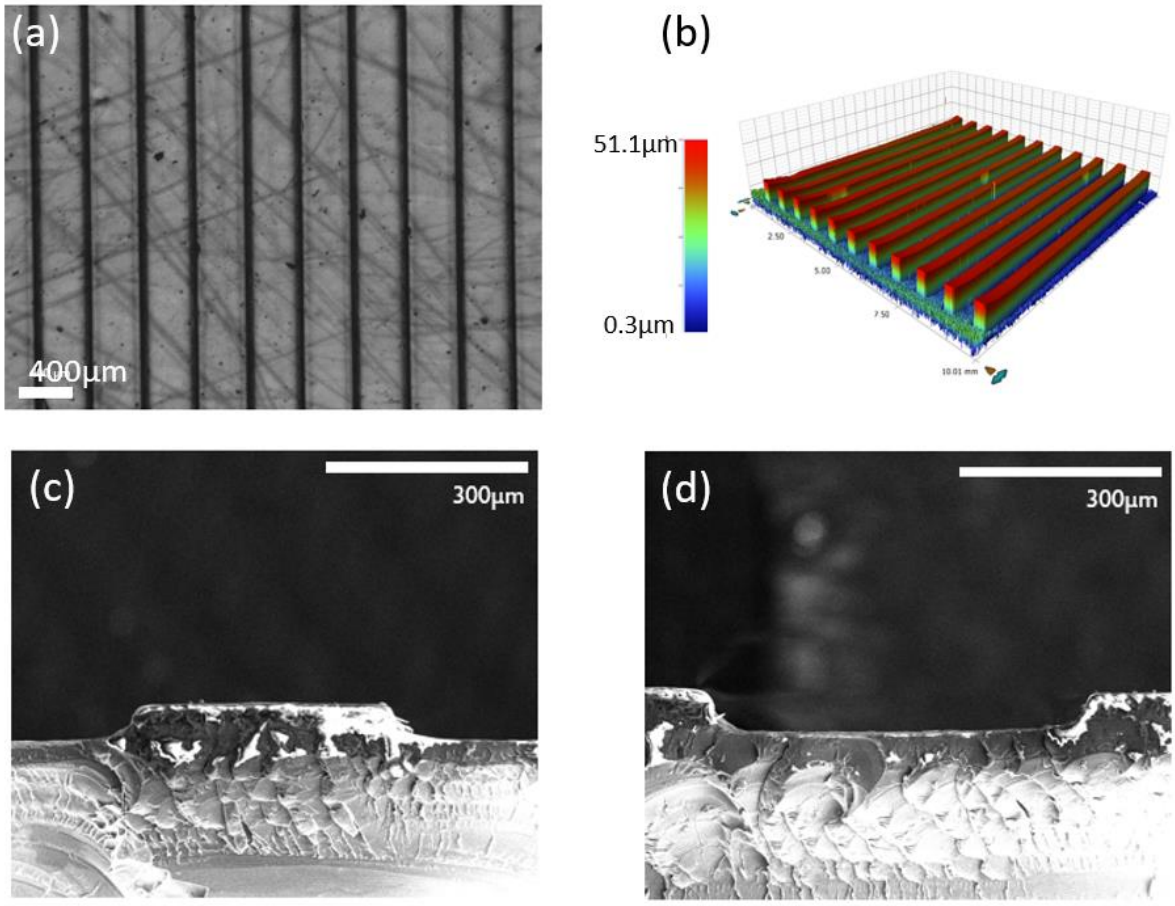

Figure 4.4 – (a) Top-down microscope image of microstructured polymer samples, (b) Stitched optical scan of microstructured polymer samples, (c) SEM image showing cleaved cross-section of a microstructured feature on a polymer sample and (d) SEM image showing cleaved cross-section of the gap between structured features.

The critical measurements considered when measuring the polymer samples were feature height, width, and spacing. Along with the features of the samples, it was important to consider the feature tops. Since this is the region of contact with the nominally flat sample, it is crucial to ensure the roughness on the feature tops was of a negligible magnitude when compared with the feature heights. Any significant roughness would influence the normal contact stiffness measurements by introducing additional compliance to the interface. The feature dimensions were scanned using the 5x optical zoom while the feature top roughness was measured from scans taken using the 50x optical zoom. The measured feature dimensions and corresponding roughness are shown in Table 4.1. The roughness of the feature tops indicated in Table 4.1 shows that the roughness is on the nanoscale and three orders of magnitude less than the feature heights. It is reasonable to assume that the roughness is small enough to make a minimal effect on the contact stiffness of the interface.

Table 4.1 – Critical dimensions measured from the repeatability polymer samples. Measured from samples 10, 30, and 50 from the moulding run.

Feature dimension			
Height (μm)	Width (μm)	Spacing (μm)	Roughness (at top), Sq (nm)
50.04 ± 1.06	401.92 ± 3.17	420.62 ± 3.36	55.3 ± 8.3

4.3.2 Repeatability results and discussion

The mechanical tests in this section aimed to illuminate how repeatable mechanical properties can be achieved through the micro structuring of an interface, specifically in this case for normal contact stiffness. Tests were carried out on five separate samples of the same topography. The five samples underwent the same testing methodologies previously outlined. The samples were brought into contact and loaded under compression to 1500 N in the microtest rig. The relative approach was tracked using the DIC positioned above. The average relative displacement of all the pairs of the DIC targets across the interface is then calculated and then plotted against the force data. A linear regression was applied to the linear portion of the force-displacement curve to elucidate the normal contact stiffness of the interface. An average normal contact stiffness for each sample is then be calculated from the five individual tests for each sample. The results from these tests are shown in Table 4.2.

A typical force vs. displacement graph from an experiment is shown in Fig. 4.5. All graphs for the tests follow extremely similar trends. The graph shows the different stages of the test that occur. The first and largest portion indicates the approach of the samples before contact is made. The middle, non-linear section is when initial contact is made. Load begins to be applied to the interface and the interface transitions from partial contact to all micro-structures making contact with the nominally flat surface. Not all features will instantaneously be in contact as shown. Initially small areas of the microfeature tops will be in contact, but as load increases so does the percentage of the features in contact. Rigid body displacements of the experimental apparatus such as the spherical joint and

leadscrews of the microtester can also potentially introduce non-linearities to the curve as contact is made. Once the whole micro-structured surface is in contact, the true normal contact stiffness can be analysed. The final region shows the linear elastic region of the test. During this section, the micro-structures can be seen to be in complete contact and a linear relationship between the relative displacement of the surfaces and the applied normal load is illustrated. The slope of the linear region in all tests is regarded as the normal contact stiffness of the interface when complete contact of the micro-structure is achieved. An example of the linear regression applied is indicated in the third linear region in Fig. 4.5. This regression analysis was applied to each test above the 500N point. This allows the contact stiffness to be measured when the samples are in full contact.

Table 4.2 – Results from the repeatability normal contact stiffness tests. Comparison to the FE model included.

Sample no.	Normal contact stiffness (kN/mm)
1	70.02 ± 3.09
2	75.12 ± 4.094
3	69.81 ±2.81
4	68.23 ± 4.72
5	71.34 ± 2.32
Average experimental value	70.91 ± 3.92
FE model	90.78

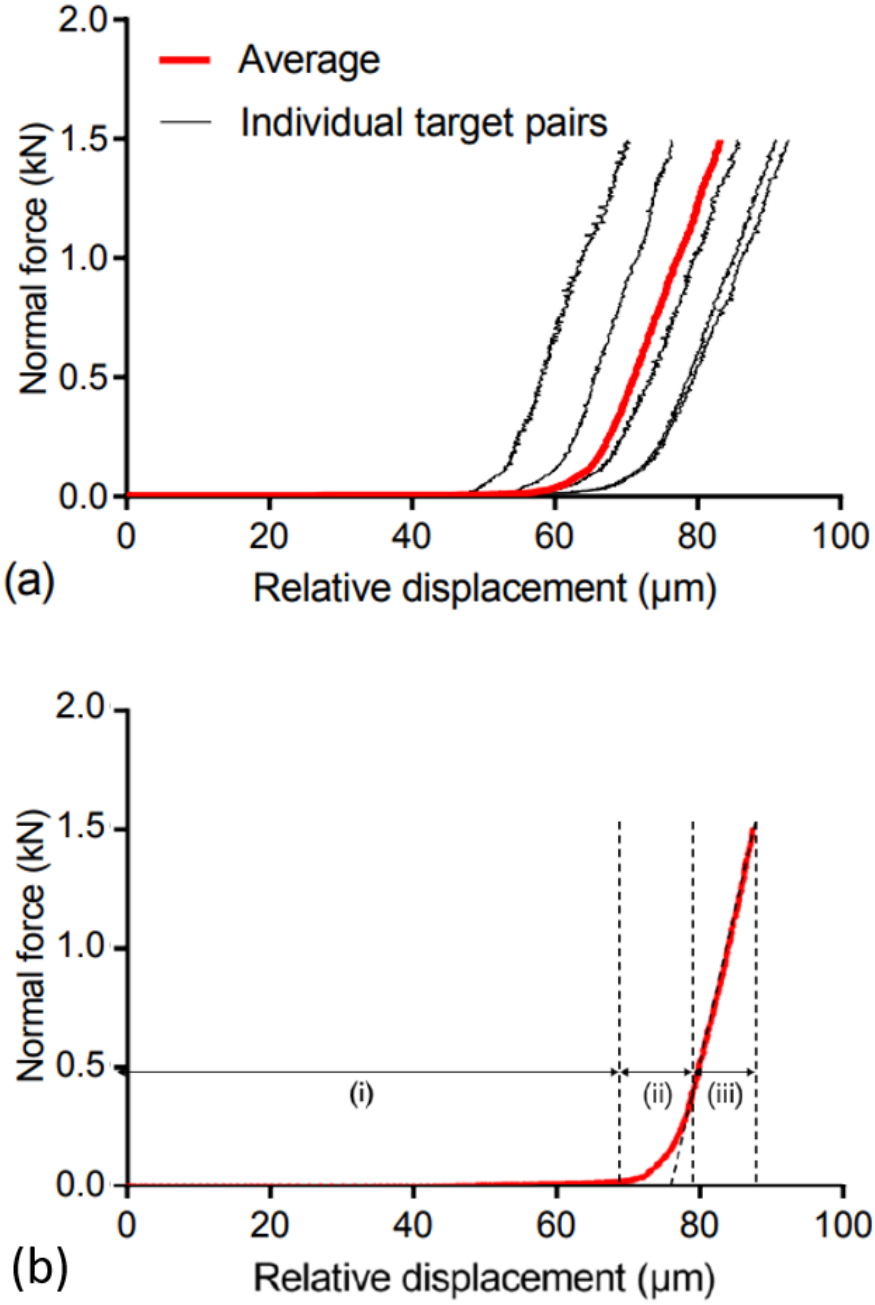

Figure 4.5 – (a) Normal force versus relative normal displacement from a typical test showing the result at each target pair as well as the average trace (contact stiffness at saturation is determined as the slope of the linear region) and (b) The average force-displacement trace from all five tests..

The results shown in Table 4.2 show the measured values from each sample after 5 repeat tests. The measured values of normal contact stiffness indicate high repeatability of the microstructured interfaces tested. The relatively low standard deviation of 3.92 over all tests (compared to a mean of 70.91 kN/mm) indicates a low spread of measurements for normal contact stiffness. Therefore, these results indicate that high repeatability of the normal contact stiffness of an interface can be achieved through the micro-structuring of

topographies. The differences between the measured values of contact stiffness can arise from two main sources: both the experimental set up and manufacturing of the interfaces.

Even though the interfaces are assumed to have the same topography, there will still be slight changes to the topography introduced through the injection moulding process. It is nearly impossible to ensure every sample will be identical. It has been shown that they are highly similar as they are produced from the same mould, using the same moulding parameters etc. The optical measurements also indicate low variability in topography. However, there will inherently be differences between the topographies. This can be in the form of differences in the roughness of the features and thus areas of contact. Defects can also be introduced during moulding, and from the handling and preparation of samples during mechanical tests. Defects introduce variability in true contact area, and thus in the measured normal contact stiffness.

The results from the tests compare well with the results from the FE model, shown in Table 4.2. This was promising as it indicates the FE model can simulate the mechanical behaviour exhibited by the interfaces during the experiments. This was the initial study to discover if the linear elastic 2D plane strain model would be sufficient for the planned tailored contact stiffness studies. For the repeatability study, the FE model overestimates the normal contact stiffness of the interface. This is to be expected as the FE model will simulate idealised smooth surfaces without roughness. In the FE simulation, there is full and complete contact as soon as a load is applied. The interface modelled is also completely uniform in design and devoid of any defects. Therefore, it is to be expected that the in-situ samples will have extra compliance introduced from the large number of variables inherent in the testing of real samples.

Even slight changes to the mechanical testing conditions can introduce changes to the measured values. Much of the variability here can be attributed to slight variations in the execution of the experiments or interfacial defects on the samples. The slight variability of the tests also contributed to the deviation from the normal contact stiffness values gathered from the FE model. Some such variables introduced are: placement of samples at the same point on corresponding fixtures for each test, alignment of the samples for contact, changes

to point of contact between samples causing different areas and nano roughness to be in contact, alignment of samples in correspondence to the force sensor of the microtester. All these areas will introduce slight variability to the testing conditions and the measured values of contact stiffness. However, it can be concluded that this study shows that microstructured interfaces can be designed to have highly repeatable normal contact stiffness.

4.4 Tailored normal contact stiffness

The next step towards tailored mechanical interfaces involved designing a study to explore how normal contact stiffness could be manipulated by designing specific micro topographies. A square wave pattern was again selected as this minimises any complexity that can arise during the microfabrication process detailed in Chapter 3. This enables the simple adjustment of the surface feature parameters. Polycarbonate was used as the material for this study as it is well established for use in the fabrication method used and in the previous repeatability study.

4.4.1 Interface design

An unstructured flat to flat contact was used as a benchmark, or 100% contact. The flat samples were produced by moulding polycarbonate using a nickel inlay that exhibits extremely low roughness in the region of a few nanometres. The structured interfaces were designed to exhibit square wave microfeatures that would produce a range of normal contact stiffnesses. The design interface consisted of a repeating square wave feature of variable width λ_f with a constant period of λ_p = 500 μm. The overall nominal contact size was kept constant at 10 x 10 mm. Adjusting the feature width allowed the designs to exhibit nominal contact area ratios of 0.2, 0.4, 0.6, 0.8, and 1. The designs are shown in Fig. 4.6. The height of the features in the designs was kept constant as varying this dimension would inevitably influence the normal contact stiffness of the interface.

The experiments with the varying contact area designs followed the same methodology as used in the repeatability study. The same experimental rig and equipment for measurement of the applied forces and interface displacements were used. Linear elastic FE models were designed and produced based on the idealised designs and the manufactured polycarbonate interfaces. This allowed a range of FE values of normal contact stiffness to be generated. The FE models highlighted the difference in behaviour between the idealised and manufactured designs.

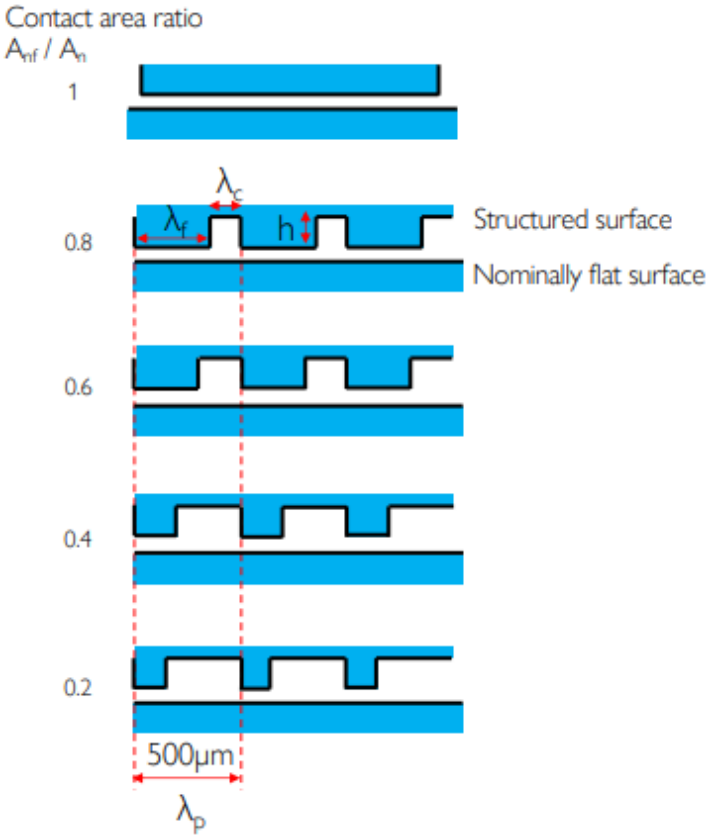

Figure 4.6 – Schematic of the square wave designs for different contact area ratios. Contact area ratio A_{nf}/A_n = λ_f/λ_p.

Table 4.3 – Contact area designs. Key dimensions shown at various stages of the fabrication process.

Feature depth (h)				Feature width (λ_f)				Contact area ratio		
Design (µm)	Silicon (µm)	as-produced PC (µm)	% Increase	Design (µm)	Silicon (µm)	as-produced PC (µm)	% Decrease	Design	as-produced PC	% Decrease
50	50.8 ± 0.3	52.3 ± 0.7	4.5	120	126.8 ± 2.9	80.6 ± 1.9	32.8	0.20	0.16	20
50	52.5 ± 0.3	52.8 ± 0.6	5.7	225	225.3 ± 2.6	171.4 ± 3.2	23.8	0.40	0.34	15
50	52.8 ± 0.4	53.9 ± 0.7	7.9	330	323.8 ± 2.3	275.4 ± 3.8	16.6	0.60	0.55	8.3
50	49.7 ± 0.4	51.1 ± 0.5	2.2	440	439.9 ± 2.6	387.8 ± 3.7	11.9	0.80	0.77	3.8

The dimensions shown in Table 4.3 show a significant difference from the design values of the interface to the final manufactured PC samples. The table reports the changes in the key parameters such as feature height, width, and contact area ratio. The silicon master feature dimensions are also indicated. For the feature heights, there is a slight stretching of the features as indicated from table 4.3. We see a maximum increase in the PC microfeature height of 7.9% from the design to produced polymer samples, shown in the 0.6 contact area ratio case. There is also a significant decrease in the feature widths and

contact area ratios from the designed interface to the as produced polymer samples - as much as 20% for the 0.2 contact area ratio design. The contact area ratio is obtained by dividing the nominal feature area, A_{nf}, the nominal area, A_n, of the sample.

It is believed the difference in the microfeatures from the design, to silicon, to the polymer samples is due to the stretching and elongation of the features during the injection moulding portion of the fabrication procedure. There is a combination of effects causing the difference in feature size. The features are stretched during the ejection stage of the moulding cycle, while the samples experience polymer shrinkage during cooling. This effect is described in Section 3.5.1 in more detail. There is some dimensional change from the design to the intermediate silicon masters, as shown in Table 4.3. However, most of the change is seen in the production of the polymer components and can be attributed to this effect. The effect was exaggerated, particularly in the 0.2 case. Even though the dimensions of the moulded squarewave differed somewhat from the as-designed case, this can easily be compensated for with appropriate experience (i.e. the design features can be adjusted to account for reductions or increases in dimensions such as feature height or width).

The samples manufactured for the different contact area ratios were still able to produce a range of contact area ratios. The next step was to test these interfaces to show the influence of varying an interfaces design dimensions (especially the contact area ratio) on the measured normal contact stiffness. Both the idealised and the modified waveform designs were used to generate the interfaces used in the FE models for comparison with the experimental results. The idealised models used the original design dimensions, while the as-produced version (modified FE) used dimensions measured from optical scans of the polymer samples. Fig. 4.7 details the difference between the waveform profiles for the idealised design, the modified waveform measured from the produced samples, and a cleaved cross section of a PC sample. The cleaved sample shown in Fig. 4.7(c) is representative of the cross section of all the microstructured interfaces.

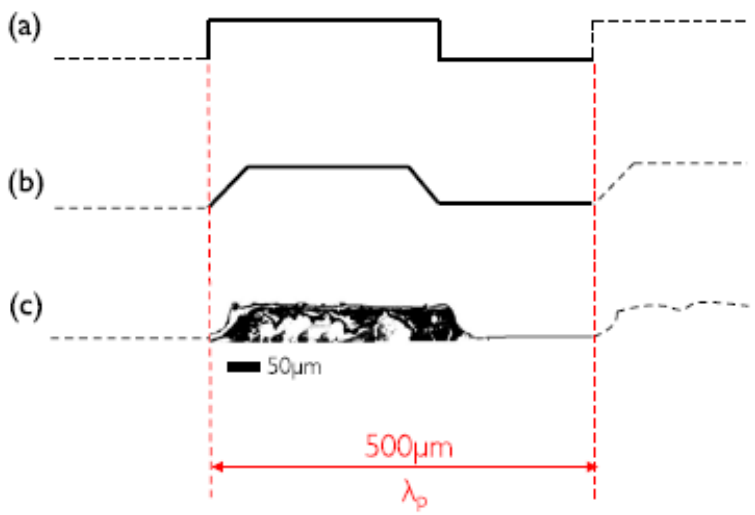

Figure 4.7 – Waveform used in the contact area study: (a) original waveform design (for idealised FE), (b) as-produced waveform with sloped sidewalls (for modified FE) and (c) SEM image showing cleaved cross section of polymer microstructure [118].

4.4.2 Contact area ratio results

As mentioned, the same methodology used for the repeatability study was followed for the mechanical testing of the contact area ratio designs. The force/displacement data was plotted in a similar manner, with a linear regression applied to the test trace to elucidate the contact stiffness of the microstructured interfaces. For these tests, two samples for each design were tested. Each sample was loaded to 1500 N in five separate repeat tests. This decision was made as repeatability of the microstructured interfaces had already been established. Therefore, a smaller number of samples could be tested for each interface design.

Fig. 4.8(a) details the normal contact stiffness versus the load for each of the interface designs. Fig. 4.8(b) details an individual case for clarity: this shows the 0.2 contact area ratio result. The five design contact area ratios, 0.2, 0.4, 0.6, 0.8, 1, correspond to manufactured measured sample contact area ratios of 0.16, 0.34, 0.55, 0.77, and 1. The traces shown in Fig. 4.8(a) show how the normal contact stiffness of the interface will evolve as more load is applied to the interface. There are slight variations in the behaviours of the interfaces, but they then plateau to a saturated contact stiffness. This saturation stiffness corresponds to the linear region detailed in Fig. 4.5, illustrating the calculation of the normal contact stiffness of an interface.

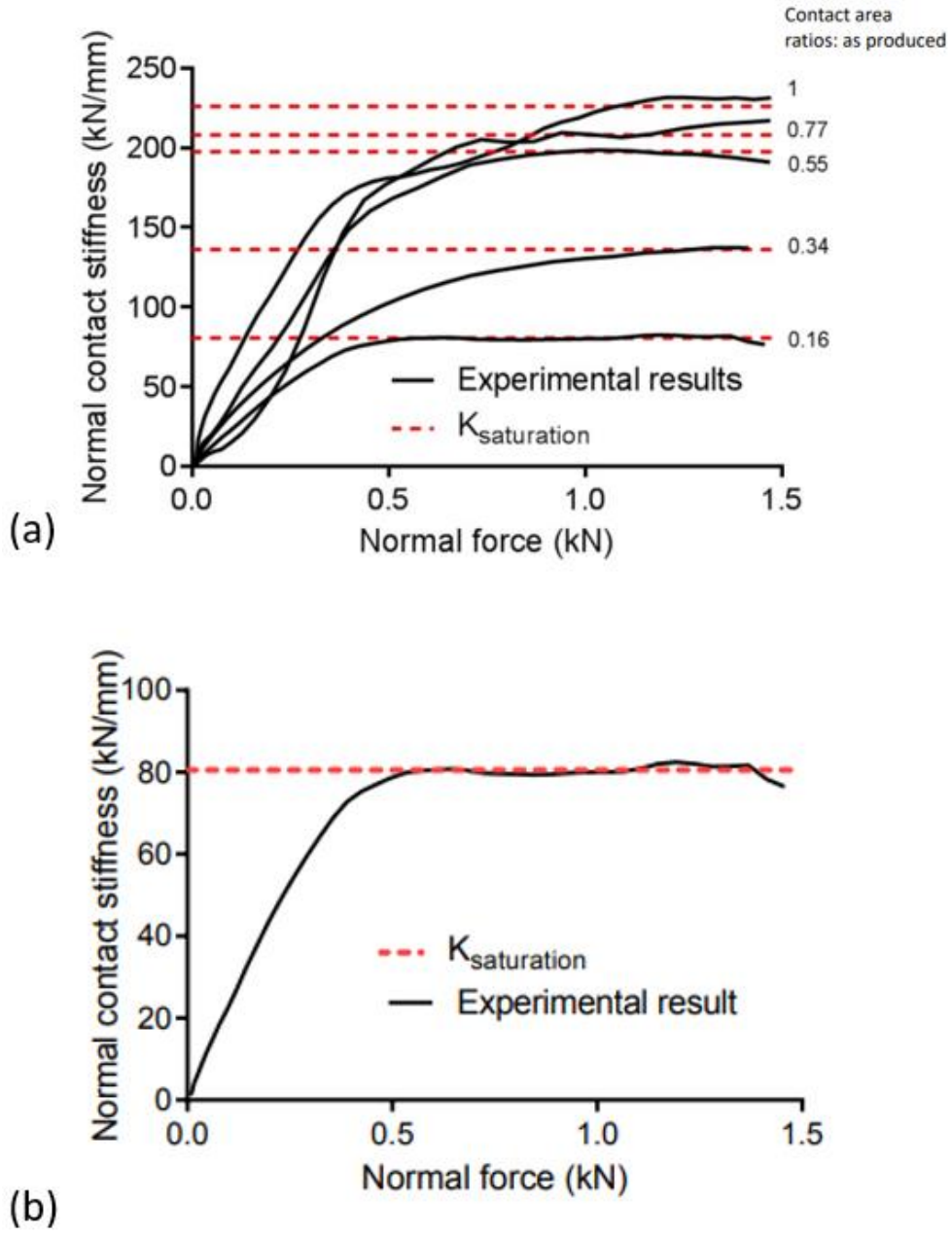

Figure 4.8 – (a) Normal contact stiffness versus normal force. All as-produced contact area ratio designs considered and (b) Normal contact stiffness versus normal force for the 0.2 contact area ratio design.

The saturated contact stiffness is the one used for comparison with the FE models. The saturated stiffness corresponds directly to how much material is in contact at the interface. As is expected as the contact area ratio increases, the measured normal contact stiffness of the interface increases. The higher contact area ratio designs result in interfaces displaying wider microfeatures with more material in contact across the interface designs. These wider, lower aspect ratio microfeatures exhibit a larger saturation stiffness. The results from the contact area ratio study are shown in Table 4.4.

Table 4.4 – Results from the contact area ratio tests. Experimental values of normal contact stiffness are compared to FE models based on idealised designs and measured as-produced interfaces.

FE – as designed		FE – as produced		Experimental			
Contact area ratio	Normal contact stiffness, K (kN/mm)	Contact area ratio	Normal contact stiffness, K (kN/mm)	Contact area ratio	Normal contact stiffness, K (kN/mm)	% Drop from 'as-designed FE'	% Drop from 'as-produced' FE
0.2	120.4	0.16	89.7	0.16	78.1 $\pm$4.0	35.1	12.9
0.4	165.4	0.34	148.2	0.34	141.5 $\pm$5.9	14.5	4.5
0.6	206.4	0.55	202.2	0.55	197.9 $\pm$5.1	4.1	2.1
0.8	225.9	0.77	216.8	0.77	208.9 $\pm$2.2	7.6	3.6
1	238.2	1	238.2	1	226.2 $\pm$10.3	5.1	5

The results in Table 4.4 illustrate the comparison of the measured experimental values and the two FE models for each design case. The experimental results show a low standard deviation, again indicating the repeatable nature of the microstructured interfaces.

The experimental results follow the same trends as exhibited by the FE models. The results from the 'as-designed' FE models differ from the experimental results (ranging from 5.1% to 35.1%). This is most likely due to the dimensional alterations between the as-designed FE and the experimental samples. However, when dimensional similarity is achieved, then the comparison improves. The results from the FE models designed to match the measured dimensions from the interface samples shows very good comparison to the experimental results. The results range from 2.1-12.9% difference when considering the as-produced FE model.

The trends of the evolution of the total normal contact stiffness when considering the contact area ratio follow very similar behaviour. This can be seen in Fig. 4.9 where the FE results from both as-designed and as-produced models follow a similar trend as the

experimental results. This is promising as it indicates that the FE models can adequately predict what value of normal contact stiffness can be expected from a produced interface. The FE models can be used to produce interface designs with an expected interfacial stiffness, which can in turn be used to support the manufacture of the microstructured polymer interfaces exhibiting similar properties.

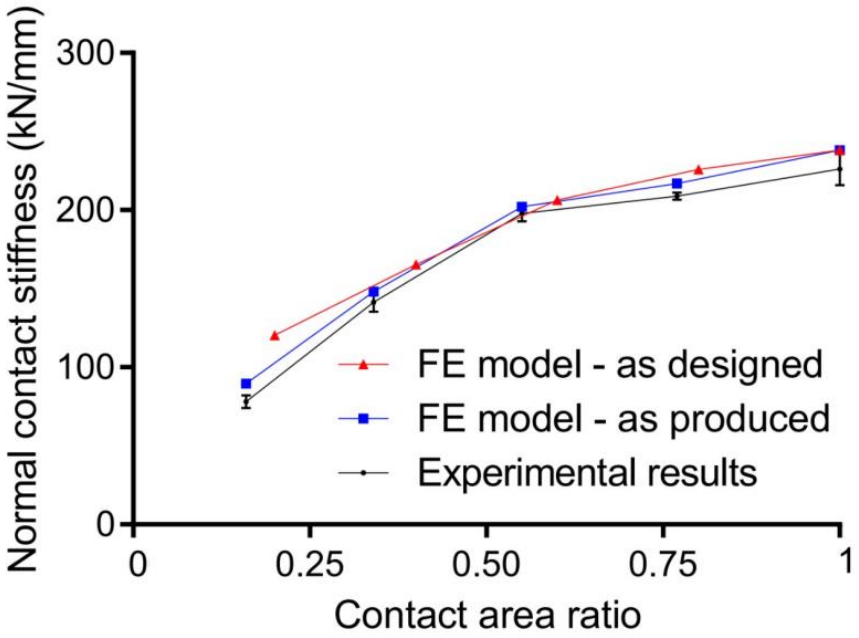

Figure 4.9 - Measured normal contact stiffness (at saturation) versus the contact area ratio. Results from both FE models and experimentat shown.

The study conducted here highlights that normal contact stiffness can be tuned to suit a specific purpose. This work has indicated that normal contact stiffness can be tailored through the modification of the design dimensions of the microstructured interface. This study considered how modifying the contact area ratio can influence the contact stiffness. As previously described, as the contact area ratio increased, the amount of material in contact with the nominally flat surface increased. This allows for a larger amount of material at each feature to resist the applied normal load, leading to an increase in the stiffness of the square wave micropattern. This can also be considered as a decrease in the aspect ratio of the microfeatures leading to an increase in the normal contact stiffness of the interface. We see in this study when we reduce from the contact area ratio from 1 to nearly 0.2, there is a decrease in the normal contact stiffness of almost three times.

The results here strongly indicate the ability to achieve repeatable and tailored normal contact stiffness through the micro-structuring of the polymer interfaces. This has a wide range of applications in the engineering field where accurate control of interfacial properties would be beneficial. As mentioned in the introduction of this chapter, contact stiffness can influence bone implant stability and function, vibration of joint interfaces, robotic gripper systems, and contact interfaces in precision machinery such as turbines and engines. The strategies presented in this work have focused on utilising novel fabrication routes that utilise injection moulding of one polymer type. This could be expanded into other thermoplastics via injection moulding or through 3D printed microstructured interfaces. This could again be expanded into the areas of metallic alloys through electroplating or metallic 3D printing.

4.5 Microfeature roughness

This final subsection aims to explain the behaviour of the trends of normal contact stiffness versus the applied normal load, seen in Section 4.4.2. In Fig. 4.8(a) and (b) the data shows the transition of normal contact stiffness from being initially load dependent to a saturation stiffness. Normal contact stiffness, K, can be thought of as a combination of stiffness inherent to the interface. Considering the approach of Medina et al [7]:

$$\frac{1}{K} = \frac{1}{K_{saturation}} + \frac{1}{K_{roughness}} \tag{4.1}$$

Here $K_{saturation}$ (the measured *K* when roughness on the feature tops is flattened by a significantly high load) can be considered to be equivalent to the bulk material contribution to contact stiffness K_{bulk} On the other hand, $K_{roughness}$ is the stiffness introduced by the roughness on the feature tops of the microstructured interface. The roughness on the feature tops is minimised by using an etched silicon master of extremely low roughness as a starting point for the fabrication of the interfaces. However, even a small amount of roughness is inevitable on the feature tops.

The linear elastic FE models used for comparison show a near constant value of $K_{saturation}$(in place for K_{bulk}) during the loading of the samples. Indicating that the features are in full contact, and roughness is completely omitted from the behaviour of the interfacial interaction within the FE models. The behaviour seen in Fig. 4.8 of the interfaces would indicate that there is a monotonic increase of the $K_{roughness}$ with the applied normal force.

This behaviour was confirmed using a simple linear elastic boundary element method (BEM) designed by Polonsky and Keer [138]. The rough surface topography modelled by the BEM was measured using optical profilometry. The scans were taken using the Contour GT, Bruker, US available at the JWNC. Seven different locations were scanned on the feature tops of the polymer samples, each with sample area of 133.5 × 176.7 μm^2 and in-plane resolution of 0.128 μm. The roughness statistics used are shown in Table 4.4.

Table 4.4 – Roughness statistics taken from optical scans. R_a and R_q provide centre line average and root-mean square roughness. σ_s is the standard deviation of the asperity and summit heights, κ_s is the mean summit curvature of all asperities.

Ra (μm)	Rq (μm)	$\sigma_s(\mu m)$	$\kappa_s(1/\mu m)$
0.026$\pm$0.007	0.048$\pm$0.008	0.040$\pm$0.004	0.071$\pm$0.009

Only one case is considered in this study to try to better understand the evolution of the normal contact stiffness. One of the repeatability study tests is considered. The topography used in the modelling is taken from a sample manufactured for the repeatability study. The nominally flat surface is assumed to have the same roughness as the feature tops. The interfacial gap and real contact area are calculated using the BEM model up to the 700N loading point for this case, after this point the saturation stiffness is reached and the influence of the $K_{roughness}$ becomes negligible. As is expected, the interfacial gap will reduce, and contact area will increase as the load increases. $K_{roughness}$ is considered in the BEM to be the absolute derivative of the applied normal force with respect to the interfacial gap. The results from the modelling are shown in Fig. 4.10. The interfacial gap and contact area are shown in Fig. 4.10(a).

The interfacial stiffness increases exponentially before reaching a saturation. The modelling is plotted along with the experimental data shown in Fig. 4.10(b). Here, we see the approach of a saturated stiffness and an end to the load dependent region of contact stiffness which is introduced by $K_{roughness}$. Even at low roughness values such as those exhibited on the feature tops, there will be a load dependent element introduced in the evolution of the normal contact stiffness. It can therefore be concluded that the deterministic nature of the normal contact stiffness exhibited by the structured interfaces can only be achieved after a certain loading has occurred and the feature top roughness stops having an influence on the normal contact stiffness. The BEM predicts a sharper increase in the observed normal contact stiffness influenced by the roughness. It is hypothesised that this is due to the lack of plasticity introduced by the modelling. The saturation achieved in the modelling is the same, Fig. 4.10(b). However, this increase is much steeper and therefore overestimating the stiffness of the rough asperities on the feature tops. If plasticity were included in the BEM, then we would observe a more gradual increase in the normal contact stiffness approaching the $K_{saturation}$. This would result in a more realistic behaviour of $K_{roughness}$.

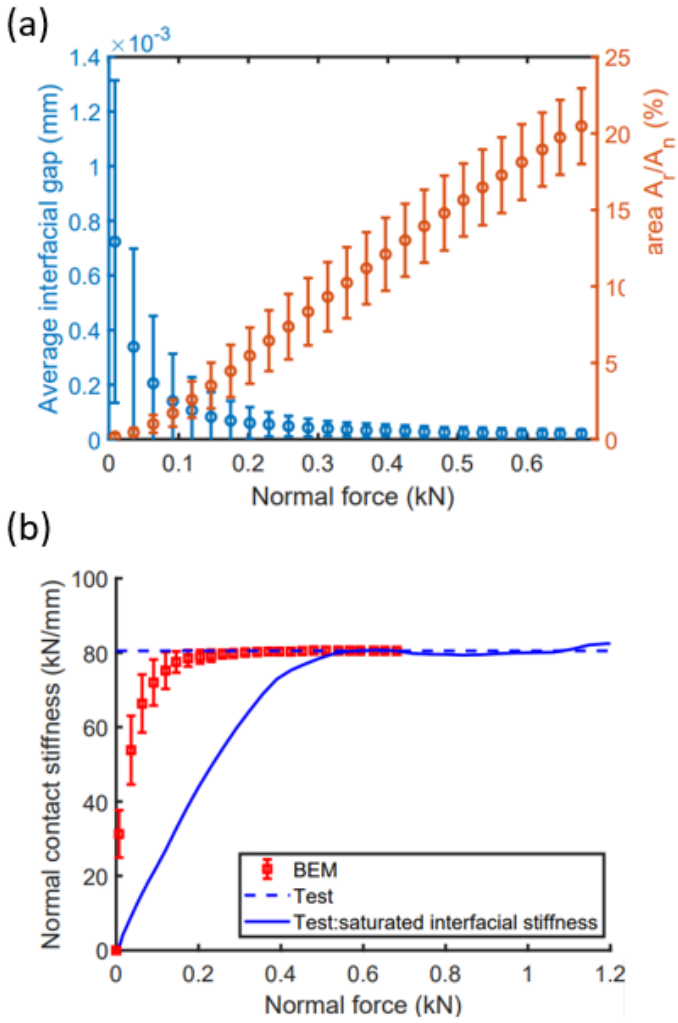

Figure 4.10 – (a) Evolution of average interfacial gap (left y-axis) and percentage of real contact area (right x-axis) with respect to normal force – BEM model of the rough surface polycarbonate contact pair and (b) Comparison of the measured and numerical (BEM) total normal contact stiffness results. – Note the average interfacial gap here is the mean gap between the two deforming rough contact surfaces (i.e., the rough surfaces representative of the feature tops).

Plastic deformation of the rough surface asperities can be quantified using the plasticity index [19].

$$\Psi = \frac{E^*}{H}\sqrt{\sigma_s \kappa_s} \tag{4.2}$$

Where $E^* = \frac{E_{PC}}{2(1-\nu_{PC})}$ is the effective modulus of the polycarbonate rough surface pair, H is the hardness of polycarbonate estimated using $H = 2.8S_y$ where S_y is the yield strength of polycarbonate. Calculating using E^* = 2350 MPa, S_y = 60 MPa and values for σ_s and κ_s taken from optical measurements shown in Table 11, this gives a plasticity index of $\Psi = 1.41$.

This indicates that the asperity deformation is predominantly plastic. This means that if plasticity were included within the model, then we would observe an increased percentage area of contact on the feature tops as normal load increased. This would soften the curve of the BEM as the interfacial stiffness would be decreased, bringing the BEM curve (Fig. 4.10(b), closer to the behaviour seen in the mechanical tests.

4.6 Conclusion

This chapter has explored the viability to use microstructured polymer interfaces to achieve tailored and repeatable normal contact stiffness properties. Finite element models were used to formulate initial square wave designs that exhibited controlled normal contact stiffness measurements. These designs were then manufactured using the fabrication process outlined in chapter 3 of this thesis.

The 'as-produced' interface dimensions differed from the initial FE model designs, this resulted in alterations to the normal contact stiffness measurements of the manufactured surfaces. However, should exact dimensions be required then the process can easily be tailored to achieve specific micro-structure characteristics and normal contact stiffness. For the work here, the FE models were tailored to accommodate the changes in dimensions in the manufactured surfaces. The results from the tailored predictions follow very similar trends and magnitudes to the mechanical tests of the microstructured interfaces. High repeatability between the surface designs and repeat samples was also observed.

The results in this chapter indicate the ability to tailor microstructured interfaces to exhibit user defined normal contact stiffness properties. The concept is simple in theory, by adjusting the feature widths and spacing then we can control the normal contact stiffness of an interface. This could also be extended studies where the feature height can be varied to manipulate the normal contact stiffness of an interface. It was shown that the contact stiffness can be reduced by almost three times when reducing from unity contact to 0.2 contact area ratio. The capabilities of producing tailored and repeatable normal contact stiffness become useful in many engineering situations: mechanical joints – friction and vibration, prosthetic interfaces – hip implants and knee replacements, robotic gripping

systems, and the control of precision mechanical design devices. The methods here can also be extended to various polymers using injection moulding and 3D printing, also metallic alloys via metal 3D printing. This will allow the exploration of repeatable and tailored normal contact stiffness in a wider range of engineering environments.

Chapter 5.

3D printing and Rapid Replication of Advanced Numerically Generated Rough Surface Topographies

5.1 Introduction

Up to now, we have been considering the fabrication and contact stiffness of structured non-random surfaces. However, there are many situations in interfacial interactions where a rough surface is unavoidable or even desirable. This chapter presents a technique that allows the user to design and manufacture high quality rough surface topographies with pre-defined roughness characteristics in various polymer materials – essentially allowing for the tailoring of rough surfaces and their contact stiffness. The technique begins with an advanced surface generation tool that allows the user to design a surface with desired rough topography characteristics. The designed topography can then be 3D printed to be used as a master surface for replication using two techniques: polymer casting and injection moulding. These methods allow for high quality rough surface polymer replicas to be produced in a wide range of polymers. This chapter will fully detail the fabrication route that has been outlined and explore the quality of replication across the replication methods. Various materials are explored to highlight the versatility of the rough surface manufacturing methods introduced. Design studies were formulated to explore the capabilities of the fabrication methods. Key results are presented to illustrate the benefits and scope of the surface generation and manufacture tool.

The fabrication tool was developed with the aim of making rough surface design and production more readily available to tribology and surface engineering researchers. Surface interactions and phenomena are intertwined with a surface's topography. Mechanical and biological behaviours surrounding surfaces are directly influenced by the topographical

characteristics exhibited by a surface. Therefore, the main application of the fabrication tool introduced here is to provide a powerful research tool where rough surfaces can be controlled and investigated. The tool allows for topographical characteristics to be isolated and investigated to explore their influence on phenomena such as friction, adhesion and lubrication, cell engineering and growth, biofouling, and aerodynamic drag.

Surfaces and interfaces will inherently exhibit a roughness at some level. Even the flattest surfaces such as silicon wafers used for MEMS fabrication will have a nanoscale asperities contributing to a surface roughness. Critical interfacial processes such as friction, adhesion and lubrication, wear, and cell growth are heavily influenced by the characteristics of a surface's roughness. Generally, the roughness of a surface can be unpredictable as it can be produced naturally or as a derivative of the manufacturing process. Typical surface roughness will be multiscale and random in nature. The design of rough surfaces is difficult to control for research or engineering applications. The tool presented here aims to control the rough surface topographies and produce them with tailored predefined characteristics. The controlled designed surface can then be replicated in various polymer materials to suit the component's specific purpose.

Surface engineering aims to design and manufacture surfaces that allow the optimisation of the performance of an engineering system. Surface modifications are introduced to control the functionality of a surface and engineering system. Various methods are employed to facilitate the manufacture of engineering surfaces in a wide range of materials. Some examples are laser structuring, embossing, treatments and coatings, micro and nano injection moulding, additive manufacture, and lithographic techniques. Injection moulding and additive manufacture have been used to produce surfaces for microfluidic devices [90, 139-140], and MEMS [141, 142]. Surface modification through laser structuring is particularly popular and used in many sectors: improvement of performance of optical devices [67], solar cell design [68], metallic joints [70], biomedical surfaces and implants [143, 144]. A crucial area that this fabrication method draws inspiration from is biomimetic design and surface replication. Surface moulding and replication is common in bio-inspired design where surfaces will be replicated and introduced to a system to improve the

engineering solution [145-149]. Typically, existing processes for generating a controlled surface will produce patterned structures, such as those seen in MEMS design, i.e. a square wave or an array of pillars [90, 135, 136]. The work presented in this chapter allows for complex, multiscale rough surfaces to be designed and produced. The advanced surface generation approach is combined with three additional fabrication techniques to produce a new rough surface manufacturing technique. The three main techniques utilised are: 3D printing, micro-injection moulding and polymer replication.

An overview of popular 3D printing methods was given in Chapter 2. The 3D printing methodology used in this work is the SLA (stereolithography) process. 3D printing has previously been used on a microscale but the designs are typically restricted to simple geometric patterns and arrangements. Some popular examples include optical devices [150], microfluidic devices [140, 151-154]. The fabrication tool introduces the concept of manufacturing designed, irregular, and multiscale rough surfaces. 3D printing is ideally suited for this task as the technology can facilitate the production of an arbitrary topographical structure, so long as the resolution limits of the printer are accounted for. The first step in the fabrication process is to produce a printed topography from the numerically generated surfaces. The printed topographies can then be used for either polymer casting or as an inlay for injection moulding. The SLA printing process allows for predefined patterns to be built up layer by layer from a resin that is cured using a laser. Irregular topography additive manufacture has been utilised in niche areas previously, generally with a focus on biomedical engineering. Tissues and scaffolds have been printed to support the rehabilitation process of patients [155-157]. The aim of this project was slightly different. As previously stated, the goal was to generate and produce rough surface topographies with controlled characteristics which can then be printed and replicated in polymers. This would appeal to the research community as certain interfacial phenomena influenced by surface roughness can be explored in a more controlled environment. The techniques presented in this chapter drew inspiration from work of Benett et al. [158] for the Contact Mechanics Challenge 2017 [159]. Here the researchers 3D printed a scaled rough surface topography taken from an AFM scan to be tested experimentally for comparison with numerical results.

However, the work presented in this chapter differs as the topographies that are printed for replication are numerically generated and designed to suit the user's needs. In addition, the 3D prints here are integrated with two replication methods allowing for the rapid production of high-quality rough surface polymer samples.

Injection moulding was chosen as one of the replication methods within the fabrication route as it is a particularly versatile manufacturing technique. Injection moulding allows for various polymers to be manufactured into products on a macroscale from furniture and automotive components to micro and nano-scale bespoke manufacture [81-89]. The method is ubiquitous in the polymer manufacturing industry, particularly for mass produced components. Injection moulding boasts high efficiency, dimensional accuracy, low part cost, and high production rates. The wide range of supported materials also makes injection moulding particularly appealing to many industries [160]. The dimensional accuracy and high precision down to the nanoscale has prompted researchers to investigate its uses for surface engineering. The process is ideally suited for replicating precise micro and nano topographical features, and by extension a good fit for the fabrication route described in this chapter. There are, of course, many variables associated with injection moulding as described in Chapter 3. This can mean a lot of process optimisation is required to achieve good replication, especially when considering complex, irregular, and multiscale rough surfaces. As previously discussed (Chapter 3), there are a wide range of options when considering inlay materials for injection moulding. In this work, the 3D printed rough surface is integrated into a mould inlay and used directly for replication. This takes inspiration from a recent work where 3D printed inserts were used to produce microfluidic devices in various polymer materials [140]. 3D printed inserts have also previously been used to produce micro-structured devices [152-154]. This process is novel but is slowly gathering interest and becoming a more established method for producing inlays for injection moulding.

Polymer casting is the second route that is employed to produce rough surface replicas. This technique is commonly used in the field of biomimetic surface replication. Casting polymers onto complex biological surfaces allows for the topographies to be duplicated and

investigated for engineering solutions. The process is simple, it works by isolating the area of interest and then pouring a liquid polymer onto the desired surface, used as a master. This is typically followed by another casting step to produce a positive polymer replica of the original surface [161-164]. This method allows topographies occurring in nature to be emulated, with their beneficial characteristics mimicked. The beneficial attributes and mechanisms of the surfaces can then be introduced to engineering surfaces. This aims to improve an engineering system's performance or influence how it interacts with its surrounding environment. We often observe topographical structures in nature that embody an optimum design that engineers wish to emulate. The polymer casting method can isolate the desired characteristics of a surface and integrate them into real engineering surfaces. Some examples include hydrophobicity replicated from leaf structures [165], antifouling topographies taken from nature to be used for aerofoil and marine surfaces [166, 167], improved solar cell light harvesting capability inspired by leaf surfaces [168] and introducing self-cleaning and anti-reflective mechanisms to solar cells [169]. These examples provide a glimpse into a world of research where a wide range of polymers are used to replicate complex natural topographies to improve engineering design. The rough surface designs presented in this work resemble the multiscale irregular topographies exhibited in the natural world. Therefore, polymer casting is particularly suited for producing high-quality rough surface polymer replicas.

5.2 Materials and methods

This section will summarise and detail the fabrication route. The process begins with an advanced surface generation tool used to produce the rough surface topography designs. This was implemented in MATLAB. Once the desired surface design is produced, this can then be 3D printed using the SLA printing process, this is used as a master surface for the two replication methods. The final step uses injection moulding or casting to produce the polymer replicas of the rough surface topographies. These processes are further detailed in the subsequent sections.

5.2.1 Surface generation

Three distinct topographies were generated using the MATLAB surface generation tool developed by Xu et al. [170]. The toolbox is planned to be released to the public as an opensource tribology toolbox. However, it is still in development by Dr Yang Xu at this current time. The surfaces generated for this work exhibited three areal root mean squared surface roughness, Sq. The surfaces were designed to be isotropic in all directions and multi-scale in nature, this aimed to simulate a real engineering surface. The MATLAB rough surface toolbox was generated based on previous literature that details algorithms for characterising and emulating rough surface topographies and their behaviours [171-173]. By extension, these algorithms can be manipulated to generate topographies desired by the user by customising key roughness parameters and the spectral contents of the surface. The main parameters that can be altered within the toolbox are areal roughness, Hurst exponent, and the upper and lower frequencies that define the nature of the surface. This allows the slope of the asperities, their kurtosis, and frequency to be altered along with the overall roughness of the surface. The rough surface $h(x,y)$ is generated based on an axisymmetric power spectrum density (PSD) $S(f_x,f_y) = S(f) = \sqrt{f_x^2 + f_y^2})$ defined in the frequency (inverse of the wavelength) domain as shown in Fig. 5.1. The PSD value decreases in a power law behaviour between the lower and upper cut-off frequencies f_l and f_s as:

$$S(f) = C_0 f^{-2-2H} \quad f \in [f_r, f_s] \tag{5.1}$$

The PSD value elsewhere is strictly zero. $H \in [0,1]$ is the Hurst dimension.

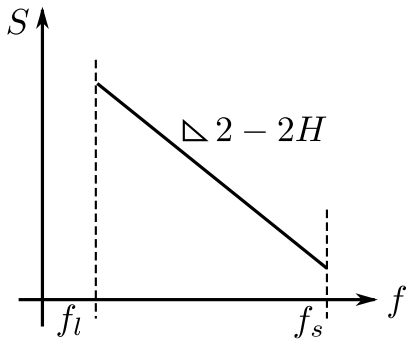

Figure 5.1 – Schematic of the log-log plot of an axisymmetric PSD.

The generated rough surface has lateral dimensions of $L_x \times L_y$. Consider a

periodic rough surface topography $h(x,y)$ with period of L_x and L_y in the x and y directions, respectively. The following Fourier transform pair is used (Eq. 5.2 and 5.3):

$$h(x,y) = \sum_{k=-\infty}^{\infty} \sum_{m=-\infty}^{\infty} H_{km} e^{+i2\pi\left(\frac{kx}{L_x}+\frac{my}{L_y}\right)} \tag{5.2}$$

$$H_{km} = \frac{1}{L_x L_y} \int_0^{L_x} \int_0^{L_y} h(x,y) e^{-i2\pi\left(\frac{kx}{L_x}+\frac{my}{L_y}\right)} dxdy \tag{5.3}$$

where $f_x = k/L_x$, and $f_y = m/L_y$. Since the auto-correlation function and the PSD also follows the above Fourier transform pair, we immediately have the following identity:

$$S(f_x, f_y) = H_{km}\overline{H_{km}} = |H_{km}|^2 \tag{5.4}$$

Given that $S(f_x, f_y)$ is known from Eq. (5.1), we can reconstruct the complex spectral H_{km} based on its absolute value $|H_{km}|$ solved by Eq. (5.4) and a random phase $\theta_{km} \in [0, 2\,\pi)$

$$H_{km} = |H_{km}|[cos\,(\theta)\, + i\, sin\,(\theta)\,] \tag{5.5}$$

We can then substitute H_{km} into the inverse Fourier transform in Eq. (5.2) over the discretised frequency domain predefined by the user, f_l and f_s. This gives us the designed topography, shown in Fig. 5.2(a). Fig 5.2(b) illustrates the agreement of the PSD exhibited by the generated topography and Eq. (5.1) that defines the areal surface. The generated rough surface topography is then integrated as a point cloud into a CAD modelling software. From here the point cloud can be used to generate a mesh representative of the rough surface topography. The data used to generate the surface must be sufficiently dense to allow a fine mesh to be generated of the topography. The meshed surface is then used to generate an STL file suitable for use with 3D printers.

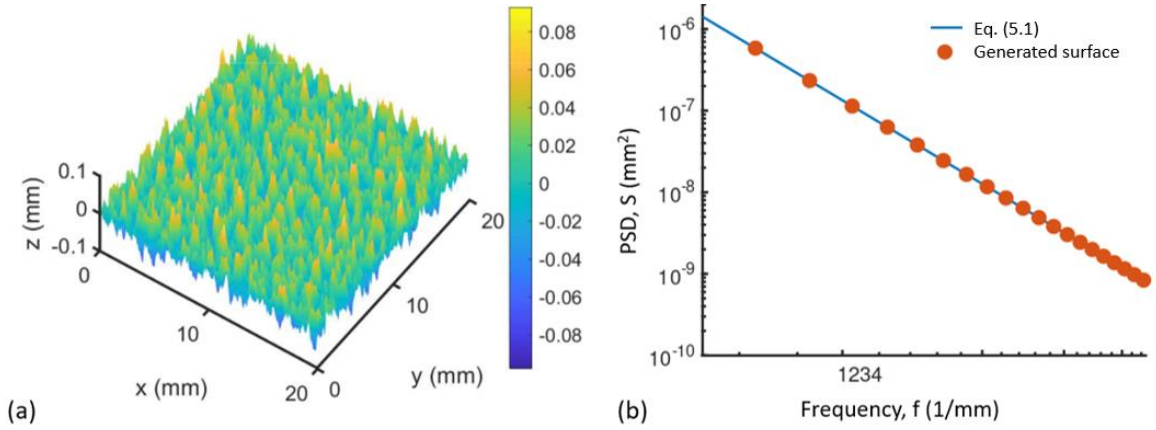

Figure 5.2 - (a) Example 3D plot of the generated topography and (b) Comparison between the radially averaged PSD $S(f) = \frac{1}{2\pi}\int_0^{2\pi} S(f,\theta)d\theta$ of the generated topography in (a) and the deterministic form in Eq. (5.1). The lateral size is $L_x = L_y = 20$ mm; Parameters in the deterministic PSD are: $f_l = 10/L_x$, $f_s = 128/L_x$, $H = 0.7$, $C_0 = 1.7064 \times 10^{-5}$; $S_q = 25$ µm. Number of sampling points: 256×256 [198].

The three distinct topographies were primarily designated using their respective areal root mean square heights, *Sq*. They were designed to have *Sq* values of 25 µm, 50 µm, and 100 µm. The surfaces were designed to measure 25 x 25 mm. The generated surfaces were then integrated into appropriate surrounding designs depending on which replication route they would follow. For the injection moulding, the three surface designs were all integrated into an inlay block that was designed to fit into existing tooling for the injection moulding machine. The inlay block measured 27.7 mm x 77.7 mm x 5 mm. For polymer casting, the rough surface designs were integrated into a border measuring 30 mm x 30 mm. This border created a distinct boundary for replica casting and a cavity where the rough surface design could be held.

5.2.2 3D printed rough surface master

The designed surfaces were printed using the Form3 printer (Formlabs, USA). This printer is an SLA printer with high dimensional accuracy and material versatility. Formlabs supply various resins that provide the user with a range of materials to choose from. For this work, the proprietary Clear V4 resin was used. The Clear V4 resin produces durable components with high quality surface finish, and allows the printer to operate at its highest quoted vertical resolution of 25 µm. The SLA process works by curing the resins using a laser that polymerises the resin in predefined patterns. The process works in a serial fashion, constructing the components layer by layer onto a vertically moving build plate. Fig. 5.3(b) illustrates a simplified diagram of the SLA process.

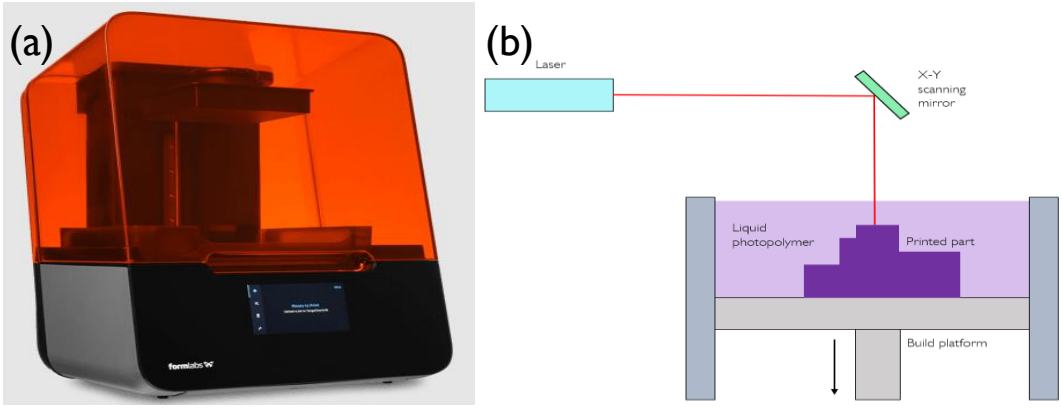

Figure 5.3 – (a) Form3 printer and (b) Diagram of SLA 3D printing process.

Once the components are printed, they are transferred to a washing unit (Formwash, Formlabs, US) that cleans the products in IPA. The components are submerged in IPA and agitated using ultrasonic frequencies for a minimum of 10 minutes. This removes excess photo resin from the 'green' components before curing. Once all excess resin is removed, the components are transferred to the thermal UV curing oven (FormCure, Formlabs, US). The Clear V4 resin is cured at 60° for 30 minutes and this allows the components to achieve the optimum material properties and durability.

5.2.3 Replication from 3D printed master surface

The replication from the master surfaces is achieved using two distinct routes: injection moulding and polymer casting. Both methods support high quality fabrication but also have additional individual benefits. Injection moulding was selected as it provides a high

throughput rate while providing excellent surface quality and part similarity. It provides a platform for rapid prototyping in large quantity production runs. The process has previously been used for replicating micro and nanostructures [89, 92, 93, 160], so it is ideally suited to this work. The drawback for injection moulding is that the process is typically limited to thermoplastic polymers. The injection moulding fabrication route is detailed in Fig. 5.4(a). Polymer casting was selected as the other method of replication as it provides additional versatility in terms of material availability. The process is established as an effective replication method to produce high quality micro and nano topographies. The process is simple and requires less specialist equipment and expertise when compared with injection moulding, making it more accessible. However, polymer casting does have a vastly reduced throughput. The process is readily used in biomedical engineering for prototyping microstructured devices such as microfluidics. Polydimethylsiloxane (PDMS) is cast onto a designed master surface, typically laser cut or on an etched silicon master. Other common polymers include (polyvinyl siloxane (PVS), polypropylene (PP), polymethylmethacrylate (PMMA)). These materials have been shown to replicate complex natural surfaces for use in biomimetic design [145-149]. A simplified diagram of the polymer casting fabrication route is shown in Fig. 5.4(b).

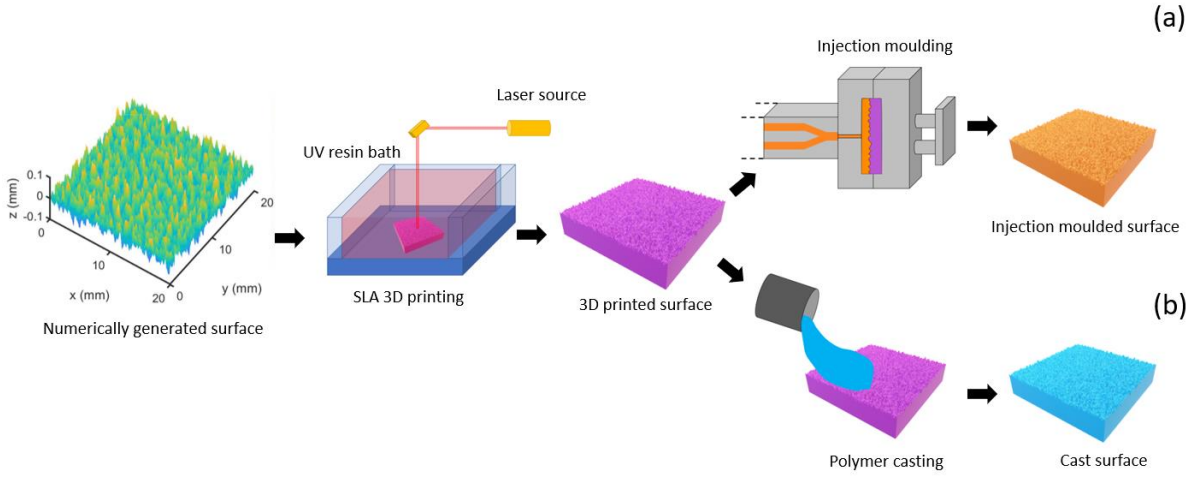

Figure 5.4 – Simplified process diagram detailing polymer fabrication routes used to produce the rough surface topographies with Injection moulding process flow (a) and polymer casting process flow (b).

5.2.4 Injection moulding

As previously mentioned, the 3D printed rough surface is integrated as an inlay tool for the injection moulding. To achieve the best results from the manufacturing process, key parameters must be optimised. Injection mould temperature, injection velocity, tooling temperature, holding pressure and time all must be tailored to the specific design situation to achieve high part quality – in this case, high surface replication quality. A study was executed to tailor the key manufacturing parameters to achieve high surface replication quality.

For this work, polystyrene (PS) (1810 Crystal Polystyrene, Total Petrochemical and Refining, Belgium) was used to produce the rough surface polymer replicas. PS was chosen due to its high durability and surface replication abilities. The injection moulding machine used for this work was the Victory 28 injection moulding machine (Engel, Austria). The polymer was heated to 260°C before being injected into the mould cavity at a velocity of $1 cm^3 s^{-1}$. The mould cavity measures roughly 4 cm^3 so the material volume was programmed accordingly. The polymer is held in the mould cavity to cool for 35 s at a pressure of 800 bar. This long cooling time and high holding pressure aim to ensure high replication quality by minimising component distortion. Before full ejection, the mould cavity is partially opened to allow further cooling to prevent polymer stretching and part distortion. The 3D printed inlay presenting the rough surface for replication has reduced thermal conductivity compared with metallic inlay components. This reduces the cooling rate of the injected parts so care must be taken with the cooling cycle and part ejection to maintain component fidelity. Once the component is sufficiently cooled, then the tooling can be fully opened, and the part ejected. This process of using 3D printed tooling was developed and optimised recently for microfluidic manufacture by Convery et al [140].

5.2.5 Polymer casting

The polymer casting replication method uses the 3D printed rough surface as a master mould. The selected polymer resin is then poured onto the 3D printed topography, as seen in Fig. 5.4(b). The resin is then left to cure for an adequate time as per the manufacturer's guidelines: the curing time varies depending on what polymer resin is cast. Three different

polymer resins were cast onto the three distinct rough surface designs: ultra-low viscosity Epoxy resin, PDMS, and polyvinyl siloxane (PVS). The PVS uses a slightly different casting procedure to the PDMS and epoxy – this is detailed in Section 5.2.6.

The casting procedure begins with the 3D printed rough surface topography; the design used is the 30 mm x 30 mm bordered samples. These are glued to the bottom of a petri dish. The polymer resin is then poured carefully onto the 3D printed surface and left to cure accordingly. The mixtures are poured at a steady rate to avoid trapping air bubbles between at the interface of the 3D print and the resin. All polymers are mixed in the ratios given by the manufacturer's guidelines. The epoxy resin (Epoxy ResinL & Hardener S, Conrad Electronic SE, Hirschau, Germany) consists of two parts, the resin and hardener are mixed at a ratio of 10:4.8 for 5 mins before being placed into a desiccation chamber for degassing. This removes any air trapped in the mixture. The mixture is then poured onto the 3D printed samples and left to cure for 15 hrs at room temperature (20 ± 2°C), as specified by the manufacturer's guidelines. This curing time can be decreased significantly by increasing the curing temperature. Once cured, the epoxy can be carefully removed from the 3D prints so as not to damage or distort the surface replicas. The PDMS follows the same procedure but with slightly different mixing ratios and curing times. The two component PDMS solution used in this work was Sylgard 184 Silicone Elastomer (Dow Inc., United States). The resin was mixed at a monomer to crosslinker ratio of 10:1. If stiffer samples are required, then the ratio of monomer to crosslinker can be reduced. The PDMS is degassed 3/4 times for 5 mins to remove all trapped air in the mixture. The PDMS resin can then be carefully poured onto the 3D printed surface – again care must be taken to avoid trapping air at the 3D print resin interface. The samples are then degassed for a further 30 mins to remove any excess air. The resin is then cured in an oven at 60°C for 4 hours. The PDMS replicas can then be easily peeled from the 3D printed samples. Less care is needed here due to the elastomeric nature of the cured PDMS.

5.2.6 PVS replica moulding

The PVS (President, Coltene Whaledent, Altstätten, Switzerland) replica moulding method follows a similar procedure as the initial casting method described in Section 5.2.5. However, the mixing of the monomer and the crosslinking agent is controlled via a manufacturer designed applicator gun. The dispenser nozzle mixes the two components before exiting the guns opening. PVS is typically used in dentistry to make negative moulds of patients teeth. The material is able to capture the topographies of teeth with high accuracy, making it an ideal candidate for the rough surface replication. The PVS mixture is applied carefully and methodically to the 3D printed topography. This again avoids any excess air bubbles trapped at the polymer to 3D print interface. Once the critical area of the sample is covered, a flat piece of PMMA is used to gently compress the PVS mixture into the 3D print. The PVS resins are more viscous than epoxy and PDMS and, so, have less flowability. The compression of the uncured resin ensures complete topographical coverage and replication. The PVS resins polymerise quickly and are fully cured in 10 mins at room temperature. Once the PVS is cured, it can be peeled from the 3D printed mould. The ultra-light body PVS resin was utilised in the replication of all three of the distinct surface designs. A design study to analyse how the viscosity of the polymer resin varies replication quality was carried out using various PVS resins. This was achieved using four different PVS resins from the same manufacturer, ultra-light, light, regular, and heavy body resins. These PVS resins were tested on the *Sq* 25 μm design 3D printed topography.

5.2.7 Surface Characterisation

The topographies were scanned and analysed to investigate key surface parameters and physical dimensions produced in the samples. For this work, it was particularly important to ensure a good translation from the designed topography to the 3D printed rough surface. Also required is good surface replication between the 3D print and the injection moulded or polymer cast surface replicas.

The surfaces were all scanned using optical profilometry (InfiniteFocus, Bruker-Alicona, Austria). The optical profilometer was used with its 5x optical zoom to gather all the scans. Scans were made at twelve key points across the 3D printed samples and the polymer

replicas. The key points were kept consistent across the samples to ensure accurate comparison. The samples were always aligned accordingly to ensure the points remained consistent. The optical scans for the 3D printed samples and polymer replicas were collected and used to quantify the quality of the replication in the fabrication process. The methods for quantifying replication quality are detailed in Section 5.3. For the injection moulding, Parts 10, 20, and 30 were initially taken and analysed to ensure good surface replication. However, Parts 50, 100, 150, and 200 were also analysed to ensure a good level of durability of the 3D printed inlay. For the polymer casting method, three replicas for each of the rough surfaces (25 μm, 50 μm, 100 μm) were taken for each material (Epoxy, PDMS, and PVS). The scans taken over all samples were used for the assessment of the replication quality of the fabrication processes outlined.

5.3 Replication quality analysis

It was decided to utilise two methods to quantify the surface replication quality for both fabrication routes. The methods used were the cross-correlation method, and a surface data 'point-to-point difference measurement' method. These two methods were able to be directly used with the optical scans taken from 3D printed and replica surfaces.

5.3.1 Cross-correlation method

This method it the primary method that was used to analyse the surface replication quality. The normalised cross-corelation method allows the user to compare two datasets and output a value corresponding to the similarity between the two. In this case, the datasets being considered are surface profiles taken from the 3D print and surface replicas. The function used to define the cross-correlation is as follows:

$$CCR = \frac{\sum_{i,j}[(Z_A(i,j) - \bar{Z}_A)(Z_B(i,j) - \bar{Z}_B)]}{\sqrt{\sum_{i,j}(Z_A(i,j) - \bar{Z}_A)^2}\sqrt{\sum_{i,j}(Z_B(i,j) - \bar{Z}_B)^2}} \quad (5.6)$$

The cross-correlation function shown in Eq. (5.6) is defined as the ratio of the covariance to the root-mean variance of the datasets (or line profiles in this case). The Z parameter is the

height of a data point within the surface profile at a point '*i*, *j*'. The subscript *A* is typically used to refer to the original or master surface, here the 3D printed topography. While *B* refers to the replica profile. The $\bar{Z}$ represents the mean value of the heights of the profile being analysed. The cross-correlation ratio will output a value ranging from -1 to 1. A value of 1 represents completely identical profiles, while a value of 0 represents completely unrelated or dissimilar profiles i.e., very poor replication. The average of nine profiles from each case was considered to generate a mean CCR measurement for each individual replication case. The function used here was suggested for use by the National Institute of Standards and Technology [174], typically this process is used for signal processing and analysis. However, it lends itself well to analysing surface profiles as well. This process has previously been used to analyse the quality of replication between complex natural topographies exhibited by the leaves of various plant species and their polymer replicas [164].

5.3.2 Point-to-point difference measurement

The secondary method used to quantify the replication quality is based on a data point method. The point-to-point difference method allows the comparison between the surface data of the optical scans of two surfaces. This method was implemented via the 'Difference Measurement' module provided by Alicona's InfiniteFocus software (Bruker-Alicona, Austria). A simplified visualisation of the process is detailed in Fig. 5.5. The method begins by taking optical scans of a critical area, this point must be well aligned so that the areas match closely in the master and replicated surfaces scans. The scans are taken from the 3D print and the polymer replica and then input into the difference module for comparison. The 3D printed surface is treated as a reference geometry which the replica surface can be compared against. The datapoints that make up the scanned geometries are compared and measured to evaluate the similarity between the topography datasets. An initial automatic alignment is performed for the surfaces – this is only allowed if the surfaces have 80% identicality [175]. Once the surface datasets are aligned, the similarity can be measured. The difference in heights between the dataset is the recommended procedure by Alicona for surface replication analysis. This works by generating a three-dimensional vector between

the two closest data points on the respective topographies. A mean displacement measurement is then output that corresponds to the distance between the points on the 3D printed and replica surface. The automatic alignment aims to minimise the error between the comparison of incorrect datapoints. The mean displacement measurement procedure is executed across the whole surface geometries. The displacement outputs are then used to calculate a mean difference in height value for the comparison of the topographies. Low output values from the mean difference calculation indicate a high level of replication. The results from the difference measurement are used as a verification method for the trends exhibited from the CCR analysis. This means that high values of CCR correspond to low values of mean height difference and vice versa.

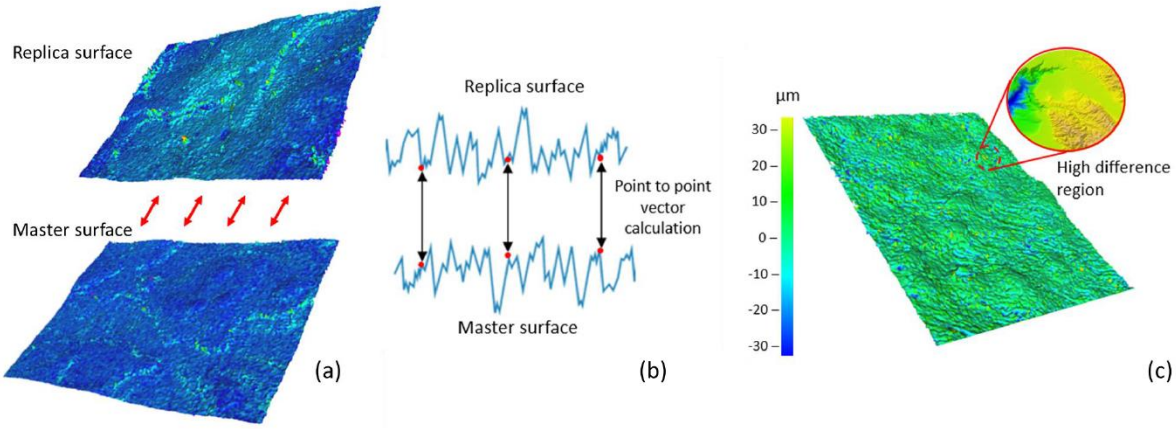

Figure 5.5 – Topography dataset point-to-point comparison. (a) Initially the topography datasets are aligned to ensure correct data point comparison. Two-dimensional representation of the difference measurement direction vector generation between two data points, allowing for heigh displacement calculation. (c) Heat map visualisation of the height difference calculation between the topography datasets, this gives a visual indication of the similarity of the scanned areas.

5.4 Replication results and discussion

5.4.1 Numerically generated surface to 3D printed topography

An initial investigation was required to quantify the quality of replication between the designed surface dataset and the 3D printed surfaces to be used in the subsequent fabrication steps. This study was essential to analyse the inevitable difference between the numerically generated topography design and the 3D printed surface. This difference must be analysed to compensate for the variability between the generated topographies and the 3D prints. If there are differences between the designed and printed surface, then the

numerical design can be adapted to compensate for the 3D print. This is particularly important if a very particular roughness or topography is required.

For this work, the three distinct topographies previously described are considered (*Sq*: 25, 50 & 100 µm). For this work it was not critical to be able replicate the designed topography exactly as it obvious there would always be some disparity between the design and 3D print. The work mainly focussed on the replication from 3D print to polymer replica quality. However, it was still important to analyse the difference from design to 3D print and have an awareness of this for future work and design considerations.

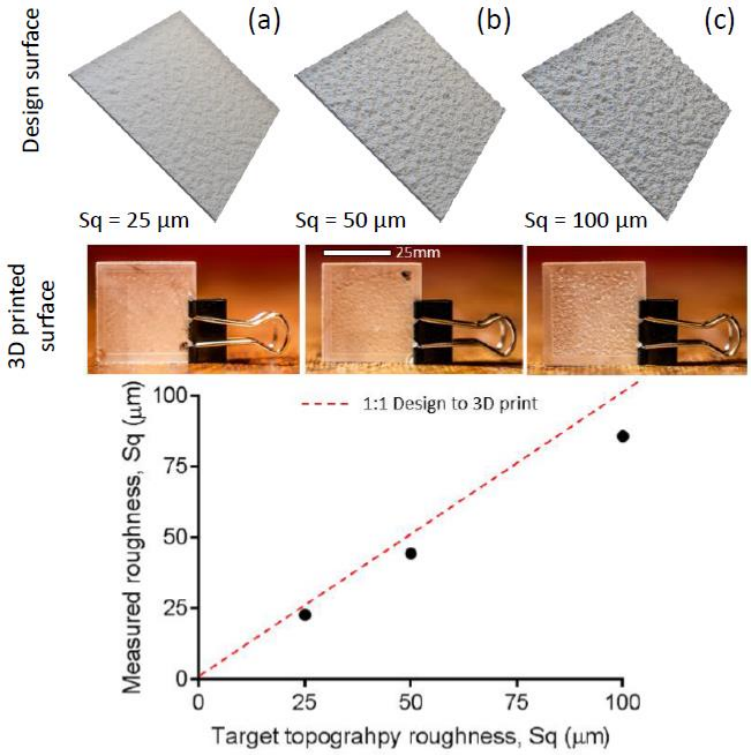

Figure 5.6 – Plot indicating the difference between the target surface roughness, Sq, of the designed topographies and the measured roughness of the 3D printed samples. The photographs illustrate the 3D printed topographies, (a) 25µm, (b) 50µm, (c) 100µm. The measured values are taken from the average of five printed samples for each topography design.

Fig. 5.6. Illustrates the *Sq* values that were measured from stitched optical scans of the whole 3D printed surfaces. This data was plotted against the corresponding design *Sq* values of the numerically generated topographies. The full numerical data is shown in Table 5.1.

Table 5.1 – The measured roughness, Sq, of the 3D printed topographies compared with the numerical designs.

Design roughness, *Sq* (μm)	*3D printed Sq* (μm)	S.D. (μm)	% Difference
25	22.72	0.21	9.1
50	44.35	0.43	11.3
100	85.68	0.57	14.3

The decision was made to measure the whole surface topographies of the 3D prints using stitched scans. This gave a more complete analysis of the difference between the numerical surface designs and the 3D printed surfaces. The data shown in Fig. 5.6 and Table 5.1 indicate that there will always be a slightly lower roughness produced in the 3D prints than the numerically generated surface designs. This % difference can be seen to increase from 9.1% in the 25 μm case to 14.3% in the 100 μm case. The difference exhibited in all the surface designs is partly due to the resolution limit of the printer. The printer used in this work is of high quality and industrial standard. There are printers with higher resolution available, but these come at significant initial cost to the user. As 3D printing technology evolves, the translation fidelity of numerical design to 3D print will inevitably be increased further.

It is hypothesised that the increase in difference associated with the higher surface roughness designs is due to the increased slope of the topographies. The rougher surface designs will inherently be made up of asperities that have steeper slopes. Effectively, these asperities can be thought of as high aspect ratio microstructures. It is widely accepted that high aspect ratio microfeatures are difficult to print and prone to collapse or decreased feature fidelity [176-178]. It is possible to achieve high aspect micro and even nanostructures, but it requires extremely high-resolution equipment and significant process optimisation to effectively print the desired structures. It would be possible to increase the design to print translation, but this would require significant investment into high quality industrial printers or design of bespoke printers and processes [179].

The work in this subsection highlights the key design considerations when 3D printing rough surface topographies using the tools presented in this chapter. When designing for a specific topography, the resolution limits of the 3D printer must be considered accordingly. With experience, it is possible to compensate at the surface design stage for the variation introduced by the 3D printing stage. For instance, should we require a specific high roughness, then the numerical design can be compensated and overengineered to achieve the desired qualities. However, this design to print translation will vary across 3D printing equipment so similar design studies specific to the equipment should be executed accordingly by the user.

5.4.2 Rough surface replication quality

This section conveys the results from the surface replication study for the two replication methods: injection moulding and polymer casting. The replication quality was analysed using the cross-correlation analyses and the mean surface difference approach, outlined in Section 5.3. The results from the cross-correlation method are shown in Fig. 5.7, while the results from the difference measurement method are given in Fig. 5.8. The numerical results from the two methods are given in Table 5.2.

The graphical figures show the data taken from both replication methods and for all three rough surface topography designs (*Sq*: 25, 50 & 100 μm). This allowed the injection moulded PS sample replication to be compared with the polymer casting of the three polymer resins: epoxy, PDMS, and ultra-low viscosity PVS.

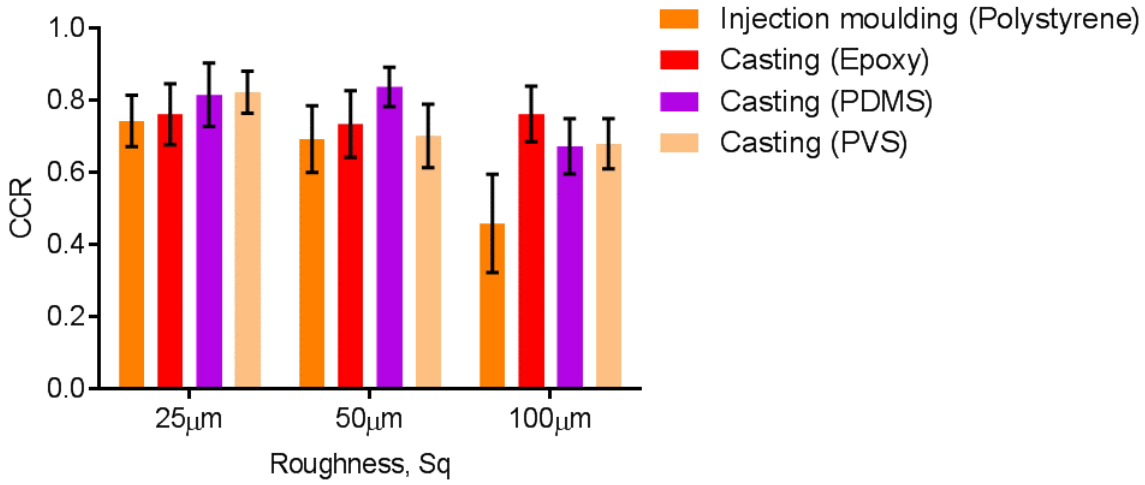

Figure 5.7 – Cross-correlation ratio analysis of the polymer replica surfaces produced from the 3D printed masters. All three distinct rough surface topographies are indicated. The results illustrated show the injection moulded (polystyrene) and the polymer casting methods (ultra-low viscosity epoxy, PDMS, ultra-low viscosity PVS). Each result is the average from 12 sample scans.

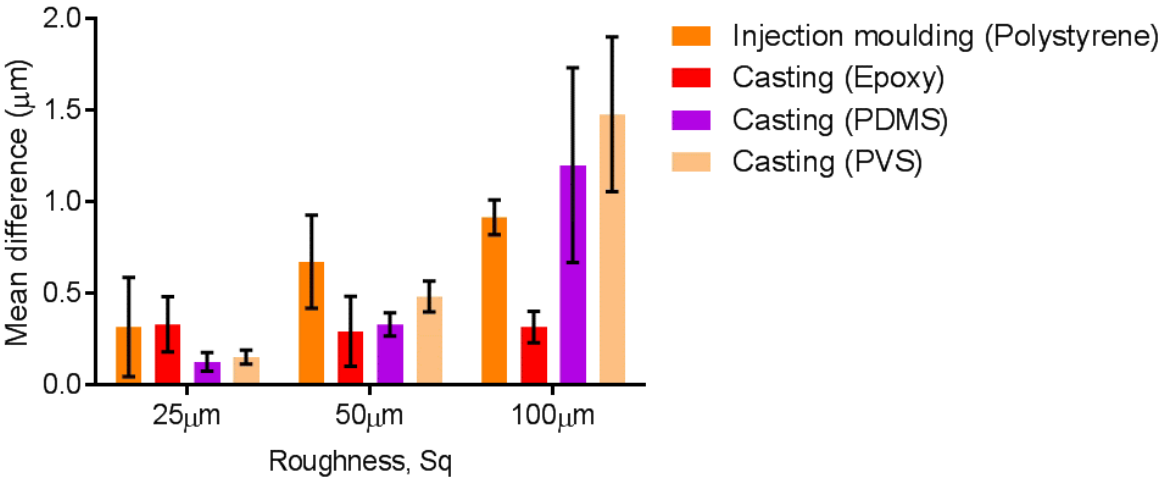

Figure 5.8 – Mean surface difference analysis of the polymer replica surfaces produced from the 3D printed masters. All three distinct rough surface topographies are indicated. The results illustrated show the injection moulded (polystyrene) and the polymer casting methods (ultra-low viscosity epoxy, PDMS, ultra-low viscosity PVS). Each result is the average from 12 sample scans.

Generally, the replication quality from the 25 μm was high. The recorded CCR values ranged from 0.74 in the PS injection moulding to 0.82 for the ultra-low viscosity PVS for this design. The results from the polymer casting were consistent for all materials, each material recorded high quality replication for the 25 μm surface. The high CCR values indicate good quality replication. The mean difference measurements seen in Fig. 5.8 support this conclusion. The low values (especially for Sq = 25 and 50 μm) indicate a high level of similarity between the 3D printed master and the polymer replica surface.

Numerical results of the CCR and difference measurement analysis are presented in Table 5.2.

It can be seen from the CCR analysis in Fig. 5.7, that as the surface roughness of the design being replicated increases, the replication quality decreases. This is supported by the increasing values measured from the mean difference analysis in Fig. 5.8. It is generally accepted that increasing roughness leads to an increase in surface complexity. The average slope and aspect ratio of the surface features or asperities will also be larger for rougher surfaces. With increased complexity and higher aspect ratio features comes an increased difficulty for the replication material to properly fill the 3D printed master topography. This inevitably leads to a decrease in replication quality as the micro and nano features of the surface become partially filled in the replication process. This can be seen in various studies, where an increase in surface complexity leads to increase in replication difficulties and reduction in the quality of replication quality [149, 163, 164]. These examples are based in biomimetic design and show how increased natural complexity of a topography can lead to difficulties in replication quality in polymers.

The results for the 50 μm topography show a marginal decrease in the replication quality. This can be seen in the slight decrease in CCR analysis and an increased measured mean difference. However, replication quality remains high across all materials and processes. This is promising as the topography complexity increases significantly from the 25 μm to the 50 μm design. It Indicates that the replication process can still be used effectively for complex rough surface topographies. However, we see a significant drop in replication quality for the replication of the 100 μm design. Especially with the injection moulding where the CCR value drops as low as 0.46. We can also see a drop in the casting method for both the PDMS and PVS. The ultra-low viscosity epoxy resin exhibits the most consistency across the topography designs. The results indicate that resins with extremely low resin viscosities will yield the best replication quality when highly complex rough surface designs are considered. The low viscosity will inevitably allow the polymer resin to flow into the micro and nanofeatures more easily allowing an increase in the replication capabilities. The effect of viscosity on replication quality is explored in more detail in Section 5.4.5.

Table 5.2 – Numerical results from the replication analysis studies. Both cross-correlation (CCR) and mean surface (µm) analysis results are shown. These results are taken from measurements between the polymer replicas and 3D printed masters. The results show analysis of all materials and both injection moulding and polymer casting methods.

	Cross-correlation ratio (CCR)			Mean Difference Measurement (µm)		
	Sq 25 µm	*Sq* 50 µm	*Sq* 100 µm	*Sq* 25 µm	*Sq* 50 µm	Sq 100 µm
Injection Moulding (Polystyrene)	0.74 ± 0.07	0.69 ± 0.09	0.46 ± 0.14	0.32 ± 0.27	0.67 ± 0.43	0.91 ± 0.09
Casting (Epoxy, (ultra-low viscosity)	0.76 ± 0.09	0.74 ± 0.09	0.76 ± 0.08	0.33 ± 0.15	0.3 ± 0.19	0.32 ± 0.09
Casting (PVS, ultra-low viscosity)	0.82 ± 0.06	0.70 ± 0.09	0.68 ± 0.07	0.15 ± 0.04	0.48 ± 0.08	1.48 ± 0.42
Casting (PDMS)	0.82 ± 0.9	0.84 ± 0.06	0.67 ± 0.08	0.13 ± 0.05	0.33 ± 0.06	1.2 ± 0.53

The injection moulding results for the CCR and difference measurement results were disappointing for the 100 µm case as it indicates reduced quality replication when considering the complex 100 µm design. It is believed that the reduced replication quality is due to a lack of optimisation of the moulding cycle when considering the 100 µm design. The parameters used for all injection moulding replication studies carried out were the same used by Convery et al [140]. It was believed that the same parameters could be transferred as these were developed to produce high-quality complex microfluidic components. This indicates how important it is to optimise the injection moulding cycle for specific designs, especially more complex rough surfaces. As previously discussed, there are many variables associated with the injection moulding process and therefore many areas for a decrease in production quality to occur. All the key parameters have direct influence over production quality and must be considered independently for the task at hand. A full optimisation study was not carried out for the 100 µm and therefore the quality of replication suffered in this case. Non-optimum parameters can result in incomplete mould filling, material stretching, and part distortion – all causing a reduction in replication quality. It is recommended that, for complex rough surface topographies above 50 µm, a thorough moulding optimisation should be considered to ensure adequate replication. It has previously been shown that high quality micro and nano designs can be effectively injection moulded to high standards. Therefore, it should be possible to achieve high quality replicas of the structures in the 100 µm design [81-97].

5.4.3 Injection moulding 3D printed inlay durability

Injection mould inlay durability is critical to producing high quality parts from the manufacturing process. Inlay durability is also important for the economic viability of the process, especially in cases of mass production. Typically, the inlays are expensive to manufacture and are expected to enable the production of 1000s of components. However, for this work, the process is only required to perform effectively for relatively short rapid prototyping runs or research sample production. The moulding cycle itself imparts harsh conditions on the inlay. The high temperatures and stresses involved require the mould inlay material and design to be particularly durable. To test inlay durability, parts will be taken at key points in the moulding cycle: Part No. 50, 100, 250, 500, 1000 for example. These components are then inspected to ensure they adhere to the manufacturer's expectations and guidelines.

The process developed here was assessed using relatively short moulding runs. These were kept to a maximum of 200 parts. Part No. 50, 100, 150, and 200 in the component sequence were examined to ensure replication quality was consistent across the moulding cycle and the 3D printed inlay had not been damaged. This was felt adequate as it would be rare that more than 200 replicas of the rough surface topography would be required. If more components were needed, then a new inlay can be quickly 3D printed and production resumed. Convery et al. [140] demonstrated that up to 500 microfluidic parts can be produced using a single 3D printed inlay without suffering significant part deterioration or inlay damage. The micro-channels associated with the designs were well within acceptable error margins even at component No. 500. The process outlined in this chapter uses inlays 3D printed using the same process, similar moulding conditions, and injected material. The results from the CCR and mean surface difference analysis are shown in Fig. 5.9, with full numerical results detailed in Table 5.3.

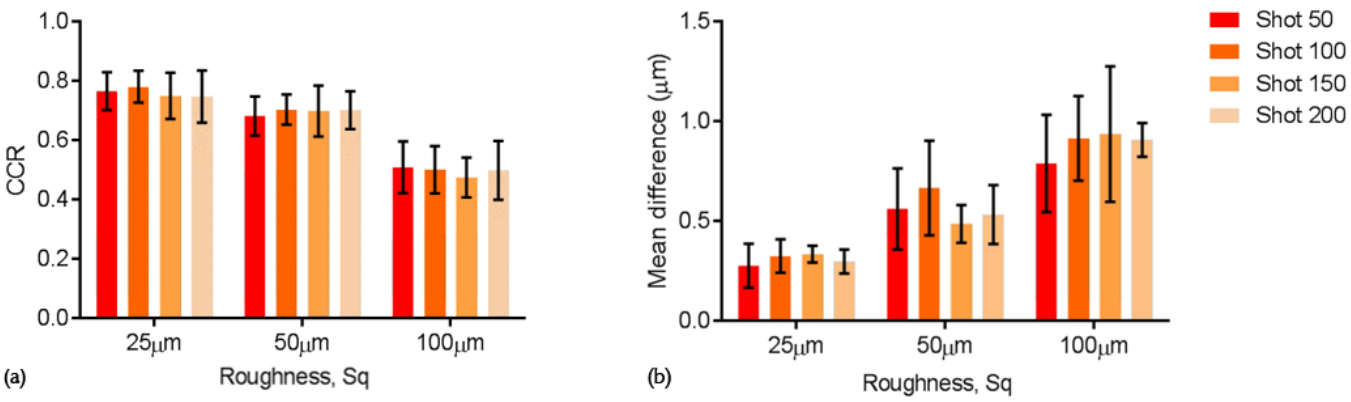

Figure 5.9 – Injection moulding inlay durability results: (a) Cross-correlation (CCR) for injection moulded PS replica surfaces from 3D printed master and (b) Mean difference measurement for injection moulded PS surfaces from 3D printed master. Results shown for shots 50, 100, 150, and 200. Consistency across the results illustrate the 3D printed inlay durability and repeatability for the process. Durability results are shown for the three distinct rough surface designs.

Table 5.3 – Injection moulding inlay durability data indicating results for cross-correlation ratio (CCR) and mean difference between injection moulded (PS) replica surfaces and 3D printed master for mould shots 10, 20 and 30. The consistency across the shot numbers highlights good inlay durability.

	CCR			Difference Measurement (μm)		
	Sq 25 μm	*Sq* 50 μm	*Sq* 100 μm	*Sq* 25 μm	*Sq* 50 μm	*Sq* 100 μm
Shot 50	0.77 ± 0.06	0.68 ± 0.07	0.51 ± 0.9	0.28 ± 0.11	0.56 ± 0.2	0.79 ± 0.24
Shot 100	0.78 ± 0.05	0.7 ± 0.05	0.5 ± 0.1	0.28 ± 0.23	0.66 ± 0.24	0.91 ± 0.21
Shot 150	0.75 ± 0.08	0.7 ± 0.09	0.47 ± 0.07	0.34 ± 0.04	0.49 ± 0.09	0.94 ± 0.2
Shot 200	0.75 ± 0.9	0.7 ± 0.06	0.49 ± 0.1	0.3 ± 0.06	0.53 ± 0.15	0.91 ± 0.08

The data in Fig. 5.9 and Table 5.3 show very consistent results across Parts 50, 100, 150, and 200. This indicates a high repeatability as well as suitable durability of the 3D printed inlay for rapid prototyping and research sample production. Fig. 5.9(a) shows the cross-correlation ratio analysis for the injection moulding study, while Fig. 5.9(b) shows equivalent mean difference values. The low standard deviation and consistent values for both analysis methods indicate minimal damage was sustained by the inlay. This is important if injection moulding is to be used to produce high-quality replicas for surface engineering research or

applied scientific environments. This study indicates the suitability of injection moulding as a consistent and reliable method to produce rough surface polymer samples.

5.4.4 Rough surface tailoring

The generated surfaces used in the previous studies described in this chapter were kept to consistent rough surface parameters, particularly the PSD characteristics of the surfaces. The main variable explored in the replication studies was the areal roughness, *Sq*. However, if we consider key PSD parameters used to generate the rough surface designs, then we can design the topographies to hold certain characteristics. This can enable a tuned topography, with a specific style of roughness to be generated. The tailoring aspect of this fabrication tool is appealing as it allows users to design topographies specific to their uses or research question. This section examines the tool's capability to manipulate the designed topography and produce a 3D printed surface from the numerical design.

The ability of the tool to reproduce topographies with manipulated asperity frequency and wavelength is explored. By altering the upper and lower frequencies (f_l and f_s) used to define the PSD of the surface, we can influence the shape of the designed topography. These frequencies bound the range of asperities that make up a topography and therefore have a direct influence on the nature of surface and how it interacts with its environment [173]. Four distinct topographies were designed to illustrate the ability of the fabrication tool to tailor the designed numerical surfaces. The upper and lower frequency bounds that define the nature of the surface were varied to alter the shape of the surface. Fig. 5.10 shows the numerically generated surfaces (top) along with optical scans of the full 3D printed surfaces (bottom). The surfaces were designed to show a range of long wavelength, low frequency asperities, Fig. 5.10(a), to short wavelength, high frequency asperities, Fig. 5.10(d). The areal roughness, *Sq*, and the Hurst exponent are kept constant. The frequency range used within the designs increases as we move from Fig. 5.10(a) to Fig. 5.10(d). Full numerical data of the designed surfaces and the resultant scanned 3D printed surfaces are given in Table 5.4.

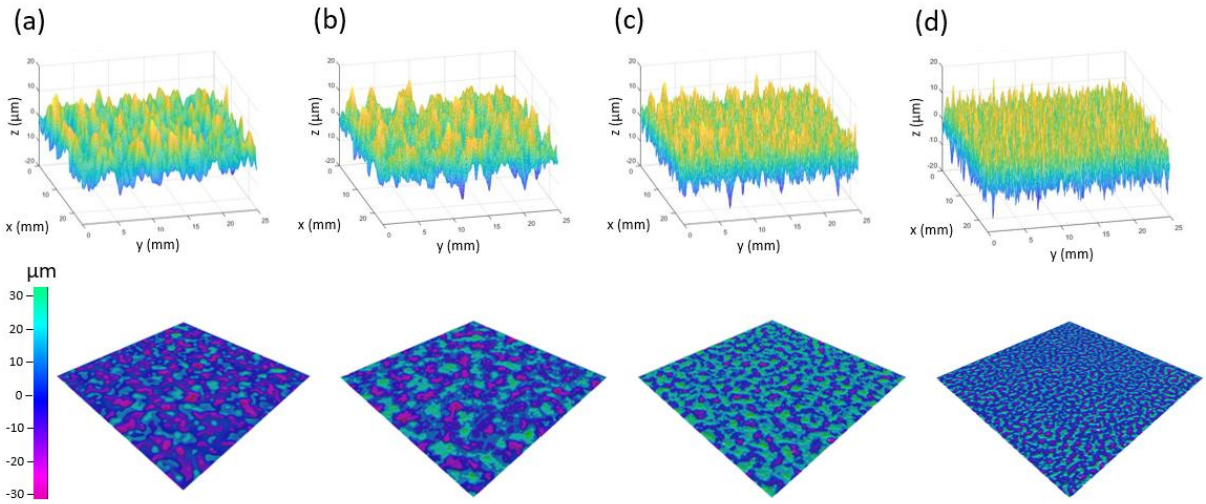

Figure 5.10 - Surface tailoring results indicating the ability to fabricate surfaces with varying frequency characteristics. Figure shows the generated topographies (top) and the as-produced 3D printed surfaces (bottom). The frequency cut-off bands are varied from left to right with upper and lower frequency cut-offs (and frequency range) increasing from left to right according to [fl, fs] (Units of 1/mm). Full numerical details in table 5.4.

Table 5.4 – Numerical parameters used to design the generated surfaces and results of scanned 3D printed topographies. The surface data here corresponds to the surface designs and 3D print scans shown in Fig. 5.10. Hurst exponent = 0.7 for all cases.

Surface instance based on frequency bounds	Lower cut-off frequency, f_l (1/mm)	Upper cut-off frequency, f_s (1/mm)	Generated roughness, *Sq* (µm)	3D Printed roughness, *Sq* (µm)	3D printed gradient, *Sdq*	3D Printed autocorrelation length, *Sal* (µm)
(a)	5	32	25	23.38	0.27	755.2
(b)	5	64	25	23.36	0.29	780.7
(c)	10	128	25	22.49	0.35	490.3
(d)	20	256	25	22.97	0.37	253.9

The numerically generated designs and scanned surfaces clearly show very different topographical nature and features. The amplitude of the design's respective areal roughness, *Sq*, is kept constant. The design and 3D print in Fig. 5.10(a) show a very long wavelength roughness, with widely distributed asperities. This corresponds to the numerical parameters where the frequency range was kept short and to low frequencies, 5-32 (1/mm). While the topography in Fig. 5.10(d) shows a surface with lots of tightly spaced high frequency asperities, this is defined by a larger frequency range that allows for much higher frequency features, 20-256 (1/mm). Fig. 5.10 and Table 5.4 clearly show that the 3D print translation

has captured the changes in numerically defined features very well. We see a good comparison of areal roughness and the frequency changes of the numerical designs in the printed surfaces. The manipulation of the frequencies can be seen in the quantitative results in Table 5.4, shown by an increase in the surface gradient, *Sdq*, and decrease of auto correlation, *Sal*, values recorded from 3D print scans. The surface gradient measures the slope of the asperities that make up the printed surface; therefore, it is expected that higher frequency asperities will result in an increase in *Sdq*. The auto correlation measurement is an indicator of characteristic wavelength of the surface topography and should decrease as the we introduce more regular higher frequency asperities. This study has shown that through manipulation of the surface parameters at the numerical design stage, we can realise 3D printed surfaces that have desired characteristics. This indicates that certain parameters can be kept constant while manipulating others for investigation depending on the research environment, highlighting the fabrication tools versatility and transferable use.

5.4.5 The effect of polymer resin viscosity in surface replication quality

This section details an investigation into the role of viscosity in surface replication. In Section 5.4.2 the role of polymer resin viscosity in surface replication was briefly mentioned. However, the work in that section only briefly discussed the difference between the three polymer resins used. The results showed how the vastly reduced viscosity of the epoxy resin allowed for consistently high-quality replication, even in the 100 μm design. However, there are potentially other variables at play when considering three dissimilar materials. Curing times and casting methods are slightly different depending on the material. This introduces multiple variables that could influence replication quality. The study here isolated the material used and kept the casting process the same during the investigation.

The proprietary PVS resins (President, Coltene Whaledent, Altstätten, Switzerland) were selected for this investigation. The company offers four types of PVS resin that are very similar but have increasing levels of viscosity – making the material ideal for this work. The supplier designates the PVS resins as follows: ultra-low viscosity, low viscosity, standard viscosity, and heavy viscosity. Viscosity measurements of each resin were executed to

characterise the materials due to the lack of sufficient detail in the manufacturer's datasheet.

Viscosity measurements of the PVS resins were performed next. The measurements were performed using the modular compact rheometer (MCR 302, Anton Paar, Austria), using the following two geometries: parallel plates 50 mm diameter and cone & plate 50 mm diameter with 1° slope. The curing of the resins was tracked by measuring the time dependent behaviour of the viscoelastic moduli. All tests were performed keeping the following parameters constant: temperature of 22°C, frequency of oscillation of 20 Hz, and a strain amplitude of 20% for the materials. Three samples were measured for each resin.

The viscosity dependent replication study was carried out using only one surface design to minimise variables being considered. The Sq = 25µm was used as this provides the simplest replication. The PVS resins were cast using the slightly modified method outlined in Section 5.2.6. Optical scans of the 3D printed surface and PVS replicas were taken using the same scanning protocol and equipment described previously in this chapter. The cross-correlation ratio (CCR) and surface mean difference analysis methods were used to access the replication quality. Fig. 5.11 and Table 5.5 detail the results from the investigation.

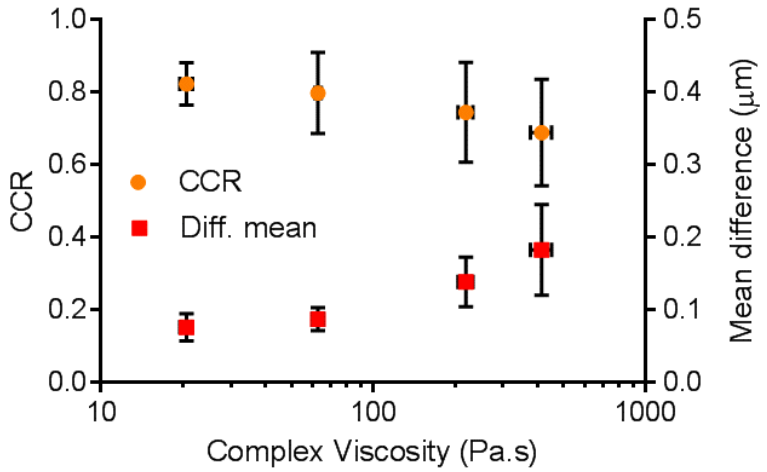

Figure 5.11 – Results of the effect of viscosity on surface replication quality. PVS resins used for the polymer casting. Left y-axis details cross-correlation ratio results, right y-axis details surface mean difference. Both analysis methods are plotted against the complex viscosity of the resins. Results measured from 3 samples for each case.

Table 5.5 – Numerical results from viscosity investigation. PVS replication from 3D printed master data. Both cross-corelation ratio (CCR) and mean difference measurement are shown.

	Complex viscosity (Pa.s)	Cross-correlation ratio (CCR)	Mean difference measurement (μm)
PVS (ultra-low viscosity)	20.60 ± 1.12	0.82 ± 0.06	0.15 ± 0.04
PVS (low viscosity)	62.64 ± 1.68	0.79 ± 0.11	0.17 ± 0.03
PVS (standard viscosity)	218.6 ± 13.67	0.74 ± 0.14	0.28 ± 0.07
PVS (high viscosity)	414.7 ± 36.93	0.69 ± 0.15	0.36 ± 0.13

The results shown in Fig. 5.11 and Table 5.5 show that there is a strong dependency between the viscosity of the polymer resin and their viability for high-quality surface replication. Both analysis methods indicate a drop in replication quality as the complex viscosity increases. This is shown by the CCR ratio dropping as the viscosity of the resin increases, while the surface mean difference measurement increases. The CCR measurement drops from 0.82 for the ultra-low viscosity PVS to 0.69 for the high viscosity resin. The main reason for this reduced surface replication quality is likely the reduced flowability of the more viscous resins. The increased complex viscosity results in the material behaving 'stiffer' when in a resin form. This results in difficulty filling the microcavities of the rough surface topographies. It is reasonable to conclude from this study that the lowest viscosity resins of the desired material should be used where possible to achieve the best replication quality from the rough surface topographies.

5.5 Applications for advanced tailored rough surfaces

This chapter has outlined two advanced fabrication routes that enable the production of numerically designed rough surface topographies. Both begin with the 3D printed rough surfaces and allow replication via the injection moulding and polymer casting methods. The fabrication routes key benefit is the user defined topographies that can be easily tuned to suit the research purpose. Other advantages include ease of operation, short fabrication time, and range of available materials. This makes the tools presented here highly versatile

and applicable to various engineering requirements. This section highlights just some of the research areas that could benefit from the fabrication process.

Rough surface topographies and interfaces are ubiquitous in engineering and scientific design. Many surface processes and phenomena are influenced by the topographies within an engineering system. Experimental investigation into these systems is the clearest example of the fabrication routes use. The original use for the fabrication route was for investigation into tribological processes. Critical areas include research on friction [180], adhesion [181], contact stiffness [182], lubrication [183, 184] and sealing effectiveness [185]. These are all sensitive to roughness and could benefit from the ability to design and fabricate rough surfaces for investigation. This can even be extended to material failure where surface roughness has been shown to have a critical role in crack propagation and fracture behaviour [186].

However, the design and fabrication of rough surfaces also has scope to be applied to a wider research community. Fluid dynamists often consider the role of surface roughness in flow regimes, generation of turbulent boundary layers, and aerodynamic drag [187]. In biological systems, adhesion mechanisms are often investigated [188]. The ability to replicate and design the rough surfaces can aid in understanding the mechanisms involved that improve or negate adhesion in certain biological instances. Surface topography has a crucial role in biological growth, with surface roughness shown to have a strong influence on algae growth [189]. The team investigating algae growth reverse engineered rough topographies for 3D printing via optically scanned rock surfaces. These were then used as experimental samples for investigation. Similar work has been carried out to explore biofouling in water treatment systems and the protection of key system components [190-192]. These works could all potentially benefit from having the resources to design and fabricate surfaces to investigate key experimental parameters. This would allow a more advanced level of control to the respective research investigations. Haptic and tactile studies have even been explored in relation to rough surfaces. Sahli et al [193] 3D printed an array of polymer surfaces exhibiting various micro-structures and surface parameters.

Human participants were encouraged to touch the surfaces to see if they could distinguish the differences in the surfaces. The fabrication tool could again be of benefit here.

One final popular area of research where the fabrication tool could be used is triboelectric nanogenerators (TENG). Electrical output has already been shown to be sensitive to surface topography and roughness of the contacting surfaces within a TENG device [194-196]. The tool developed in this chapter has already supported investigations into triboelectric research: it has been applied to fabricate surfaces for a study on the effect of surface roughness on the electrical output of TENGs [197].

These examples show there are a wide range of possibilities for the tool to be implemented in future projects. Basic 3D printing of rough surfaces has been shown in a limited number of examples. However, the key benefit of this work is the ability to design and fabricate custom and tailored rough surfaces to suit the research area. In addition, the fabrication routes support rapid replication in a wide range of materials for rough surface design.

5.6 Conclusion

This chapter has explored and developed an approach for the rapid replication of numerically designed rough surface topographies. The surfaces were designed using user defined characteristics before being 3D printed. The 3D printed surfaces can then be used as a master surface for the replication routes outlined: injection moulding and polymer casting. The replication quality for both methods was analysed using both a cross correlation analysis and a surface mean difference method.

The results show high quality design to 3D print translation along with high quality replication using both injection moulding and polymer casting based on the high value of the CCR measurements. Indicating a high level of surface profile similarity and therefore replication. The best results were achieved when replicating the Sq = 25 μm surface. This was the simplest design, so allows for the best replication. The replication quality decreased slightly for all materials and methods as the surface roughness and topography complexity increased – most likely influenced by the increased slopes and aspect ratios of the surface features. This is to be expected but can be improved through process optimisation. This

was a particular problem for the injection moulding of the 100 μm surface. As discussed in Section 5.4.3 this can likely be improved through surface-specific process optimisation.

The influence of polymer resin viscosity was also investigated, showing that best surface replication is achieved using low viscosity resins. This chapter also gave examples of surface tailoring, through manipulating key surface parameters. The ability of the numerically tuned surfaces to be realised in high quality 3D printed master surfaces was also demonstrated. This is one of the key novel aspects of the work. Allowing users to design and fabricate surfaces to suit their research needs. Injection mould durability was explored and yielded beneficial results. The mould inlays were able to easily produce at least 200 samples without suffering damage or deterioration of surface replication quality. As outlined, the main applications lie in research environments where the ability to rapidly produce rough tailored rough surface topographies is particularly beneficial. The versatile flexible approach can allow users to investigate the influence of rough surfaces over a host of surface engineering fields and phenomena. The tool has already been deployed in a study on the effect of surface roughness on the electrical output of triboelectric nanogenerators.

Further investigation is required into parameters that can provide a measure of the surface replication quality. Cross correlation ratio and the difference measurement give a good measure but not the full picture for the quality of surface replication. Surface parameters such as areal roughness, asperity slopes, surface kurtosis, surface correlation length are all examples of tribology parameters that could be assessed to provide a more complete analysis of the surface replication across the methods used in this work. These parameters should be analysed for the 3D prints and all polymer replication samples in future applications to provide a more convincing argument for the effectiveness of rough surface rapid replication method.

Chapter 6

Application of rough surface fabrication tool to the study of rough surface contact stiffness

6.1 Introduction

This chapter explores the influence of surface roughness on normal contact stiffness and the evolution of real contact area of interfaces during normal loading. Normal contact stiffness is known to be greatly influenced by an interface's topography. The topographical features or asperities present at an interface introduce a compliance that controls the approach of the two surfaces when under loading. As described in Chapter 4, normal contact stiffness is mathematically defined as the rate of change of normal load, *P*, with the relative approach, *d*, of two surfaces in contact ($K_n = |dP/dd|$). This stiffness is largely influenced by the material properties of the surfaces in contact and the geometry of the interface region.

Contact stiffness as previously discussed has great influence on mechanical design of engineering systems. Areas of contact all introduce a compliance based on the topographical features. This interfacial behaviour influences the mechanical behaviour of an engineering design due to the large number of interfacial interactions present in a complex mechanical system [199, 200]. In Chapter 4, the benefits of microstructured interfaces were explored. There, we saw how micro-structuring an interface we can achieve repeatable and tailored normal contact stiffness. This means the mechanical behaviour can be controlled and designed to suit a particular situation. However, most engineering systems contain a myriad of interfaces that result from components in contact that have been machined by conventional methods. Most conventional engineering components in a mechanical system will have an inherent surface roughness due to their manufacturing method, whether by

CNC milling, die casting, compression moulding etc. [201, 202]. This results in rough surface interactions being ubiquitous in interfacial interactions. These rough surface contact interfaces within a system introduce a compliance controlled by the topographical features. The rough surface interactions introduce far more complex mechanical behaviour than that associated with a structured interface. By extension, the interface becomes more difficult to design in order to control specific parameters (such as the contact stiffness).

However, we can gain a greater understanding of these rough surface interactions through mechanical modelling and experimentation. Improved understanding of rough surface interaction would allow for more efficient and controlled mechanical design through the ability to design and estimate the rough surface behaviours and interactions throughout a mechanical system. In this study, we develop four rough surface designs in the same material each having different topographical features and surface roughness. The design and manufacture follow the injection moulding fabrication procedure detailed in Chapter 5. The manufacturing method is shown in Fig. 6.1. The designs are developed and then 3D printed to be utilised as an injection moulding inlay. By exploiting this fabrication procedure, it is possible to design and produce high quality replicas using injection moulding that have a high degree of similarity between samples of the same topography This procedure is applied to the four rough surface designs for investigation.

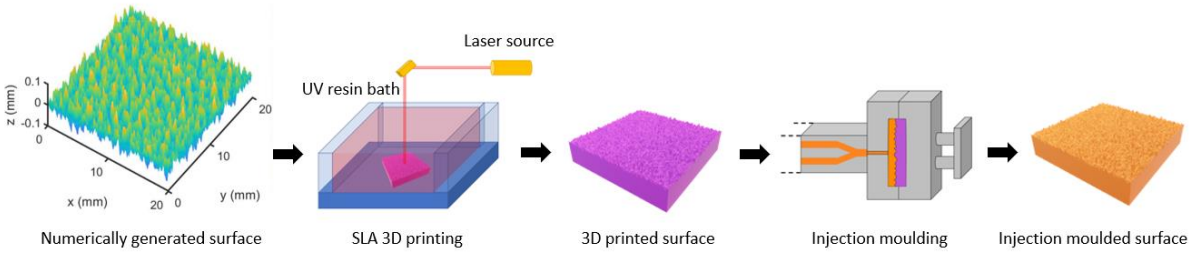

Figure 6.1 – Rough surface fabrication process used to produce the rough surface polymer designs.

The work begins with the mechanical testing of the rough surface polymer interfaces using two different methods. The first method aims to explore the normal contact stiffness behaviour of the rough surface interfaces, while the second allows for the measurement of the evolution of real contact area present during the normal loading of the rough surfaces. The results are then compared with FE models that aim to simulate the mechanical

experiment. The two branches of this project aim to develop a more holistic understanding of the influence of the rough surface topography on the mechanical behaviour of interfaces.

6.2 Experimental methodology

Two mechanical test methodologies were developed and utilised to explore both normal contact stiffness and real contact area for the rough surface designs. The normal contact stiffness test methodology was adapted from the protocol and rig developed for the microstructured contact tests in Chapter 4. A new optical method had to be adapted for the contact area measurements. This section details the experimentation, design and techniques used for measuring both normal contact stiffness and real contact area during the normal loading of the rough surface samples.

6.2.1 Normal contact stiffness measurements

The same test rig detailed in Chapter 4 is used for measuring the normal contact stiffness of the rough surfaces. This method provided a well-established and reliable process for measuring normal contact stiffness. The rough surface normal contact stiffness tests follow the same initial set up and methodology, but have slight modifications detailed in this section. Full details on the mechanical testing rig and the DIC optical system used for measuring normal contact stiffness are provided in Section 4.2.1.

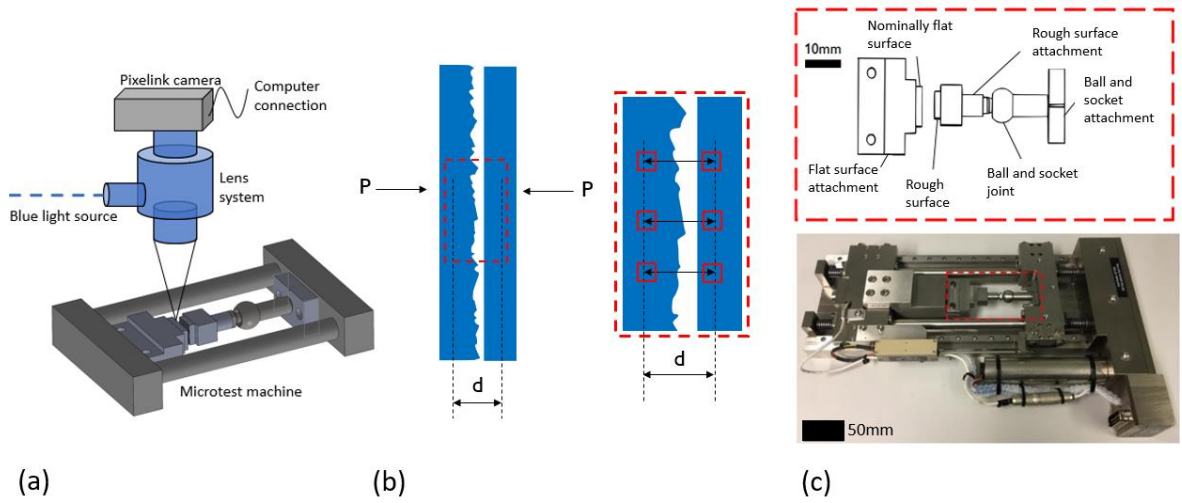

Figure 6.2 – Experiment schematic of the normal contact stiffness tests: (a) Basic representation of the experimental rig with optical observation of the contact, (b) Application of normal load, P, and relative displacement of the interface, d, (Red dashed box indicates a snapshot of how the DIC system tracks the relative approach of the samples) and (c) Detailed view of the experimental fixtures for the modified Deben microtester.

The microtest rig allows for the rough surface designs to be positioned and compressed into a nominally flat sample of the same material. The modified fixtures allow for the self-alignment of the samples to ensure full and uniform contact over the rough surface interface. The applied normal load is again measured using the microtest rig, while the relative displacement approach of the interface is measured using an optical system positioned above the test rig. DIC software is used to track the displacement of the interface. A simplified diagram of the normal contact stiffness tests is shown in Fig. 6.2. These provide an overview of the operation of the normal contact stiffness experiments.

Overall, the tests were executed using the same procedure as in Section 4.2.1. However, the loading varied in magnitude and two types of tests were executed for the rough surface samples. The initial tests were carried out to examine the evolution of normal contact stiffness of the rough surfaces in a mostly elastic regime. To do this, the tests were limited to relatively low loads before being unloaded and the test repeated. The samples were prepared and aligned before being compressed to a normal load of 500 N at a rate of 0.5 mm/min before being unloaded. During the tests, the displacements were tracked from above using DIC – the displacement tracking followed the same procedure as in Chapter 4.

The second type of test was used to examine the evolution from elastic to a plastic regime where the normal contact stiffness would saturate at a level based on the rough surface interface. The test followed the same procedure but involved loading the samples to a greater threshold. The samples were loaded to 1500 N to ensure a transition to an elastic-plastic region. Three samples for each rough surface design were tested. The samples were not repeatedly tested as they were known to undergo significant plastic deformation after each test.

6.2.2 Optical real contact area measurement

The second test executed aimed at generating a real contact visualisation during the normal contact stiffness tests. A novel setup was adapted from that developed by Kumar et al. [196]. This was developed by a colleague to enable the measurement of the real contact area of various TENG rough surface designs. This meant the test could be easily adapted to enable the measurement of the real contact area exhibited during normal contact stiffness

tests. The test rig aimed to simulate the same test conditions in the normal contact stiffness measurements. A high precision linear electrodynamic fatigue test machine (Electropuls E3000, Instron UK) was adapted by the addition of custom experimental fixtures and an optical system to enable the contact area measurements. The Instron measures the applied normal load during the tests via the loadcell fitted in the actuation drive. The setup is shown in Fig. 6.3.

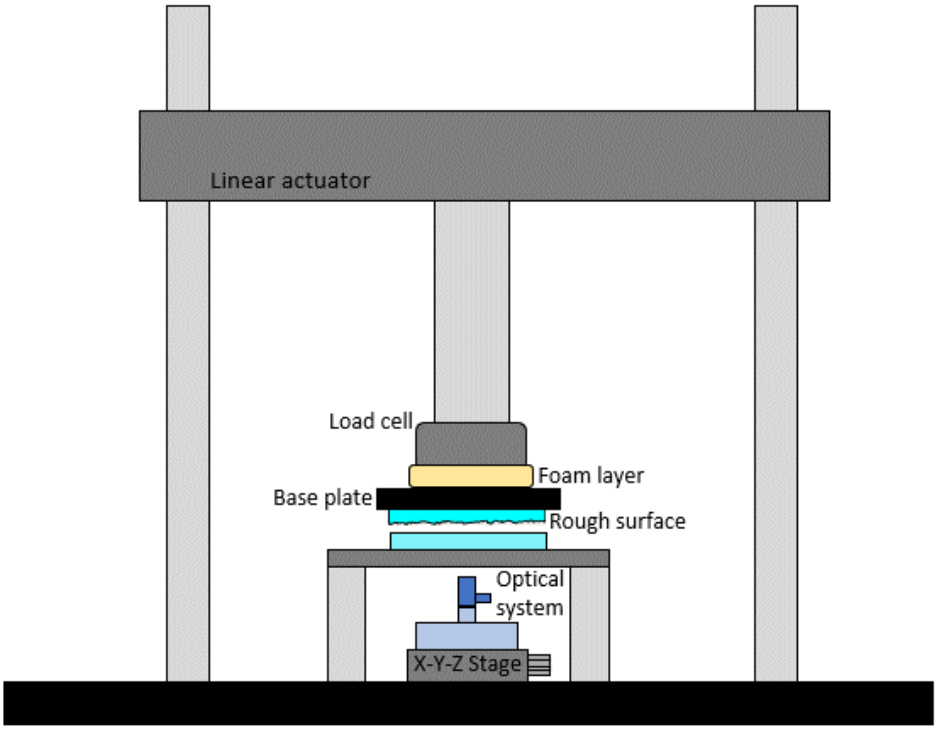

Figure 6.3 – Schematic for the test rig that allows for the optical measurement of the real contact area of the rough surface interfaces.

The rough surface designs are secured to the upper fixture which is attached to a foam layer. This feature provides a self-alignment mechanism for the base plate holding the rough surface replica, similar to the action seen in the normal contact stiffness measurements. The top fixtures are attached to the load-controlled mechanism of the Instron test machine. The rough surface samples are brought into contact with a transparent PMMA block that is secured on the lower stage. PMMA sheet was selected as this has the similar critical material properties as the injection moulded polystyrene samples. Transparent PS was unavailable so a similar thermoplastic was selected. This was only used for the contact area measurements and not the contact stiffness tests. The material properties of the samples

used measure as follows: Polystyrene has a Young's modulus of 3.1 GPa and a yield strength of 55MPa. PMMA has a Young's modulus of 3-3.4 GPa and a yield strength of 72MPA. Therefore, the contact interactions at the load levels required can be assumed to be the similar. The transparency of the PMMA allows for the optical setup positioned underneath the stage to record the real contact area measurements.

The optical measurements work by a reflection interference microscopy approach. This allows images to be recorded at the rough surface interface which show the areas of real contact [202-204]. This allows for easy distinction between areas of contact and non-contact. Fig. 6.4 details the working principles associated with the optical measurements. A telecentric lens combined with a fibre optic lighting system allows for the illumination of the area of interest. The resolution in both vertical and horizontal directions is 5.5 µm. While the field of view offered by the lens is 11.26 mm x 5.9 mm. The working distance is 40 mm, meaning the system could be easily secured underneath the fixture stage. The lens system is attached to the digital camera (PL-D732 2.2MP, Pixelink) used in the normal contact stiffness tests. The optical system sits on a Thorlabs 3D translation stage that allows adjustment to camera focus and capture area. This allows for the high level of optical focus required at the interface region for accurate real contact area image capture.

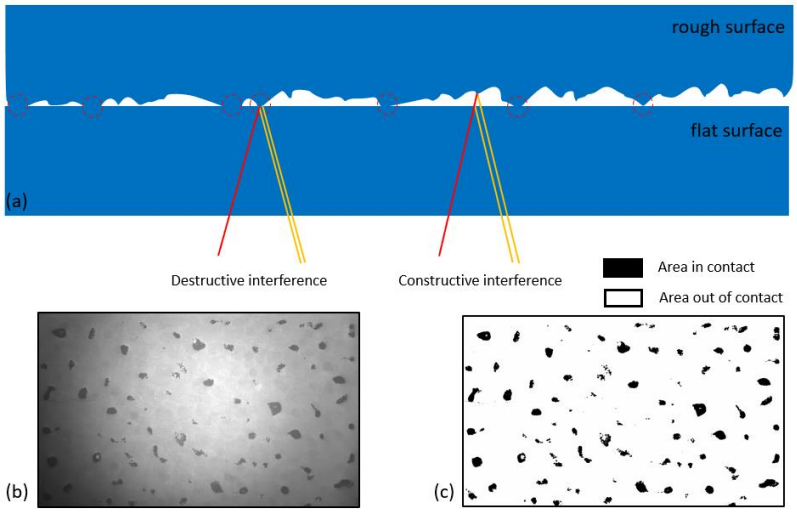

Figure 6.4 – Optical principles deployed in the optical contact measurements of real contact area: (a) White light is projected from the telecentric lens attached to the Pixelink camera through the transparent PMMA and then reflected for capture with destructive and constructive interference depending on the contact area, (b) Sample contact image that demonstrates real contact areas (dark spots) and out of contact regions (bright spots) and (c) Binary image after post-processing used to calculate real contact area.

After each loading step, the focus level must be examined to ensure adequate image quality for the post-processing analysis. The recorded real contact images were analysed using Fiji, an open-source image processor based on ImageJ2 (National Institutes of Health, USA). The Fiji tool allows for image manipulation such as thresholding, noise filtration, binary analysis.

The test methodology is relatively simple and follows a similar procedure to the normal contact stiffness tests. The rough samples are brought into contact with the nominally flat PMMA and incrementally loaded from 0 N to 500 N in 50 N steps. An optical image is taken at each 50 N step to allow for an evolution of the real contact area to be examined as the applied normal load is increased. The images can then be post-processed and analysed to evaluate the real contact area for each rough surface design at each incremental loading step. These results can then be utilised to show the evolution of real contact area with the normal contact stiffness measurements.

6.2.3 Finite element model design

Finite element models were designed to help better understand the mechanical behaviour of the rough surface interfaces during the mechanical tests. The FE models were used to compare with the experiments and help better understand the behaviour exhibited during the mechanical tests, specifically the evolution of the normal contact stiffness behaviour of the interfaces. Initially, linear elastic models were built. These were then modified to include elastic perfectly plastic behaviour to make sure any plastic behaviour of the asperities was accounted for. The plastic behaviour modelled in the initial tests was thought to be minimal due to the normal applied pressures and loads associated with the tests. The models were only used to analyse the evolution of normal contact stiffness associated with the first series of the mechanical tests. The models were all built and simulated using the FE software, ABAQUS explicit.

The model designs begin with an idealised flat-on-flat contact that measures the same area associated with the nominal sample sizes. The rough surface designs all measure 10 mm x 10 mm, while the nominally flat sample measures 10 mm x 15 mm. All material properties were taken from the data sheet of the injection moulded polystyrene (PS) (1810 Crystal Polystyrene, Total Petrochemical and Refining, Belgium). Fig. 6.5(a) shows a diagram of the

initial idealised flat contact FE models. This is a 2D representation of the model, the surface seen here has a depth of 10 mm. The 25 µm and 50 µm model designs both contained 900,000 elements. Both models were built from the original idealised flat model before the rough surface topography was mapped to the surface. The rough surface models were fixed in the y and z directions. While allowing the surface to be compressed into the idealised flat surface in the x direction. ENCASTRE boundary conditions were used on the idealised flat to keep it fully fixed in all directions. A pressure is then applied to the rough surface model to compress it against the idealised flat.

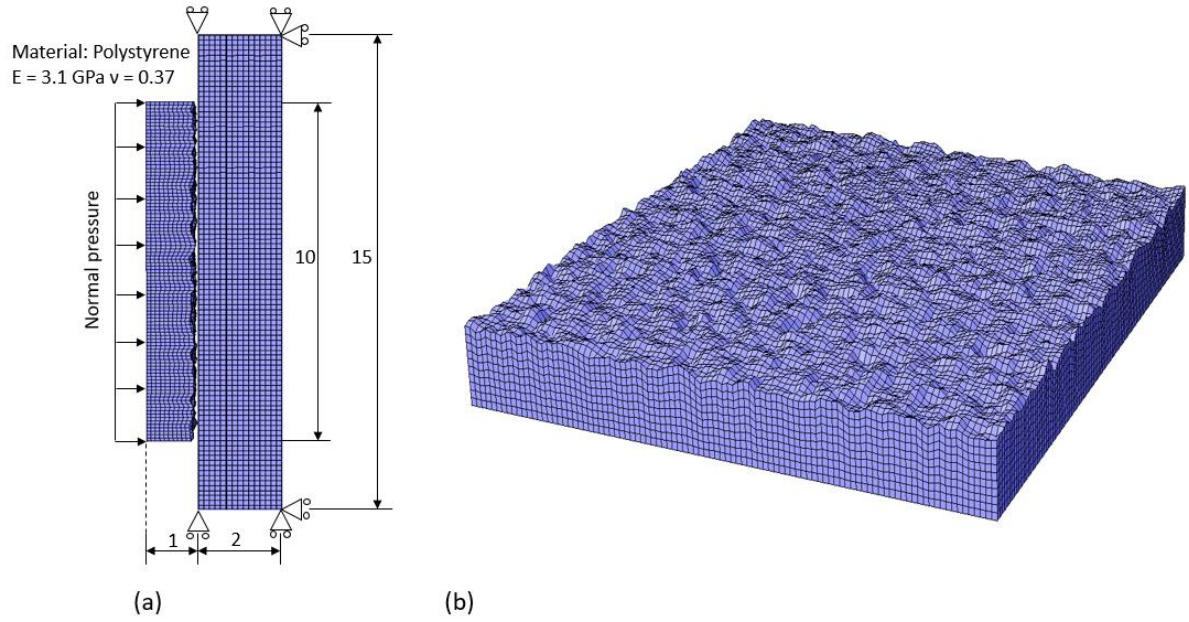

Figure 6.5 – Basic schematic for the ABAQUS model design: (a) 2D schematic cross-section of the model used in ABAQUS, view is taken from top of model. All dimensions are in mm and (b) FE model with the rough surface data mapped onto the component interface, node and element positions after they have been shifted according to the surface data scans.

Representative models of the rough surface samples can then be built from the initial idealised flat model. The rough surfaces from the samples were used to generate the rough surface FE models. This was done by capturing the rough surface topographies using optical scans of the surfaces. The surface data could then be post-processed and mapped onto the idealised flat models. This allows a representative model of the rough surface to be generated and used in the mechanical simulation. The image in Fig. 6.5(b) illustrates the rough surface representation in the FE models after the flat surface mesh has been moved according to the surface data from the optical scans. The rough surface mesh begins with a

completely flat mesh of uniform element size. The nodes of the nominal contact area are then shifted in the *z*-direction according to a linear interpolation. Each node on the flat surface is shifted according to a linear interpolation of the *z*-coordinates of the four nearest neighbouring data points in the optical scan data of the rough surface designs. This allows for the flat elements to become shifted in the z-direction to emulate the rough polymer surfaces. Each node in the elements that construct the rough surface shift in the *z*-direction but will maintain their *x*-*y* position. It is accepted that this is inevitably going to lead to a relatively inaccurate approximation of the surface as so many points are interpolated to generate the rough surface map applied to the FE model. This will inevitably 'smooth' out microfeatures of the rough surface that will influence the contact stiffness. The surface only measures 40000 elements on the surface. This is not enough accuracy for a 10 x 10 mm rough surface. Ideally numerical schemes should be applied to analyse the contact stiffness of a rough surface rather than FE. This would improve accuracy and computational times.

Stitched optical scans were taken of the whole 10 mm x 10 mm area of the rough surface samples. The surface scans were captured using optical profilometry (InfiniteFocus, Bruker-Alicona, Austria). The 5x optical zoom lens was used for the 3D optical profilometry. The optical data of the rough surfaces was then post-processed and then trimmed accordingly. The optical scans of the surfaces produce extremely dense point cloud maps of the surface. This is due to the large number of scans required to map the whole rough surface design. Therefore, the stitched surface scans must be sampled and simplified to allow the data to be mapped appropriately. Ideally, the whole surface scan would be mapped onto the FE models but due to the number of data points, the rough surface in the model would become incredibly complex with an extremely fine mesh and high number of elements and nodes in the FE model. Unfortunately, this would not be viable for simulation with current computing constraints and resources available.

6.3 Results and discussion

The results section is split into four areas of investigation:

- Design to polymer replica manufacture
- Low load normal contact stiffness tests and FE model analysis
- Contact area evolution with normal contact stiffness
- Saturation stiffness tests

Initially, the design to surface realisation is examined. This was detailed in Chapter 5, where the discussion examined how there will inevitably be a difference between the numerical rough surface design, the 3D print, and the injection moulded polymer replicas. The surfaces are measured and detailed at each stage of the fabrication process. The initial elastic normal contact stiffness tests are then analysed. This subsection highlights the direct influence of a surfaces' roughness on the contact stiffness of an interface. The results from the contact stiffness measurements in the elastic regime are then compared with the trends exhibited by the FE models. The contact area measurements are then considered for each roughness design. These measurements allow the examination of the evolution of real contact area with the increase of applied normal load. This data highlights the influence of real contact area on the normal contact stiffness of an interface. Finally, the elastic-plastic tests of the rough surface designs are analysed.

6.3.1 Rough surface design manufacture

The four surface designs were conceptualised with the aim of manufacturing a range of topographies to explore how normal contact stiffness is influenced by surface roughness. The fabrication route used here inevitably generates a difference between the numerical design, the 3D print, and finally the injection moulded replica. Predominantly, the numerical design to manufacture is limited by the intermediate 3D printing stage. In this step, the resolution of the printer can limit the rough surface topography that is realised. This manufacturing limitation is examined in more depth in Section 5.4.1 in Chapter 5.

This section details the rough surface topographies that were designed and manufactured for use in the rough surface contact stiffness studies in this chapter. Details of the numerical

designs are taken from the parameters used to generate the surfaces, while the 3D printed master and injection moulded surfaces were measured using an optical profilometer. The details of the numerical design to manufacture translation are detailed in Table 6.1.

Table 6.1 – Numerical parameters used to design the generated surfaces followed by results of the scanned 3D printed masters, and injection moulded polystyrene replica surfaces.

Generated roughness, *Sq* (μm)	Generated roughness slope, *Sdq*	3D printed roughness, *Sq* (μm)	3D printed roughness slope, *Sdq*	Injection moulded roughness, *Sq* (μm)	Injection moulded roughness slope, *Sdq*
25	0.18	21.42	0.59	23.47	1.14
50	0.35	42.98	0.74	44.33	1.95
100	0.69	81.45	0.97	83.57	2.48
150	1.05	105.78	1.24	103.66	2.56

The results shown in Table 6.1 follow the same trend exhibited by the rough surface fabrication in Chapter 5. Typically, the roughness of the 3D printed surface and polymer replicas are reduced from the initial numerical design, while the slope of the roughness increases at each step of the fabrication process. However, the aim in this study was to design and manufacture four distinct rough surface topographies that exhibit a range of roughness and topographical features (i.e. the exact magnitude of each roughness level was not critical). The injection moulded polymer replicas achieve this as the roughness ranges from 23.47 μm to 103.66 μm, while the slope of the topographical features ranges from 1.14 to 2.56. These polymer surfaces facilitate the study of how surface roughness and roughness slope can influence the normal contact stiffness and real contact evolution of an interface.

6.3.2 Low load normal contact stiffness tests

The initial mechanical tests aimed to examine how the surface roughness and slope would influence normal contact stiffness of an interface. The loading of the samples was kept relatively low at 500 N to ensure predominantly elastic interactions and stresses experienced by the interface. However, it is inevitable that plastic behaviour will be present

to varying degrees for all surfaces. The applied 500 N is equivalent to a normal pressure of 5 MPa based on the nominal area of the samples.

Identical replicas of each surface design were produced from the fabrication process. This allowed repeatability tests on the rough surfaces to be performed. In typical contact stiffness tests, the measured response can be variable due to the asperity interactions encountered when an interface is brought into contact. The rough surface topography on either side of the interface results in different asperity contacts arising even when two surfaces appear to be in contact in the same alignment and position as a previous test. Here, the replica surfaces come into contact with a nominally flat sample that aims to minimise the variability of the contact interactions and isolate the importance of surface roughness in connection to interface stiffness. Three replicas of each surface design were tested following the protocol in Section 6.2.1. Each sample was tested three times to ensure repeatable results.

The results from the low load tests follow a trend of high repeatability for all surface designs. These results also exhibit a strong link between the normal contact stiffness of an interface and the surface roughness associated with each design. The average trends shown by the different surface designs during the load mechanical tests are shown in Fig. 6.6.

The results clearly illustrate that the RMS roughness of the surface greatly influences the asperity interactions at the interface and, by extension, the normal contact stiffness exhibited by each surface design. This agrees with the findings of previous studies, particularly Zhai et al [206]. Here, the researchers studied the effects of surface structure in normal contact stiffness. The authors concluded that RMS roughness is key in governing contact stiffness, especially when surfaces have similar fractal structures. This theory applies well here as the surfaces examined in this study were designed to have the same Hurst exponent and fractal dimension. The surface designs were scaled accordingly in the *z*-direction to give varying asperity heights, RMS roughness, and roughness slope.

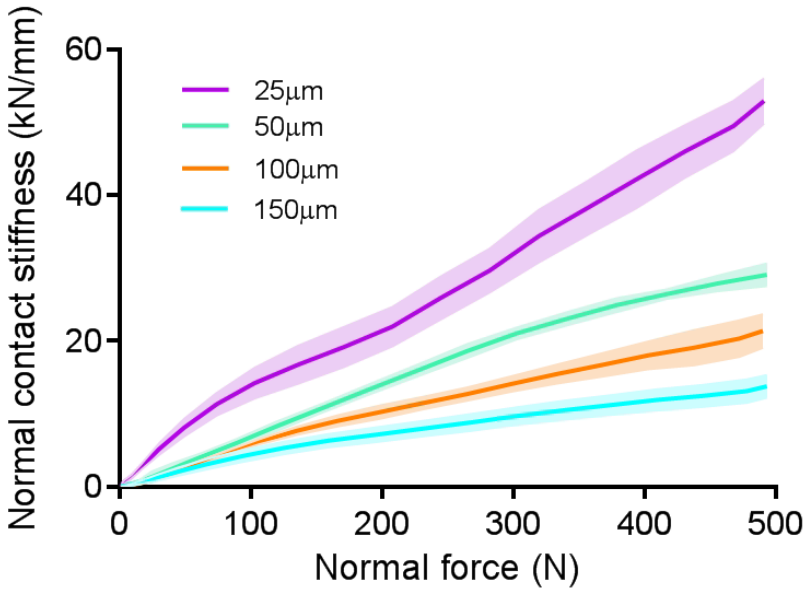

Figure 6.6 – Normal contact stiffness evolution with the applied normal load. All surface designs are shown. The ribbon plots indicate the average trend for of the normal contact stiffness and the upper and lower bounds of the results that were observed for each surface design. The values in the legend are nominal design areal RMS surface roughness Sq.

Fig. 6.6 shows a clear trend where we see the magnitude of the normal contact stiffness significantly drop as the RMS roughness of the design increases. This decrease in normal contact stiffness also coincides with an increase of the roughness slope of the surface designs. Full details are given for the tested surfaces in Table 6.1. The resulting increase in RMS roughness and slope causes the individual asperities to decrease in stiffness. The thin elongated asperities result in overall surface structures that are more compliant than the features on the low roughness design. The lower roughness asperities are shorter and wider geometrically, resulting in stiffer structures. These geometrical factors of the surface asperities cause variations in the interface's structure that directly affect the stiffness of an interface. Other factors known to affect contact stiffness such as material hardness, yield point, Young's modulus are not examined in great detail for this study as the same material, Polystyrene, was used for all designs and for the nominally flat contact surface.

However, the elastic-plastic behaviour of the rough surface designs must be considered as a factor causing the decrease in normal contact stiffness as roughness increases. As roughness increases, there are far more opportunities for stress concentrations at the asperity interactions due to their geometry, resulting in increased plastic deformation. This plastic

behaviour will cause an increase in the resultant deformation of an interface when a normal load is applied, allowing for a decrease in the normal contact stiffness measured. From the results shown in Fig. 6.6, we can assume that there is a high likelihood that there is more elastic-plastic behaviour occurring in the higher roughness designs.

Another factor that will contribute to the normal contact stiffness of the interfaces will be the real contact area exhibited. The rig shown in Section 6.2.2 was used to examine the evolution of the real contact area as the load was increased. Fig. 6.7 shows the evolution of each surface design as the load is applied from 0 to 500 N. The images in Fig. 6.7(a) show the real contact evolution for the 25 and 150 μm cases. This gives a visual representation of the real contact area growth as the normal load applied to the interface increases.

As previously discussed, the lower roughness surfaces will exhibit asperities and features that have a shorter wider geometry, compared with the taller, slim asperities associated with the higher roughness. The asperity tops associated with the lower roughness exhibit a larger surface area that can initially encounter the nominally flat surface. The higher roughness asperities will have a reduced surface area for contact. The interfaces shown in Fig. 6.7(c) and (d) show the stitched scan data of the 25 and 150 μm cases, respectively. The surface for the 25 μm case shows asperities that have a much lower RMS roughness and height difference between the peaks of the asperities. This allows more asperities to come into contact more easily at the interface as load increases. This by extension will give more material at the interface to support the applied load, leading to an increase in the normal contact stiffness. The height disparity between the sharper asperities in the 150 μm mean less asperities can easily come into contact at the interface, meaning less asperities and material in contact, which also contributes to a lower contact stiffness. This surface structure will result in a reduction in the overall normal contact stiffness as the roughness in the design increases. These effects and the behaviours of the surface designs are again supported by the work of Zhai et al [206], that examined fractally similar surfaces with increasing RMS roughness.

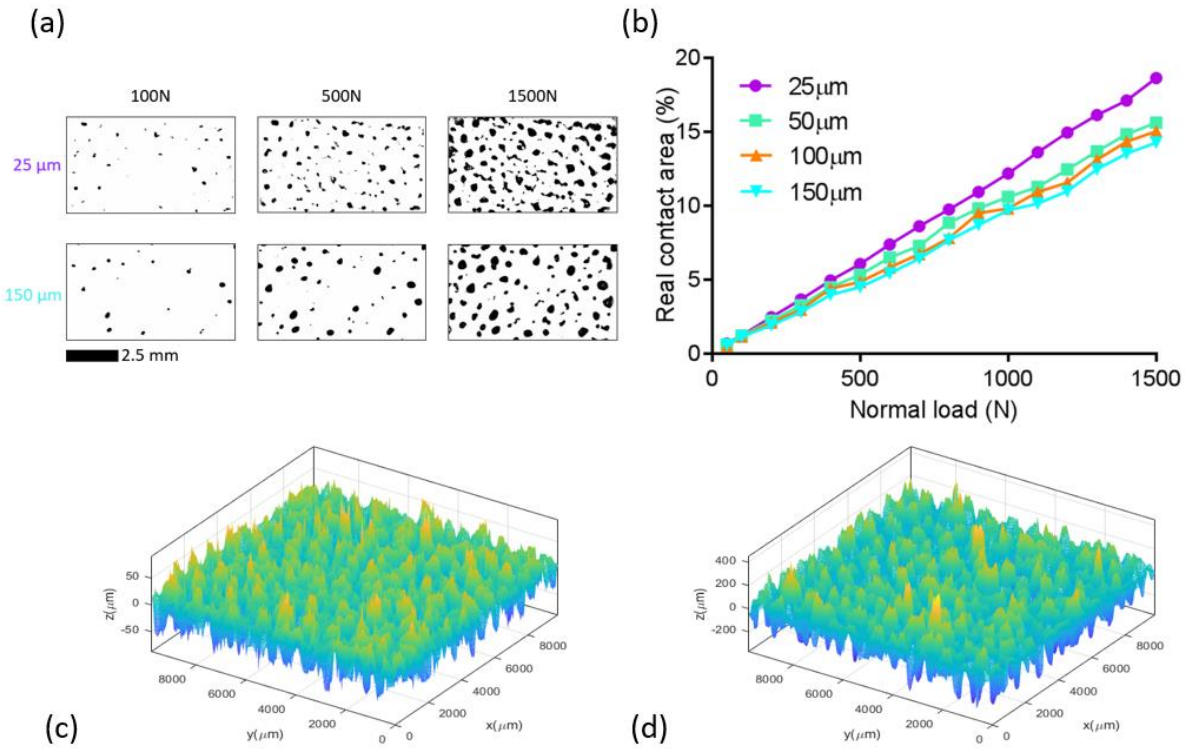

Figure 6.7 – Real contact area measurements for the normal contact stiffness tests: (a) Binary images show example images for the 25 and 150 µm design cases at 100 N, 500 N, and 1500 N applied normal load, (b) Data in the graph illustrates the evolution of real contact area for the low load events (The values in the legend are nominal design areal RMS surface roughness Sq), (c) Surface scan data of 25 µm design and (d) Surface scan data of 150 µm design.

6.3.3 FE model results

FE models were constructed (see Section 6.2.3), that enabled the simulation of the mechanical tests. The results from the 25 µm and 50 µm designs were able to be gathered, but the 100 and 150 µm cases caused significant difficulties. The nodal and element shifts required to replicate these surface designs caused highly distorted and incompatible meshes when incorporated into the FE models. This meant the decision was made not to pursue these models and focus on the behaviour exhibited by the 25 and 50 µm cases. Normally, FE models that aim to simulate rough surface contact use a small sample area such as 1 x 1 mm. This reduces the computing power required to effectively model the contact interactions. The possibility of modelling a full test is explored here to see if the general contact stiffness behaviour on a global scale could be achieved by generating a representation of the interfacial properties within an FE model. Inevitably, there would be a difference between the FE model and test as surface detail would have to sacrificed.

Fig. 6.8 shows the results from the FE models compared with the mechanical test results. The behaviour of the models follows a similar trend as the experiments with a slightly increased stiffness. This is to be expected. However, the general trend is a good indicator that the models are simulating the general mechanical behaviour exhibited in the tests by the 25 and 50 µm interfaces.

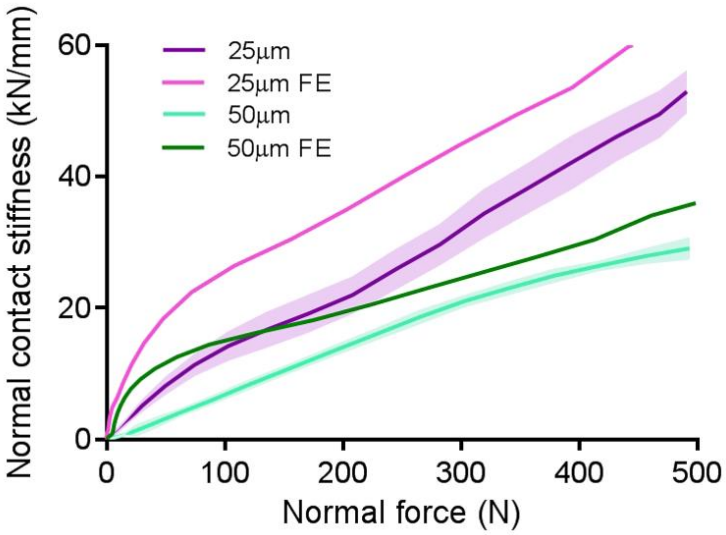

Figure 6.8 – FE model results and corresponding mechanical test normal contact stiffness results. The values in the legend are nominal design areal RMS surface roughness Sq.

The increase in stiffness seen in the models will be heavily influenced by the error occurring within the translation of the surface to the FE model approximation. The resolution limits of the 5x zoom lens on the optical profilometer are 2.82 µm in the lateral measurement range and 410 nm in the vertical range. This inevitably means surface data from the real samples is lost in the scanning procedure. The stitched scans were then altered to decrease the density of point cloud map so that it can be effectively processed in the FE software. The surface is then mapped onto a mesh of 100 x 100 nodes over a 10 x 10 mm area of the FE model representing the rough surface sample – meaning each element measuring 100 µm. This is a significant sacrifice in detail for the modelled surface, meaning the FE model is only an approximate representation of the true surface. It can only be used as an indicator of the interface behaviour.

6.3.4 Saturation stiffness tests

In this section, the rough surface designs were loaded to a higher normal load of 1500 N. This enabled the study of the behaviour of the interfaces at relatively high contact pressures, which can be expected to result in increased plastic deformation. Three samples for each surface design were loaded to 1500 N following the same normal contact stiffness test methodology. Real contact area measurements were also performed up to a load of 1500 N. This allowed the examination of the interplay between real contact area and the normal contact stiffness observed.

Fig. 6.7(b) shows the evolution of the real contact area observed when the respective samples are loaded to 1500 N, while Fig. 6.9 illustrates the evolution of the measured normal contact stiffness in each mechanical test. The traces shown in Fig. 6.9 have produced interesting results. The contact stiffness can be seen to saturate around a similar value for each rough surface design. The repeatability of the behaviour is verified with three repeat test cases for each roughness and these are seen to produce highly similar results.

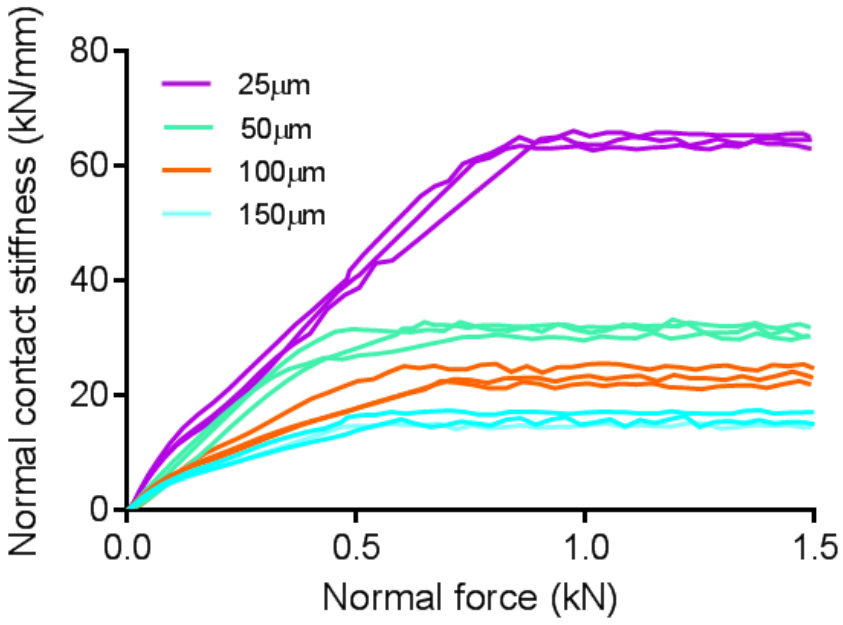

Figure 6.9 – High load normal contact stiffness results for all rough surface designs. All samples are loaded to 1500 N. The values in the legend are nominal design areal RMS surface roughness Sq.

These results are particularly interesting when considering the corresponding real contact area measurements. We can clearly see from Fig. 6.7 that, as the loading increases for the

rough surface samples, the observed contact area increases. This is the typical behaviour that is expected in real contact area measurements – i.e. as applied normal force increases, real contact area increases. This will initially be a largely elastic interaction, before transitioning into a more elastic-plastic regime. Normally, an increase in real contact area would result in an associated continual increase of the measured contact stiffness [1, 2, 6, 11, 12, 33]. More material in contact results in a stiffer interface, leading to an increase in the observed normal contact stiffness [118]. So, there should be an associated increase in normal contact stiffness from the resulting increased real contact area observed.

However, in the case of the rough surfaces observed in these tests, the normal contact stiffness increases to a point, but then saturates. Each rough surface has a varied saturation point. The smoother stiffer surfaces have a higher saturation load. This threshold load decreases as the roughness of the interface increases, as shown in Fig. 6.9. After the point of saturation, the measured normal contact stiffness continues to exhibit this saturation stiffness, even as the applied normal load increases. This opens the question to why there is a saturation stiffness observed in all test cases and for all test samples (when the contact area is still increasing – see Fig, 6.7b). It is reasonable to assume that the rough surface asperities are undergoing plastic deformation with the increasing normal load and normal contact pressures associated with the small nominal contact area of 10 x 10 mm. When an increasing plastic deformation is observed, this will lead to a decrease in the normal contact stiffness. This is most likely the behaviour being observed when the rough surface interfaces experience the larger applied normal loads. There is a continued monotonic increase in real contact area (even at the higher loads) which could cause an increase in contact stiffness. However, this is likely being counteracted by the plastic deformation experienced by the interface – thereby allowing the measured normal contact stiffness to remain at a saturated level. Similar behaviour was observed in the tailored contact stiffness tests from Chapter 4. Each structured interface's normal contact stiffness would increase with the applied normal load before reaching a threshold or saturation stiffness [118].

6.4 Conclusion

This chapter has explored the use of the 3D printing-to-injection moulding fabrication procedure developed in Chapter 5 for the study of rough surface contact stiffness. This manufacturing route was developed to enable a methodology for designing and fabricating rough surface topographies for specific research work on rough interface interaction. This chapter has applied the fabrication procedure to design and produce four rough surface designs and examined how their properties (roughness and real contact area) influence the normal contact stiffness of the interface.

The initial section of the chapter outlines the interface design and fabrication with reference to Chapter 5. Four different rough surface designs were established and the design to production translation was examined. From here, two mechanical testing methodologies were outlined. The first aimed to measure the normal contact stiffness evolution during increasing normal loading of the rough surface designs. This mechanical testing rig was adapted from the study in Chapter 4. The second mechanical test type allows the measurement of real contact area during the normal loading of the rough surfaces. The two sets of results can be examined together as they are inherently related. The results show a direct link in the low load tests, where increasing roughness can be expected to result in a lower normal contact stiffness and associated real contact area. An FE model was also developed that aimed to predict the results from the normal contact stiffness tests. The resultant models were able to map a full field optical scan of the rough surfaces onto the surface of the FE model to generate a representation of the roughness. This enabled the simulation of the contact stiffness tests on a full scale. The results compared well for the *Sq* 25 and 50 μm design cases but ran into problems with the higher roughness designs. The surface designs were then finally tested to the point that plastic deformation would begin to occur. Interesting mechanical behaviour was observed where a threshold contact stiffness was reached for the normal contact stiffness tests even though the real contact area continues increasing monotonically. This is believed to be due to increasing plastic behaviour associated with the increasing applied normal load and large contact pressures

over a small nominal area (i.e. high levels of plasticity perhaps counteract the effect of the increasing real contact area and cause the contact stiffness to saturate).

This chapter has utilised the rough surface fabrication tool developed in Chapter 5. The tool was used here to explore rough surface interfaces and how their normal contact stiffness can be influenced by surface roughness. The work illustrated how as areal roughness was increased, and interfacial contact area reduced, there was a corresponding reduction in the measured normal contact stiffness of the interfaces. The fabrication tool used here can design and produce topographies with tailored topographical characteristics, by extension this can be used to tailor the normal contact stiffness of a rough surface interface. The tool can also be used to produce high quality replicas of the interfaces, which in turn produce highly repeatable measurements of normal contact stiffness. Supporting FE models of the rough surface interfaces were able to provide predictions of the contact stiffness behaviour and measurements. If further developed these could potentially assist in the design and production of rough surface interfaces that exhibit specific normal contact stiffnesses and mechanical properties, mirroring the work in Chapter 4. Contact stiffness was explored using the tools in this chapter, but this could be extended to other interfacial properties such as friction, adhesion, surface drag, wettability, lubricant penetration, and wear.

Chapter 7

Conclusions and Future Work

This chapter provides a summary of the work carried out in this thesis and its key outcomes. Motivations and background knowledge to the work have been detailed in the respective chapters. The information here will detail what has been achieved in each aspect of the work. Potential future work is detailed for the individual sections of work where appropriate. Each part is discussed individually followed by a final summary.

7.1 Thesis summary and further work additions

7.1.1 Fabrication of micro-structured interfaces

The beginnings of the project explored microfabrication techniques and how these could be utilised to develop a new novel way to manufacture microstructured polymer interfaces. This work required extensive initial research into the necessary cleanroom techniques that would allow the development of an effective silicon etching protocol. Even though this area is well established, it is common to have to trial many methods before generating the required etch profile in a silicon master.

Once an etching protocol was established, the next stage of nanoimprint lithography was explored. This stage in the fabrication protocol allowed the development of hybrid polymer inlays to be used in the final injection moulding stage of the fabrication procedure. The nanoimprint protocol was optimised to allow the effective replication of the micro-structured silicon masters. From here, the hybrid polymer inlays could be utilised to manufacture micro-structured polymer replicas that would emulate the initial silicon master profile. The injection moulding stage required extensive optimisation as many factors contribute to the effectiveness of an injection moulding manufacturing cycle.

Once the microfabrication protocol was established it could then be optimised and its capabilities explored. This stage required the development of design case studies that investigated how well the manufacturing procedure could fabricate certain microstructures.

This enables the user to develop an idea of what type of devices can effectively be created using this microfabrication technique.

Overall, this work was successful as it allowed the development of a rapid prototyping protocol that enables a wide range of micro-structured interfaces to be created in a range of polymer materials via injection moulding. Future work would include further exploring the capabilities of the process. It would be viable to explore more etch profiles to potentially push the lower limits of the microfeature sizes generated in the polymer replicas. This would require exploration of different etch types, photoresists, and etch recipes along with the optimisation of the nanoimprinting and injection moulding protocols for each design. Further work would also explore the creation of more complex devices using this microfabrication technique. In this thesis, the primary purpose of this section of work was to produce structured surfaces to achieve interfaces with tailored and repeatable contact stiffness. As we will see in the next section, this was successful.

7.1.2 Repeatable and tailored normal contact stiffness

This chapter built upon the polymer microfabrication techniques developed in Chapter 3. This allowed the design and development of a series of microstructured interfaces that aimed to explore the viability of repeatable and tailored normal contact stiffness.

The initial development of this work involved constructing appropriate finite element (FE) models based on the potential interface designs that would be manufactured and mechanically tested. The FE models provided an understanding of the mechanical behaviour that could be expected from the designed interfaces. The designed interfaces aimed to provide a range of contact area ratios and range of interfacial stiffnesses to provide evidence that contact stiffness can be controlled and designed based on the geometry of a microstructured interface. A range of interfaces were produced using the microfabrication production technique. The produced interfaces were examined and used to develop more accurate FE models that would represent the exact dimensions of the produced interfaces.

The interfaces were mechanically tested using a bespoke experimental microtest rig. The rig allowed the simple and accurate measurement of the normal contact stiffness of an

interface. All interface designs were tested and compared to the refined FE models. The results showed clear repeatability across the interfaces and an increasing contact stiffness that corresponded to the wider microstructured features, or increased contact area ratio. The results also compared very well to the FE model results.

The work developed here has highlighted the viability for designing and manufacturing microstructured interfaces that will exhibit tailored mechanical contact properties. This has the potential to be useful in many mechanical design situations such as aerospace, automotive, and energy systems where traditional interfaces can be highly unpredictable and produce uncertainty/inefficiency within a design. The strong agreement between FE model prediction and experimental results show that the interfaces can be designed and simulated before manufacture, potentially saving time and expenditure during the mechanical design phase of an interface or component.

One area of further work here is the applicability of the designs for real engineering systems, possibly turbine blade housings, engine block interfaces, mechanical damping systems and experimental rig design. These situations can potentially highlight how the integrated microstructured interface can benefit the modelling and design of a mechanical system. The issue of how the geometry of a microstructured interface can affect the mechanical properties also requires further study. This would involve exploring aspect ratios and microstructure geometries, varying the interface point of contact shape, materials for the interfaces, and different manufacturing methodologies. Tangential contact stiffness of microstructured interfaces must also be explored to give a full picture of the benefits of tailored and repeatable interface design. These are all areas that could be explored to highlight the true potential of microstructured interfaces in enabling repeatable and tailorable interface properties.

7.1.3 3D printing and rapid replication of advanced numerically generated rough surface topographies

This work developed a research tool and novel manufacturing approach that facilitated the rapid replication of designed rough surface topographies in various polymer materials. The

work began with developing a method for 3D printing rough surface topographies effectively with the aim of producing repeatable rough surfaces. From here, the project developed to allow the design of rough surface topographies with varying surface parameters. These could be translated into a 3D printed topography through a highly accurate SLA 3D printing process.

The 3D printed topographies were then used in two replication methods, polymer casting and injection moulding, to allow a wider range of polymers to be used in creating the tailored rough surface designs. Two surface comparison methods were used to analyse the replication quality in each manufacturing technique. The replication analysis highlighted what polymers and manufacturing type would be most effective depending on the user's needs.

A study was executed to understand the effects of how the viscosity of the polymer being cast can effect the replication quality. A durability study was also performed to highlight the viability of injection moulding to rapid prototype large numbers of polymer replicas of the rough surface designs. Finally, work was undertaken that detailed the design and production of various rough surfaces all with the same areal roughness, but different spatial topographical properties (i.e. wavelength). This showed how the rough surfaces could indeed be designed to generate topographies with wide ranging wavelengths to allow users to manufacture a design to suit their research needs.

The ability to generate and fabricate rough surface topographies in a range of polymers according to flexible design parameters is a powerful research tool. Surface roughness is everywhere in both nature and engineering design. The tool developed allows researchers to explore interfacial phenomena and properties specific to their research field with a more controlled approach to rough surface fabrication than previously available. Hopefully this work will prompt an array of more advanced engineering and experimental studies on how rough surface characteristics can effect interfacial phenomena. This is where the further scope for this project lies. The tool must be applied in various engineering fields to explore how certain topographical characteristics influence biological systems, contact mechanics, aerodynamics, and electromechanical systems. Indeed, at the time of writing, it has already been applied in a study on the effect of surface roughness in triboelectric nanogenerators

due to be published in 2023 [198]. For the present thesis, the concentration remains on contact stiffness and hence, one of the advantages of fabricating pre-designed rough surfaces (with very specific topographical properties) is to also enable an investigation into the repeatability and tailorability of contact stiffness for multiscale rough surfaces. This was the subject of the next section.

7.1.4 Application of rough surface fabrication tool to the study of rough surface contact stiffness

The final research chapter developed as an exploration of the potential capabilities of the rough surface 3D printing tool developed in Chapter 5. Here, the rough surfaces fabrication tool was applied to the study of rough surface contact stiffness. The study details the design and fabrication of four rough surfaces fabricated using the injection moulding sub-technique. These designs were used to explore the role of surface roughness in normal contact stiffness and real contact area evolution with increasing normal loading. Specifically, it explores the question we already explored for the structured surfaces; namely, can rough surfaces be designed to enable interfaces with repeatable and tailorable contact stiffness?

The surface designs were mechanically tested using two methods. Normal contact stiffness was measured using an adapted mechanical testing methodology detailed in Chapter 4, while the real contact area measurements were made using a novel optical method. This method has rarely been used to compare with contact stiffness results; thereby, allowing for a clearer picture of the mechanics at a surface level during in situ normal contact stiffness tests. The results show a direct link between the normal contact stiffness and surface roughness of a topography, with increasing roughness resulting in a more compliant interface and lower measured normal contact stiffnesses. The same can also be seen in the contact measurements where real contact area reduced as surface roughness increased. A rough surface FE model was also developed that produced a simulation of the full experimental set up for the normal contact stiffness tests. The models simulated the rough surfaces by mapping optical scans of the topographies for each case. The simulations compared well for the two lower roughness cases, 25 and 50 μm, but encountered convergence and meshing issues with the two higher roughness designs.

Crucially, results here showed that good levels of repeatability and tailorability could also be achieved for the designed rough surfaces. Further work emerging from this chapter might involve exploring how manipulating other surface characteristics such as the frequencies of asperities that make up a topography can influence normal contact stiffness. This would involve creating a design study to generate an array of rough surface designs with wide ranging and varied surface characteristics. The surfaces could then be mechanically tested to measure normal and tangential contact stiffness. The possibilities with rough surface design as applied to other interface properties would be very interesting also – for, example: adhesion, friction, and lubrication studies could also be explored. This thesis focused on contact stiffness. However, the rough surface fabrication method in Chapter 5 could be applied to the study of a very wide range of interfacial phenomenon.

7.2 Thesis conclusions and future work recommendations

This section will examine how effectively the aims and objectives of this thesis were achieved. This will involve recommendations for further work where objectives were not fully satisfied.

- Establish and develop novel fabrication routes that facilitate the production of complex microstructured thermoplastic polymer topographies. This will be achieved by combining reliable, repeatable fabrication and manufacturing techniques available both in the James Watt nanofabrication centre and the manufacturing technologies at the MMRG and BIG research groups.

The methods detailed in chapter 3 and 4 satisfy this goal. A detailed and structured methodology was developed that enables users to design and produce microstructured topographies in a range of thermoplastic polymers. This was achieved by gathering expertise from the MMRG, BIG, and JWNC facilities.

- Further develop this fabrication technique to establish a clear cleanroom microfabrication to injection moulding rapid prototyping route for MEMS device design and manufacture. This technique should allow for high throughput for potential application into mass production.

This aim was achieved by investigation of how the microfabrication technique could be applied to microfluidic device fabrication. The complexity of the microfluidic design used highlights the capabilities of the methodology to fabricate high quality complex MEMS devices. A durability study was executed to investigate the feasibility of the manufacturing techniques application into mass production. It was concluded that the technique should be limited to around 100 samples for MEMS device fabrication, especially for more complex devices. This means that the technique is suitable for rapid prototyping and bespoke microstructured device manufacture. However, it would not be able to produce high quality devices at the component numbers associated with mass production, i.e. 1000s of components per microstructured inlay. More durable inlays would have to be developed to enable mass production capabilities.

- A clear analysis method must be established for assessing the topographical features of the microstructured polymer interfaces. This will allow for full assessment of microfeature quality, and part replication throughout the stages of the fabrication technique.

A methodology was developed for the analysis of feature quality and dimensions. This enabled the analysis of microfeature replication through the various stages of the fabrication procedure. This methodology combined SEM imaging and optical profilometry scans. This allowed for a visual analysis of part quality (SEM) combined with mathematical measurements of the microstructured components (optical scans). The methodology here allowed users assess microfeature fidelity throughout the manufacturing process, quantifying the success of the manufacturing method.

- Investigate the full capabilities of the microfabrication technique. How versatile is the fabrication method? Potential assessment can involve the range of features can be made, device complexity, feature shape and spacing, and aspect ratio of features the devices that can be fabricated using the techniques developed.

This goal was partially achieved. The capabilities of the technique were explored in terms of fabricating complex features and designs, aspect ratio studies, feature spacing etc. However,

these could be extended into further studies that would convey the full scope of the fabrication method. Also, this would highlight to potential users how the methods could be applied to new fields. It should be noted that mainly channels and linear features were explored. This should be extended to an array of shapes and configurations in the silicon microstructures for replication. This would highlight any shapes that were problematic and appropriate design considerations that should be engaged with during the fabrication process.

- Explore the capabilities of microstructured polymer interface's ability to provide tailored and repeatable normal contact stiffness. Develop appropriate mechanical test rig and methodology to facilitate the measurement of normal contact stiffness. Generate FE models to support, validate the empirical results, and guide the testing methodology of microstructured interfaces.

In chapter 4 it was shown that the microstructured polymer interfaces could be designed to exhibit user defined normal contact stiffnesses. The design process started with FE models to develop predictions of the mechanical properties of the interfaces. These FE results allow the user to predict the mechanical behaviour of the designed interfaces. A mechanical test rig was developed that facilitated an accurate measurement of the normal contact stiffness of the microstructured interfaces using a Deben microtest machine and a DIC optical system. The results were validated against the FE models. The mechanical properties of the interfaces were shown to be highly repeatable and tailorable to the user's requirements.

- Investigate how the microstructured surface designs can influence the tangential contact stiffness of an interface. With further aims of creating tailored and tuneable tangential contact stiffness characteristics of an interface.

This aim was unfortunately not explored during any of the work in this thesis. Initially it had been planned to develop FE models and mechanical testing methods that would explore how tangential contact stiffness can be tuned using microstructured interface designs. This aimed to compliment the microstructured interface work on normal contact stiffness. This

would be a major project that could be explored in future research. It would require a new mechanical test rig and related FE models to perform a similar study as seen in chapter 4.

- Attempt to develop a manufacturing route that can facilitate repeatable and tuneable rough surface interface designs. Explore how rough surface topographical features influence the normal contact stiffness of an interface.

A rough surface generation and replication tool was developed to allow the user to design and fabricate rough surface topographies that were repeatable in nature. The designs could be tuned to exhibit certain a certain roughness, feature slope, asperity frequency and distribution. These were then 3D printed and used to make polymer copies. The tool was used to generate and produce repeatable rough surfaces that were examined using the normal contact stiffness testing methodology developed in chapter 4. This rough surface generation method is versatile, but it should be added that more capability and control into the design of the surfaces would make this a more powerful research tool. With more scope to be applied in further work.

- Establish a clear protocol to full analyse the quality of rough surface topographies and the quality of replica polymer samples.

A clear protocol was developed using existing literature for examining rough surface similarity and replication. The quality of the rough surface replication could be analysed using the cross-correlation ratio surface examination and validated using 3D modelling tools available on the Alicona optical profilometer.

- Explore what topographical features of rough surface interfaces influence TENG design and by extension device performance and efficiency.

This work was not included within the thesis as it was still being completed during the final stages of writing. The rough surface generation tool has subsequently been used to analyse how surface roughness influences TENG design performance. However, this could be extended to the microstructured interface work and how topography contact area shapes and stiffnesses influence the TENG output and efficiency.

Surface design and contact mechanics are critical to the engineering world. A strong command of interface design and an understanding of interfacial mechanical behaviour can enable an engineer to improve the performance of multicomponent systems and develop innovative solutions. This was the primary driving force behind the work of the present thesis.

The work in this thesis has involved studying the design and manufacture of both microstructured and rough surface interfaces. This has enabled investigation into the mechanical behaviour of surfaces and how to tailor them for more efficient engineering design. Specifically, the mechanical property of normal contact stiffness was explored. It was found that interfaces can be created that embody repeatable and tailored contact stiffness defined by the user for a specific engineering solution. This can be easily achieved in both the microstructured, and pre-defined rough surface interfaces. These discoveries have the potential to benefit mechanical systems where performance is affected by interfacial stiffness – frictional joints in engines and turbines, vibrational response of multicomponent machines, tribology of biomedical joints, robotic gripping systems etc. The work here also has the potential to extend to further interfacial phenomena studies. This allows the users to explore innovative interface designs and their behaviour to improve engineering design.

References

1. Sherif HA, Kossa SS. Relationship between normal and tangential contact stiffness of nominally flat surfaces. Wear. 1991 Nov 30;151(1):49-62.
2. Parel, Kurien. An Analysis of Contact Stiffness and Frictional Receding Contacts. PhD thesis. University of Oxford; 2017.
3. Yang C, Persson BN. Contact mechanics: contact area and interfacial separation from small contact to full contact. Journal of Physics: Condensed Matter. 2008 Apr 22;20(21):215214.
4. Poon CY, Bhushan B. Numerical contact and stiction analyses of Gaussian isotropic surfaces for magnetic head slider/disk contact. Wear. 1996 Dec 30;202(1):68-82.
5. Cutkosky MR, Wright PK. Friction, stability and the design of robotic fingers. The International Journal of Robotics Research. 1986 Dec;5(4):20-37.
6. Shi X, Polycarpou AA. Measurement and modeling of normal contact stiffness and contact damping at the meso scale. J. Vib. Acoust.. 2005 Feb 1;127(1):52-60.
7. Medina S, Nowell D, Dini D. Analytical and numerical models for tangential stiffness of rough elastic contacts. Tribology Letters. 2013 Jan;49(1):103-15.
8. Gonzalez-Valadez M, Baltazar A, Dwyer-Joyce RS. Study of interfacial stiffness ratio of a rough surface in contact using a spring model. Wear. 2010 Feb 4;268(3-4):373-9.
9. Campana C, Persson BN, Müser MH. Transverse and normal interfacial stiffness of solids with randomly rough surfaces. Journal of physics: condensed matter. 2011 Feb 3;23(8):085001.
10. Mulvihill, Daniel. Studies of Frictional Interface Behaviour: Experiments and Modelling. PhD thesis. University of Oxford; 2012.
11. Persson BN. Relation between interfacial separation and load: a general theory of contact mechanics. Physical review letters. 2007 Sep 18;99(12):125502.
12. Mulvihill DM, Brunskill H, Kartal ME, Dwyer-Joyce RS, Nowell D. A comparison of contact stiffness measurements obtained by the digital image correlation and ultrasound techniques. Experimental Mechanics. 2013 Sep;53(7):1245-63.

13. Wang D, Ueckermann A, Schacht A, Oeser M, Steinauer B, Persson BN. Tire–road contact stiffness. Tribology letters. 2014 Nov;56(2):397-402.
14. Kartal ME, Mulvihill DM, Nowell D, Hills DA. Measurements of pressure and area dependent tangential contact stiffness between rough surfaces using digital image correlation. Tribology International. 2011 Sep 1;44(10):1188-98.
15. Kartal ME, Mulvihill DM, Nowell D, Hills DA. Determination of the frictional properties of titanium and nickel alloys using the digital image correlation method. Experimental Mechanics. 2011 Mar;51(3):359-71.
16. Królikowski J, Szczepek J. Assessment of tangential and normal stiffness of contact between rough surfaces using ultrasonic method. Wear. 1993 Feb 1;160(2):253-8.
17. Dwyer-Joyce RS, Gonzalez-Valadez M. Ultrasonic determination of normal and shear interface stiffness and the effect of Poisson's ratio. InTribology Series 2003 Jan 1 (Vol. 43, pp. 143-149). Elsevier.
18. Berthoud, P., Baumberger, T., 1998. Shear stiffness of a solid-solid multicontact interface. Proceedings of the Royal Society A: Mathematical, Physical and Engineering Sciences 454, 1615–1634.
19. Greenwood JA, Williamson JP. Contact of nominally flat surfaces. Proceedings of the royal society of London. Series A. Mathematical and physical sciences. 1966 Dec 6;295(1442):300-19.
20. Tim Timoshenko S. Theory of elasticity. McGraw-hill; 1951.
21. Persson BN. Contact mechanics for randomly rough surfaces. Surface science reports. 2006 Jun 1;61(4):201-27.
22. Jackson RL, Green I. A statistical model of elasto-plastic asperity contact between rough surfaces. Tribology International. 2006 Sep 1;39(9):906-14.
23. Greenwood JA, Williamson JP. Contact of nominally flat surfaces. Proceedings of the royal society of London. Series A. Mathematical and physical sciences. 1966 Dec 6;295(1442):300-19.
24. Jones RE, Zeigler DA. A method for determining the asperity distribution of contacting rough surfaces. J. Trib.. 2005 Jan 1;127(1):24-9.

25. Sevostianov I, Kachanov M. Contact of rough surfaces: a simple model for elasticity, conductivity and cross-property connections. Journal of the Mechanics and Physics of Solids. 2008 Apr 1;56(4):1380-400.
26. Bush AW, Gibson RD, Thomas TR. The elastic contact of a rough surface. Wear. 1975 Nov 1;35(1):87-111.
27. Ciavarella M, Greenwood JA, Paggi M. Inclusion of "interaction" in the Greenwood and Williamson contact theory. Wear. 2008 Aug 25;265(5-6):729-34.
28. Pfeifer P. Fractal dimension as working tool for surface-roughness problems. Applications of Surface Science. 1984 May 1;18(1-2):146-64.
29. Persson BN. Contact mechanics for randomly rough surfaces. Surface science reports. 2006 Jun 1;61(4):201-27.
30. Hyun S, Pei L, Molinari JF, Robbins MO. Finite-element analysis of contact between elastic self-affine surfaces. Physical review E. 2004 Aug 31;70(2):026117.
31. Pei L, Hyun S, Molinari JF, Robbins MO. Finite element modeling of elasto-plastic contact between rough surfaces. Journal of the Mechanics and Physics of Solids. 2005 Nov 1;53(11):2385-409.
32. Akarapu S, Sharp T, Robbins MO. Stiffness of contacts between rough surfaces. Physical Review Letters. 2011 May 20;106(20):204301.
33. Pohrt R, Popov VL. Normal contact stiffness of elastic solids with fractal rough surfaces. Physical Review Letters. 2012 Mar 5;108(10):104301.
34. Persson BN. Contact mechanics for randomly rough surfaces: on the validity of the method of reduction of dimensionality. Tribology Letters. 2015 Apr;58(1):1-4.
35. Popov VL. Comment on "Contact Mechanics for Randomly Rough Surfaces: On the Validity of the Method of Reduction of Dimensionality" by Bo Persson in Tribology Letters. Tribology Letters. 2015 Nov;60(2):1-7.
36. Pastewka L, Prodanov N, Lorenz B, Müser MH, Robbins MO, Persson BN. Finite-size scaling in the interfacial stiffness of rough elastic contacts. Physical Review E. 2013 Jun 18;87(6):062809.
37. Etsion I. Revisiting the Cattaneo–Mindlin concept of interfacial slip in tangentially loaded compliant bodies.

38. Zhao B, Zhang S, Wang P, Hai Y. Loading–unloading normal stiffness model for power-law hardening surfaces considering actual surface topography. Tribology International. 2015 Oct 1;90:332-42.
39. Etsion I, Kligerman Y, Kadin Y. Unloading of an elastic–plastic loaded spherical contact. International Journal of Solids and Structures. 2005 Jun 1;42(13):3716-29.
40. Brizmer V, Kligerman Y, Etsion I. The effect of contact conditions and material properties on the elasticity terminus of a spherical contact. International journal of solids and structures. 2006 Sep 1;43(18-19):5736-49.
41. Paggi M, Pohrt R, Popov VL. Partial-slip frictional response of rough surfaces. Scientific reports. 2014 Jun 5;4(1):1-6.
42. Li S, Yao Q, Li Q, Feng XQ, Gao H. Contact stiffness of regularly patterned multi-asperity interfaces. Journal of the Mechanics and Physics of Solids. 2018 Feb 1;111:277-89.
43. Digitalimagecorrelation.org [Internet]. digitalimagecorrelation.org. [cited 2023Jan23]. Available from: https://digitalimagecorrelation.org/
44. Reu P. All about speckles: contrast. Experimental Techniques. 2015 Jan;39(1):1-2.
45. Sutton MA, Orteu JJ, Schreier H. Image correlation for shape, motion and deformation measurements: basic concepts, theory and applications. Springer Science & Business Media; 2009 Apr 21.
46. Zhou HF, Dou HY, Qin LZ, Chen Y, Ni YQ, Ko JM. A review of full-scale structural testing of wind turbine blades. Renewable and Sustainable Energy Reviews. 2014 May 1;33:177-87.
47. Palanca M, Tozzi G, Cristofolini L. The use of digital image correlation in the biomechanical area: a review. International biomechanics. 2016 Jan 1;3(1):1-21.
48. De Crevoisier J, Swiergiel N, Champaney L, Hild F. Identification of in situ frictional properties of bolted assemblies with digital image correlation. Experimental mechanics. 2012 Jul;52(6):561-72.
49. Biwa S, Hiraiwa S, Matsumoto E. Stiffness evaluation of contacting surfaces by bulk and interface waves. Ultrasonics. 2007 Dec 1;47(1-4):123-9.

50. Biwa S, Suzuki A, Ohno N. Evaluation of interface wave velocity, reflection coefficients and interfacial stiffnesses of contacting surfaces. Ultrasonics. 2005 May 1;43(6):495-502.
51. Kim JY, Baltazar A, Rokhlin SI. Ultrasonic assessment of rough surface contact between solids from elastoplastic loading–unloading hysteresis cycle. Journal of the Mechanics and Physics of Solids. 2004 Aug 1;52(8):1911-34.
52. Kendall K, Tabor D. An utrasonic study of the area of contact between stationary and sliding surfaces. Proceedings of the Royal Society of London. A. Mathematical and Physical Sciences. 1971 Jun 22;323(1554):321-40.
53. Tattersall HG. The ultrasonic pulse-echo technique as applied to adhesion testing. Journal of Physics D: Applied Physics. 1973 May 1;6(7):819.
54. Baik JM, Thompson RB. Ultrasonic scattering from imperfect interfaces: a quasi-static model. Journal of Nondestructive Evaluation. 1984 Dec;4(3):177-96.
55. Starzynski G, Buczkowski R. Ultrasonic measurements of contact stiffness between rough surfaces. Journal of Tribology. 2014 Jul 1;136(3):034503.
56. Nowell D, Mulvihill D, Brunskill H, Kartal M, Dwyer-Joyce R. Measurement and modelling of interface stiffness in frictional contacts. D. Nowell, D. Mulvihill, H. Brunskill, M. Kartal, R. Dwyer-Joyce//5th WTC. 2013(3):2232-5.
57. Dubey AK, Yadava V. Laser beam machining—A review. International Journal of Machine Tools and Manufacture. 2008 May 1;48(6):609-28.
58. Dalili N, Edrisy A, Carriveau R. A review of surface engineering issues critical to wind turbine performance. Renewable and Sustainable energy reviews. 2009 Feb 1;13(2):428-38.
59. Zhou M, Pesika N, Zeng H, Tian Y, Israelachvili J. Recent advances in gecko adhesion and friction mechanisms and development of gecko-inspired dry adhesive surfaces. Friction. 2013 Jun;1(2):114-29.
60. Lasagni A, Mücklich F, Nejati MR, Clasen R. Periodical surface structuring of metals by laser interference metallurgy as a new fabrication method of textured solar selective absorbers. Advanced engineering materials. 2006 Jun;8(6):580-4.

61. Alamri S, El-Khoury M, Aguilar-Morales AI, Storm S, Kunze T, Lasagni AF. Fabrication of inclined non-symmetrical periodic micro-structures using Direct Laser Interference Patterning. Scientific reports. 2019 Apr 1;9(1):1-2.
62. Lang V, Roch T, Lasagni AF. High-Speed Surface Structuring of Polycarbonate Using Direct Laser Interference Patterning: Toward 1 m2 min− 1 Fabrication Speed Barrier. Advanced Engineering Materials. 2016 Aug;18(8):1342-8.
63. Yao L, He J. Recent progress in antireflection and self-cleaning technology–From surface engineering to functional surfaces. Progress in Materials Science. 2014 Apr 1;61:94-143.
64. Mohamed AM, Abdullah AM, Younan NA. Corrosion behavior of superhydrophobic surfaces: A review. Arabian Journal of Chemistry. 2015 Nov 1;8(6):749-65.
65. Zhao D, Tian Q, Wang M, Jin Y. Study on the hydrophobic property of shark-skin-inspired micro-riblets. Journal of Bionic Engineering. 2014 Jun 1;11(2):296-302.
66. Vedaprakash L, Dineshram R, Ratnam K, Lakshmi K, Jayaraj K, Babu SM, Venkatesan R, Shanmugam A. Experimental studies on the effect of different metallic substrates on marine biofouling. Colloids and Surfaces B: Biointerfaces. 2013 Jun 1;106:1-0.
67. Juodkazis S, Nishi Y, Misawa H, Mizeikis V, Schecker O, Waitz R, Leiderer P, Scheer E. Optical transmission and laser structuring of silicon membranes. Optics express. 2009 Aug 17;17(17):15308-17.
68. Gečys P, Račiukaitis G, Gedvilas M, Selskis A. Laser structuring of thin-film solar cells on polymers. The European Physical Journal-Applied Physics. 2009 Apr;46(1).
69. Engelhart P, Harder NP, Grischke R, Merkle A, Meyer R, Brendel R. Laser structuring for back junction silicon solar cells. Progress in Photovoltaics: Research and Applications. 2007 May;15(3):237-43.
70. Rodríguez-Vidal E, Sanz C, Soriano C, Leunda J, Verhaeghe G. Effect of metal micro-structuring on the mechanical behavior of polymer–metal laser T-joints. Journal of Materials Processing Technology. 2016 Mar 1;229:668-77.
71. Etsion I, Halperin G. A laser surface textured hydrostatic mechanical seal. Tribology Transactions. 2002 Jan 1;45(3):430-4.

72. Etsion I. Improving tribological performance of mechanical components by laser surface texturing. Tribology letters. 2004 Nov;17(4):733-7.
73. Ryk G, Etsion I. Testing piston rings with partial laser surface texturing for friction reduction. Wear. 2006 Oct 20;261(7-8):792-6.
74. Wakuda M, Yamauchi Y, Kanzaki S, Yasuda Y. Effect of surface texturing on friction reduction between ceramic and steel materials under lubricated sliding contact. Wear. 2003 Feb 1;254(3-4):356-63.
75. Li J, Xiong D, Dai J, Huang Z, Tyagi R. Effect of surface laser texture on friction properties of nickel-based composite. Tribology International. 2010 May 1;43(5-6):1193-9.
76. Garrido AH, González R, Cadenas M, Battez AH. Tribological behavior of laser-textured NiCrBSi coatings. Wear. 2011 Jun 22;271(5-6):925-33.
77. Hu T, Hu L, Ding Q. Effective solution for the tribological problems of Ti-6Al-4V: Combination of laser surface texturing and solid lubricant film. Surface and Coatings technology. 2012 Aug 15;206(24):5060-6.
78. Tang W, Zhou Y, Zhu H, Yang H. The effect of surface texturing on reducing the friction and wear of steel under lubricated sliding contact. Applied surface science. 2013 May 15;273:199-204.
79. Fan H, Zhang Y, Hu T, Song J, Ding Q, Hu L. Surface composition–lubrication design of Al2O3/Ni laminated composites—Part I: Tribological synergy effect of micro–dimpled texture and diamond–like carbon films in a water environment. Tribology International. 2015 Apr 1;84:142-51.
80. Kwok CT, Man HC, Cheng FT, Lo KH. Developments in laser-based surface engineering processes: with particular reference to protection against cavitation erosion. Surface and Coatings Technology. 2016 Apr 15;291:189-204.
81. N. Gadegaard, S. Mosler, N.B. Larsen, Biomimetic polymer nanostructures by injection moulding, 2003. Macromolecular Materials Engineering. 288 (1) 76–83.
82. Macintyre D, Thoms S. The fabrication of high resolution features by mould injection. Microelectronic Engineering. 1998 Mar 1;41:211-4.

83. Yoon SH, Srirojpinyo C, Lee JS, Mead JL, Matsui S, Barry CM. Evaluation of novel tooling for nanoscale injection molding. InSmart Structures and Materials 2005: Smart Electronics, MEMS, BioMEMS, and Nanotechnology 2005 May 16 (Vol. 5763, pp. 107-116). SPIE.

Zhao J, Ong R, Chen G, Juay YK, Ng FL, Lee MW, Kua CH. Development of rapid manufacturing technology of polymer microfluidic devices by micro moulding using silicon mould inserts. International Conference on Nanochannels, Microchannels, and Minichannels 2008 Jan 1 (Vol. 48345, pp. 1187-1194).

84. Yoon SH, Palanisamy P, Padmanabha P, Mead JL, Barry CM. Comparison of tooling materials in injection molding of microscale features. InASME International Mechanical Engineering Congress and Exposition 2009 Jan 1 (Vol. 43857, pp. 545-552).

85. Hansen TS, Selmeczi D, Larsen NB. Fast prototyping of injection molded polymer microfluidic chips. Journal of Micromechanics and Microengineering. 2009 Dec 2;20(1):015020.

86. Park SH, Lee WI, Moon SN, Yoo YE, Cho YH. Injection molding micro patterns with high aspect ratio using a polymeric flexible stamper. eXPRESS Polymer Letters. 2011 Nov 1;5(11):950-8.

87. N. Zhang, C.J. Byrne, D.J. Browne, M.D. Gilchrist, 2012. Towards nano-injection molding, Materials Today 15 (5) 216–221.

88. Stormonth-Darling JM, Gadegaard N. Injection moulding difficult nanopatterns with hybrid polymer inlays. Macromolecular materials and engineering. 2012 Nov;297(11):1075-80.

89. Hamilton A, Perris J, Convery N, Mulvihill DM, Gadegaard N. Flexible Inserts for Injection Molding of Complex Micro-Structured Polymer Components. Macromolecular Materials and Engineering. 2021 Sep;306(9):2100223.

90. Moon SD, Lee N, Kang S. Fabrication of a microlens array using micro-compression molding with an electroformed mold insert. Journal of Micromechanics and Microengineering. 2002 Dec 4;13(1):98.

91. Su YC, Shah J, Lin L. Implementation and analysis of polymeric microstructure replication by micro injection molding. Journal of Micromechanics and Microengineering. 2003 Dec 17;14(3):415.
92. Stormonth-Darling JM, Pedersen RH, How C, Gadegaard N. Injection moulding of ultra high aspect ratio nanostructures using coated polymer tooling. Journal of Micromechanics and Microengineering. 2014 Jun 23;24(7):075019.
93. Hansen HN, Hocken RJ, Tosello G. Replication of micro and nano surface geometries. CIRP annals. 2011 Jan 1;60(2):695-714.
94. Zhang N, Srivastava A, Kirwan B, Byrne R, Fang F, Browne DJ, Gilchrist MD. Manufacturing microstructured tool inserts for the production of polymeric microfluidic devices. Journal of Micromechanics and Microengineering. 2015 Aug 10;25(9):095005.
95. Giboz J, Copponnex T, Mélé P. Microinjection molding of thermoplastic polymers: a review. Journal of micromechanics and microengineering. 2007 May 15;17(6):R96.
96. Zhang N, Srivastava AP, Browne DJ, Gilchrist MD. Performance of nickel and bulk metallic glass as tool inserts for the microinjection molding of polymeric microfluidic devices. Journal of Materials Processing Technology. 2016 May 1;231:288-300.
97. Khan Malek C, Coudevylle JR, Jeannot JC, Duffait R. Revisiting micro hot-embossing with moulds in non-conventional materials. Microsystem technologies. 2007 Mar;13(5):475-81.
98. Ngo TD, Kashani A, Imbalzano G, Nguyen KT, Hui D. Additive manufacturing (3D printing): A review of materials, methods, applications and challenges. Composites Part B: Engineering. 2018 Jun 15;143:172-96.
99. Hager I, Golonka A, Putanowicz R. 3D printing of buildings and building components as the future of sustainable construction?. Procedia Engineering. 2016 Jan 1;151:292-9.
100. Pagonis DN, Kaltsas G, Koutsis T, Pagonis A. A Novel Engine Air Intake Sensor Based on 3D Printing and PCB Technology. In2021 IEEE Sensors 2021 Oct 31 (pp. 1-4). IEEE.

101. Shahrubudin N, Lee TC, Ramlan R. An overview on 3D printing technology: Technological, materials, and applications. Procedia Manufacturing. 2019 Jan 1;35:1286-96.

102. Wang X, Jiang M, Zhou Z, Gou J, Hui D. 3D printing of polymer matrix composites: A review and prospective. Composites Part B: Engineering. 2017 Feb 1;110:442-58.

103. Shahrubudin N, Lee TC, Ramlan R. An overview on 3D printing technology: Technological, materials, and applications. Procedia Manufacturing. 2019 Jan 1;35:1286-96.

104. Cabrera MS, Sanders B, Goor OJ, Driessen-Mol A, Oomens CW, Baaijens FP. Computationally designed 3D printed self-expandable polymer stents with biodegradation capacity for minimally invasive heart valve implantation: A proof-of-concept study. 3D printing and Additive Manufacturing. 2017 Mar 1;4(1):19-29.

105. Tetsuka H, Shin SR. Materials and technical innovations in 3D printing in biomedical applications. Journal of Materials Chemistry B. 2020;8(15):2930-50.

106. Bhattacharjee N, Urrios A, Kang S, Folch A. The upcoming 3D-printing revolution in microfluidics. Lab on a Chip. 2016;16(10):1720-42.

107. Chia HN, Wu BM. Recent advances in 3D printing of biomaterials. Journal of biological engineering. 2015 Dec;9(1):1-4.

108. Chen Z, Li Z, Li J, Liu C, Lao C, Fu Y, Liu C, Li Y, Wang P, He Y. 3D printing of ceramics: A review. Journal of the European Ceramic Society. 2019 Apr 1;39(4):661-87.

109. Zhou LY, Fu J, He Y. A review of 3D printing technologies for soft polymer materials. Advanced Functional Materials. 2020 Jul;30(28):2000187.

110. Sood AK, Ohdar RK, Mahapatra SS. Parametric appraisal of mechanical property of fused deposition modelling processed parts. Mater Des 2010;31(1):287–95.

111. Yap CY, Chua CK, Dong ZL, Liu ZH, Zhang DQ, Loh LE, Sing SL. Review of selective laser melting: Materials and applications. Applied physics reviews. 2015 Dec 9;2(4):041101.

112. Bhushan B, Caspers M. An overview of additive manufacturing (3D printing) for microfabrication. Microsystem Technologies. 2017 Apr;23(4):1117-24.

113. Dutta B, Palaniswamy S, Choi J, Song LJ, Mazumder J. Direct metal deposition. Advanced Materials & Processes. 2011 May:33.

114. Frazier WE. Metal additive manufacturing: a review. Journal of Materials Engineering and performance. 2014 Jun;23(6):1917-28.

115. Edgar J, Tint S. Additive manufacturing technologies: 3D printing, rapid prototyping, and direct digital manufacturing. Johnson Matthey Technology Review. 2015 Jul 1;59(3):193-8.

116. Wang X, Jiang M, Zhou Z, Gou J, Hui D. 3D printing of polymer matrix composites: A review and prospective. Composites Part B: Engineering. 2017 Feb 1;110:442-58.

117. Perris J, Xu Y, Kartal ME, Gadegaard N, Mulvihill DM. Tailorable and Repeatable Normal Contact Stiffness via Micropatterned Interfaces. Tribology Letters. 2021 Sep;69(3):1-2.

118. Wu B, Kumar A, Pamarthy S. High aspect ratio silicon etch: A review. Journal of applied physics. 2010 Sep 1;108(5):9.

119. Tay BY, Loh NH, Tor SB, Ng FL, Fu G, Lu XH. Characterisation of micro gears produced by micro powder injection moulding. Powder Technology. 2009 Jan 10;188(3):179-82.

120. Hung PJ, Lee PJ, Sabounchi P, Aghdam N, Lin R, Lee LP. A novel high aspect ratio microfluidic design to provide a stable and uniform microenvironment for cell growth in a high throughput mammalian cell culture array. Lab on a Chip. 2005;5(1):44-8.

121. Tay BY, Loh NH, Tor SB, Ng FL, Fu G, Lu XH. Characterisation of micro gears produced by micro powder injection moulding. Powder Technology. 2009 Jan 10;188(3):179-82.

122. Yoon SH, Cha NG, Lee JS, Park JG, Carter DJ, Mead JL, Barry CM. Effect of processing parameters, antistiction coatings, and polymer type when injection molding microfeatures. Polymer Engineering & Science. 2010 Feb;50(2):411-9.

123. Maghsoudi K, Jafari R, Momen G, Farzaneh M. Micro-nanostructured polymer surfaces using injection molding: A review. Materials today communications. 2017 Dec 1;13:126-43.

124. Tofteberg TR, Andreassen E. Multiscale simulation of injection molding of parts with low aspect ratio microfeatures. International Polymer Processing. 2010 Mar 1;25(1):63-74.

125. Raffa ML, Nguyen VH, Haiat G. Micromechanical modeling of the contact stiffness of an osseointegrated bone–implant interface. BioMedical Engineering OnLine. 2019 Dec;18(1):1-8.

126. Eriten M, Lee CH, Polycarpou AA. Measurements of tangential stiffness and damping of mechanical joints: Direct versus indirect contact resonance methods. Tribology international. 2012 Jun 1;50:35-44.

127. Brake, M.R.W.: The Mechanics of Jointed Structures: Recent Research and Open Challenges for Developing Predictive Models for Structural Dynamics. Springer, Cham (2018)

128. Chang Y, Ding J, He Z, Shehzad A, Ding Y, Lu H, Zhuang H, Chen P, Zhang Y, Zhang X, Chen Y. Effect of joint interfacial contact stiffness on structural dynamics of ultra-precision machine tool. International Journal of Machine Tools and Manufacture. 2020 Nov 1;158:103609.

129. Barber JR. Incremental stiffness and electrical contact conductance in the contact of rough finite bodies. Physical Review E. 2013 Jan 25;87(1):013203.

130. Barber J. Bounds on the electrical resistance between contacting elastic rough bodies. Proceedings of the royal society of London. Series A: mathematical, physical and engineering sciences. 2003 Jan 8;459(2029):53-66.

131. Carbone, G.: Grasping in Robotics. Springer, London (2013)

132. Zou HT, Wang BL. Investigation of the contact stiffness variation of linear rolling guides due to the effects of friction and wear during operation. Tribology international. 2015 Dec 1;92:472-84.

133. Sever, I.A.: Experimental validation of turbomachinery blade vibration predictions. Ph.D. Dissertation, Imperial College London (2004)

134. Jaber SB, Hamilton A, Xu Y, Kartal ME, Gadegaard N, Mulvihill DM. Friction of flat and micropatterned interfaces with nanoscale roughness. Tribology International. 2021 Jan 1;153:106563.

135. Hamilton A, Xu Y, Kartal ME, Gadegaard N, Mulvihill DM. Enhancing strength and toughness of adhesive joints via micro-structured mechanical interlocking. International Journal of Adhesion and Adhesives. 2021 Mar 1;105:102775.

136. Sutton MA, Wolters WJ, Peters WH, Ranson WF, McNeill SR. Determination of displacements using an improved digital correlation method. Image and vision computing. 1983 Aug 1;1(3):133-9.

137. Polonsky, I.A., Keer, L.M.: A numerical method for solving rough contact problems based on the multi-level multi-summation and conjugate gradient techniques. Wear 231(2), 206–219 (1999)

138. Amin R, Knowlton S, Hart A, Yenilmez B, Ghaderinezhad F, Katebi-far S. 3D-printed microfluidic devices. Biofabrication, 8 (2): 022001.

139. Convery N, Samardzhieva I, Stormonth-Darling JM, Harrison S, Sullivan GJ, Gadegaard N. 3D Printed Tooling for Injection Molded Microfluidics. Macromolecular Materials and Engineering. 2021 Nov;306(11):2100464.

140. Kumar S, Bhushan P, Pandey M, Bhattacharya S. Additive manufacturing as an emerging technology for fabrication of microelectromechanical systems (MEMS). Journal of Micromanufacturing. 2019 Nov;2(2):175-97.

141. Wang Z, Yi Z, Qin M, Huang QA. Low-drift MEMS thermal wind sensor with symmetric packaging using plastic injection molding process. IEEE Transactions on Instrumentation and Measurement. 2021 Mar 22;70:1-8.

142. Kurella A, Dahotre NB. Surface modification for bioimplants: the role of laser surface engineering. Journal of biomaterials applications. 2005 Jul;20(1):5-0.

143. Vorobyev AY, Guo C. Femtosecond laser structuring of titanium implants. Applied surface science. 2007 Jun 30;253(17):7272-80.

144. Koch K, Schulte AJ, Fischer A, Gorb SN, Barthlott W. A fast, precise and low-cost replication technique for nano-and high-aspect-ratio structures of biological and artificial surfaces. Bioinspiration & biomimetics. 2008 Sep 8;3(4):046002.

145. Schulte AJ, Koch K, Spaeth M, Barthlott W. Biomimetic replicas: transfer of complex architectures with different optical properties from plant surfaces onto technical materials. Acta Biomaterialia. 2009 Jul 1;5(6):1848-54.

146. Wu W, Guijt RM, Silina YE, Koch M, Manz A. Plant leaves as templates for soft lithography. RSC advances. 2016;6(27):22469-75.

147. Gitlin L, Schulze P, Belder D. Rapid replication of master structures by double casting with PDMS. Lab on a Chip. 2009;9(20):3000-2.

148. Prüm B, Bohn HF, Seidel R, Rubach S, Speck T. Plant surfaces with cuticular folds and their replicas: influence of microstructuring and surface chemistry on the attachment of a leaf beetle. Acta Biomaterialia 2013;9:6360–8.

149. Willis K, Brockmeyer E, Hudson S, Poupyrev I. Printed optics: 3D printing of embedded optical elements for interactive devices. InProceedings of the 25th annual ACM symposium on User interface software and technology 2012 Oct 7 (pp. 589-598).

150. Waheed S, Cabot JM, Macdonald NP, Lewis T, Guijt RM, Paull B, Breadmore MC. 3D printed microfluidic devices: enablers and barriers. Lab on a Chip. 2016;16(11):1993-2013.

151. Mischkot M, Hansen HN, Pedersen DB. Additive manufacturing for the production of inserts for micro injection moulding. In15th International Conference of the European Society for Precision Engineering and Nanotechnology 2015.

152. Hofstätter T, Mischkot M, Pedersen DB, Tosello G, Hansen HN. Evolution of surface texture and cracks during injection molding of fiber-reinforced, additively-manufactured, injection molding inserts. InProceedings of ASPE Summer Topical Meeting 2016: Dimensional Accuracy and Surface Finish in Additive Manufacturing 2016.

153. Zhang Y, Pedersen DB, Gøtje AS, Mischkot M, Tosello G. A Soft Tooling process chain employing Additive Manufacturing for injection molding of a 3D component with micro pillars. Journal of Manufacturing Processes. 2017 Jun 1;27:138-44.

154. Zhu W, Ma X, Gou M, Mei D, Zhang K, Chen S. 3D printing of functional biomaterials for tissue engineering. Current opinion in biotechnology. 2016 Aug 1;40:103-12.

155. Do AV, Khorsand B, Geary SM, Salem AK. 3D printing of scaffolds for tissue regeneration applications. Advanced healthcare materials. 2015 Aug;4(12):1742-62.

156. Jammalamadaka U, Tappa K. Recent advances in biomaterials for 3D printing and tissue engineering. Journal of functional biomaterials. 2018 Mar;9(1):22.

157. Bennett AI, Harris KL, Schulze K, Urueña JM, McGhee AJ, Pitenis AA, Müser MH, Angelini TE, Sawyer WG. Contact measurements of randomly rough surfaces. Tribology Letters. 2017 Dec;65(4):1-8.

158. Müser MH, Dapp WB, Bugnicourt R, Sainsot P, Lesaffre N, Lubrecht TA, Persson BN, Harris K, Bennett A, Schulze K, Rohde S. Meeting the contact-mechanics challenge. Tribology Letters. 2017 Dec;65(4):1-8.

159. dAR J, Wimberger-Friedl R. Precision injection molding. Carl Hanser, Munich. 2006 Mar.

160. Koch K, Bhushan B, Barthlott W. Multifunctional surface structures of plants: an inspiration for biomimetics. Progress in Materials science. 2009 Feb 1;54(2):137-78.

161. Prüm B, Bohn HF, Seidel R, Rubach S, Speck T. Plant surfaces with cuticular folds and their replicas: influence of microstructuring and surface chemistry on the attachment of a leaf beetle. Acta Biomaterialia. 2013 May 1;9(5):6360-8.

162. Kumar C, Le Houérou V, Speck T, Bohn HF. Straightforward and precise approach to replicate complex hierarchical structures from plant surfaces onto soft matter polymer. Royal Society open science. 2018 Apr 18;5(4):172132.

163. Kumar C, Palacios A, Surapaneni VA, Bold G, Thielen M, Licht E, Higham TE, Speck T, Le Houérou V. Replicating the complexity of natural surfaces: technique validation and applications for biomimetics, ecology and evolution. Philosophical Transactions of the Royal Society A. 2019 Feb 11;377(2138):20180265.

164. Sun M, Luo C, Xu L, Ji H, Ouyang Q, Yu D. Artificial lotus leaf by nanocasting. Langmuir. 2005;21(19):8978-81.

165. Salta M, Wharton JA, Stoodley P, Dennington SP, Goodes LR, Werwinski S, Mart U, Wood RJ, Stokes KR. Designing biomimetic antifouling surfaces. Philosophical Transactions of the Royal Society A: Mathematical, Physical and Engineering Sciences. 2010 Oct 28;368(1929):4729-54.

166. Yan H, Wu Q, Yu C, Zhao T, Liu M. Recent progress of biomimetic antifouling surfaces in marine. Advanced Materials Interfaces. 2020 Oct;7(20):2000966.

167. Huang Z, Yang S, Zhang H, Zhang M, Cao W. Replication of leaf surface structures for light harvesting. Scientific reports. 2015 Sep 18;5(1):1-10.

168. McDonald B, Patel P, Zhao B. 2013 Micro-structured polymer film mimicking the trembling Aspen leaf. Chem. Eng. Process Tech. 1, 1012–1018.

169. Xu Y, Jackson RL. Statistical models of nearly complete elastic rough surface contact-comparison with numerical solutions. Tribology International. 2017 Jan 1;105:274-91.

170. Hu YZ, Tonder K. Simulation of 3-D random rough surface by 2-D digital filter and Fourier analysis. International journal of machine tools and manufacture. 1992 Feb 1;32(1-2):83-90.

171. Wu JJ. Simulation of rough surfaces with FFT. Tribology international. 2000 Jan 1;33(1):47-58.

172. Yastrebov VA, Anciaux G, Molinari JF. From infinitesimal to full contact between rough surfaces: evolution of the contact area. International Journal of Solids and Structures. 2015 Jan 1;52:83-102.

173. Song J, Vorburger T. Topography measurements and applications. InThird International Symposium on Precision Mechanical Measurements 2006 Oct 13 (Vol. 6280, pp. 417-424). SPIE.

174. Alicona Help User's Manual, IF – MeasurementSuite 5.1. Bruker Alicona, Austria, 2013

175. Kain A, Mueller C, Reinecke H. High aspect ratio-and 3D-printing of freestanding sophisticated structures. Procedia Chemistry. 2009 Sep 1;1(1):750-3.

176. Krieger KJ, Bertollo N, Dangol M, Sheridan JT, Lowery MM, O'Cearbhaill ED. Simple and customizable method for fabrication of high-aspect ratio microneedle molds using low-cost 3D printing. Microsystems & nanoengineering. 2019 Sep 9;5(1):1-4.

177. Compton BG, Lewis JA. 3D-printing of lightweight cellular composites. Advanced materials. 2014 Sep;26(34):5930-5.

178. Greer AI, Barbour E, Cutiongco MF, Stormonth-Darling JM, Convery N, Alsaigh RE, Lavery MP, Gadegaard N. Large volume nanoscale 3D printing: Nano-3DP. Applied Materials Today. 2020 Dec 1;21:100782.

179. Rabinowicz E, Tanner RI. Friction and wear of materials. Journal of Applied Mechanics. 1966;33(2):479.

180. Fuller KN, Tabor D. The effect of surface roughness on the adhesion of elastic solids. Proceedings of the Royal Society of London. A. Mathematical and Physical Sciences. 1975 Sep 30;345(1642):327-42.

181. Campana C, Persson BN, Müser MH. Transverse and normal interfacial stiffness of solids with randomly rough surfaces. Journal of physics: condensed matter. 2011 Feb 3;23(8):085001.

182. Larsson R. Modelling the effect of surface roughness on lubrication in all regimes. Tribology International. 2009 Apr 1;42(4):512-6.

183. Shvarts AG, Yastrebov VA. Trapped fluid in contact interface. Journal of the Mechanics and Physics of Solids. 2018 Oct 1;119:140-62.

184. Persson BN, Albohr O, Tartaglino U, Volokitin AI, Tosatti E. On the nature of surface roughness with application to contact mechanics, sealing, rubber friction and adhesion. Journal of physics: Condensed matter. 2004 Dec 10;17(1):R1.

185. Sneddon S, Xu Y, Dixon M, Rugg D, Li P, Mulvihill DM. Sensitivity of material failure to surface roughness: A study on titanium alloys Ti64 and Ti407. Materials & Design. 2021 Feb 15;200:109438.

186. Busse A, Jelly TO. Influence of surface anisotropy on turbulent flow over irregular roughness. Flow, Turbulence and Combustion. 2020 Mar;104(2):331-54.

187. Kumar C, Favier D, Speck T, Le Houérou V. In situ investigation of adhesion mechanisms on complex microstructured biological surfaces. Advanced Materials Interfaces. 2020 Oct;7(20):2000969.

188. Khoshkhoo A, Carrano AL, Blersch DM, Kardel K. Engineering of bio-mimetic substratum topographies for enhanced early colonization of filamentous algae. Plos one. 2019 Jul 5;14(7):e0219150.

189. Carrano AL, Blersch DM, Kardel K, Khoshkhoo A. Understanding attachment preferences of benthic algae through controlled surface topographies on 3D printed substrata. In5th International Conference on Surface Metrology (ICSM 2016) Poznan, Poland 2016 Apr 4.

190. Kardel K, Carrano AL, Blersch DM, Kaur M. Preliminary development of 3D-printed custom substrata for benthic algal biofilms. 3D Printing and Additive Manufacturing. 2015 Mar 1;2(1):12-9.

191. Elliott O, Gray S, McClay M, Nassief B, Nunnelley A, Vogt E, Ekong J, Kardel K, Khoshkhoo A, Proaño G, Blersch DM. Design and Manufacturing of High Surface Area 3D-Printed Media for Moving Bed Bioreactors for Wastewater Treatment. Journal of Contemporary Water Research & Education. 2017 Apr;160(1):144-56.

192. Sahli R, Prot A, Wang A, Müser MH, Piovarči M, Didyk P, Bennewitz R. Tactile perception of randomly rough surfaces. Scientific reports. 2020 Sep 25;10(1):1-2.

193. Shvarts AG, Xu Y, Min G, Athanasiadis I, Kaczmarczyk L, Mulvihill DM, Pearce CJ. Finite-element modelling of triboelectric nanogenerators accounting for surface roughness. InProceedings of UKACM 2021 conference 2021.

194. Xu Y, Min G, Gadegaard N, Dahiya R, Mulvihill DM. A unified contact force-dependent model for triboelectric nanogenerators accounting for surface roughness. Nano Energy. 2020 Oct 1;76:105067.

195. Min G, Xu Y, Cochran P, Gadegaard N, Mulvihill DM, Dahiya R. Origin of the contact force-dependent response of triboelectric nanogenerators. Nano Energy. 2021 May 1;83:105829.

196. Kumar C, Perris J, Bairagi S, Min G, Xu Y, Gadegaard N, Mulvihill DM. Multiscale in-situ quantification of the role of surface roughness and contact area using a novel Mica-PVS triboelectric nanogenerator. Nano Energy. 2022 Dec 21:108122.

197. Perris J, Kumar C, Xu Y, Tassieri M, Kartal ME, Gadegaard N, Mulvihill DM. 3D Printing and Rapid Replication of Advanced Numerically Generated Rough Surface Topographies in Numerous Polymers. Advanced Engineering Materials. 2022 Aug 3:2200832.

198. Sun Q, Liu X, Mu X, Gao Y. Estimation for normal contact stiffness of joint surfaces by considering the variation of critical deformation. Assembly Automation. 2020 Jan 17.

199. Chang Y, Ding J, He Z, Shehzad A, Ding Y, Lu H, Zhuang H, Chen P, Zhang Y, Zhang X, Chen Y. Effect of joint interfacial contact stiffness on structural dynamics of ultra-precision machine tool. International Journal of Machine Tools and Manufacture. 2020 Nov 1;158:103609.

200. Benardos PG, Vosniakos GC. Predicting surface roughness in machining: a review. International journal of machine tools and manufacture. 2003 Jun 1;43(8):833-44.

201. Turner BN, Gold SA. A review of melt extrusion additive manufacturing processes: II. Materials, dimensional accuracy, and surface roughness. Rapid Prototyping Journal. 2015 Apr 20.

202. Sharp JS, Poole SF, Kleiman BW. Optical measurement of contact forces using frustrated total internal reflection. Physical Review Applied. 2018 Sep 24;10(3):034051.

203. Contreras-Naranjo JC, Silas JA, Ugaz VM. Reflection interference contrast microscopy of arbitrary convex surfaces. Applied optics. 2010 Jul 1;49(19):3701-12.

204. Limozin L, Sengupta K. Quantitative reflection interference contrast microscopy (RICM) in soft matter and cell adhesion. ChemPhysChem. 2009 Nov 9;10(16):2752-68.

205. Zhai C, Gan Y, Hanaor D, Proust G, Retraint D. The role of surface structure in normal contact stiffness. Experimental Mechanics. 2016 Mar;56(3):359-68.